INFLUENCE OF SOFT ENCAPSULATION ON THE WIRELESS POWER TRANSFER FOR BIOELECTRONIC MEDICINE

EVALUATING THE EFFICIENCY OF NEAR-FIELD RESONANT INDUCTIVE LINKS

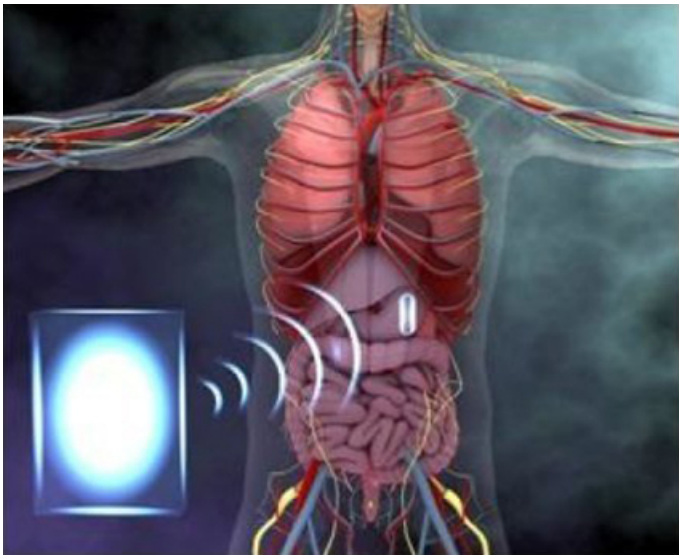

by

Anastasios MALISSOVAS

Faculty of Mechanical, Maritime & Materials Engineering,
Delft University of Technology, Delft, the Netherlands

TU Delft Delft University of Technology

Salvia BioElectronics

INFLUENCE OF SOFT ENCAPSULATION ON THE WIRELESS POWER TRANSFER FOR BIOELECTRONIC MEDICINE

EVALUATING THE EFFICIENCY OF NEAR-FIELD RESONANT INDUCTIVE LINKS

Thesis

in partial fulfillment of the requirements for the degree of

Master of Science
in Biomedical Engineering,
Bioelectronics specialization

at the Delft University of Technology,
to be defended publicly on Wednesday July 3, 2019 at 11:00 AM.

by

Anastasios MALISSOVAS

Faculty of Mechanical, Maritime & Materials Engineering,
Delft University of Technology, Delft, the Netherlands

Student number:	4624459	
Project duration:	May 1, 2018 – July 3, 2019	
Thesis committee:	Prof. Dr. Ir. W. Serdijn,	TU Delft
	Dr. V. Giagka,	TU Delft, supervisor
	Prof. Dr. PJ French	TU Delft

An electronic version of this thesis is available at http://repository.tudelft.nl/.

Science is a wonderful thing
if one does not have to earn one's living at it.

Albert Einstein

SUMMARY

As the era of Bioelectronic medicines (BEms) evolves, new technological challenges are generated, including miniaturized devices that are encapsulated with flexible materials and energized by wireless power transmission (WPT) techniques. Among them, magnetostatic, also known as inductive is the most viable candidate for shallow applications of peripheral nerve stimulation (PNS). However, the conductive nature of the human tissue with high relative permittivity increases the parasitic components of the induction coils and leads to power losses in the WPT link.

This study focuses on the influence of biocompatible, soft, polymeric materials, such as polydimethyloxane (PDMS) and Parylene-C, on the electrical behavior of the aforementioned externally powered receivers. Unlike previous works, this investigation employs a series of case studies which include various implantation environments, thin and different encapsulation materials taking also into account the non-hermetic nature of polymers. Analytical and simulation models are utilized to discriminate the effect of various packaging schemes and to relate their influence on the inductive link design and efficiency. Lastly, empirical measurements in air and phosphate buffered saline (PBS) aim to verify the proposed methods.

The modeling and experimental results demonstrate that the soft encapsulation thickness on top of the coil traces has a strong influence on the power transfer efficiency (PTE) and its estimation. In addition, it is found that its behavior is strongly coupled with the dielectric properties of the surrounding tissue, suggesting that they should be included during the link design constraints along with the total volume of the implantable device. Based on the above and the BEm requirement of miniaturization, this work provides evidence that thin devices with efficient links can be realized in superficial soft tissue, decoupling the polymeric material selection from the application-specific design considerations. On the contrary, it is found that implantation in deep tissue requires thick encapsulation materials with a low dielectric loss tangent, promoting the compatibility of ultrasonic (US) transducers with the BEm packaging in this environment.

ACKNOWLEDGEMENTS

I am using this opportunity to express my special thanks of gratitude to Vasiliki Giagka for the supervision and inspiration to be involved in the technological aspects of bioelectronic medicine. In addition, I would like to thanks Salvia Bioelectronics B.V. for the trust and the opportunity to work within an innovative company of great engineers and wonderful people. I am profoundly grateful to the director of product development, Zameed SahebAli who steered me in the right direction throughout this project.

I would also like to say thanks to Wouter Serdijn, Virgilio Valente, Marco Spirito, Michiel Pertijs and Rob Remis for the meetings we had, answering my numerous questions. Also, I would like to acknowledge the contribution of Atef Akhnoukh, Kambiz Nanbakhsh, Nasim Bakhshaee, Gandhika Wardhana, Andrada Velea and Stefan Eijsvogel. Also, I consider myself as a very lucky individual as I was provided with an opportunity to be a part of the Bioelectronics group. Thank you for the meaningful conversations, brainstorming sessions, the knowledge I gained from the monthly group meetings and of course, the great times we had together. Working in this pleasant working environment was always motivating me to to find novel solutions in this project.

Finally, I would like to my family and friends for the unparalleled support and continuous encouragement throughout my years of study. This accomplishment would not have been possible without them. Thank you.

Anastasios "Tasos" Malissovas
Delft, June 2019

CONTENTS

List of Figures

LIST OF TABLES

NOMENCLATURE

Abbreviations

Symbol	Description
2-D	two-dimensional
AC	Alternating Current
AIMDs	Active implantable devices
ALD	Atomic Layer Deposition
AlN	Aluminum Nitride
Au	Gold
BaTiO3	Barium Titanate
BEm	Bioelectronic medicine
CI	Cochlear Implants
CMUT	Capacitive Micromachined Ultrasonic Transducers
CTQ	Critical to quality
CTQ	Qritical for quality
DALY	Disability-Adjusted Life Years
DBS	Deep Brain Stimulators
ECC	Electronic Communications Committee
EM	Electromagnetic
EMF	Electromotive force
FCC	Federal Communications Commission
FDA	Food and Drug Administratio
FEM	Finite Element Methods
IF	Intermidiate frequency
IMDs	Implantable Medical Devices

ISM	Industrial, Scientific and Medical
LCP	Liquid-Crystal Polymer
LiNbO3	Lithium Niobate
LTCC	Low Temperature Co-fired Ceramics
MDR	Medical Device Regulation
MEE	Maximum Energy Efficiency
MIT	Massachusetts Institute of Technology
MPT	Maximum Power Transfer
NRIC	near field resonance inductive coupling
PDMS	Polydimethylsiloxane
Pi	Polyimide
PME	Power Matching Conversion
PMS	Post Market Surveillance
PMUT	Piezoelectric Micromachined Ultrasonic Transducers
PNS	Peripheral Nervous System
PSCs	Printed Spiral Coils
PTE	Power Transfer Efficiency
PZT	Lead Zirconate Titanate
QMS	Quality Management System
RF	radio frequency
RX	Receiver
SCS	Spinal Cord Stimulators
Si	Silicon
SP	Series to Parallel
SRF	Self Resonance Frequency
TX	Transmitter
US	Ultrasound
WPT	Wireless Power Transfe
ZnO	Zinc Oxide

1

INTRODUCTION

The aim of this introductory chapter is to present the motivation behind the initiation of this study. Based on the recent technological advances and challenges for the realization of bioelectronic medicines (BEms), the research objectives are defined and an overview of this work is presented.

1.1. BIOELECTRONIC MEDICINE

Over the last decades, the scientific interest around the merge of electronics and biology, a field of research that is known as bioelectronics, has grown immensely. The tremendous clinical demands to expand the number of patients that benefit from neuromodulation and the recent technological advances introduced a new term of therapeutic agents, namely bioelectronic medicines (BEms). These devices are envisioned to become a mainstay of medical treatment with less side effects from their pharmaceutical counterparts that have a systemic influence on the human body [139].

Based on the recent insights on neuromodulation that focus on the peripheral nervous system (PNS) [112], it is evident that BEms could intervene with it in several therapeutic contexts (see Figure 1.1) in order to control biological processes or neuroprosthesis [132]. Depending on the implantation site, they can cure chronic pain syndromes [146], metabolic diseases [157], digestive disorders [19] and inflammatory responses [35] such as chronic migraine, diabetes, gastroparesis and rheumatoid arthritis respectively.

Besides the therapeutic benefits for the patients, the BEm is reported [155] to have a significant economic and social impact, as the prevalence of chronic diseases is continuously rising [50]. According to the worldwide statistical surveying report of 2018 [199], the current market of AIMDs was esteemed at $18.59 billion, whilst that of BEm $29.66 billion by 2023. In addition, pondering on the importance of patients' safety, disability-adjusted life year (DALY) and quality of life, the regulatory framework has been recently changed. The new European Medical Device Regulation (MDR) in 2017 (Reg. 2017/745) introduced new requirements for clinical evidence, upgrades to quality management systems (QMS) and post market surveillance (PMS), rendering the compliance with the relevant legislation more strict [41].

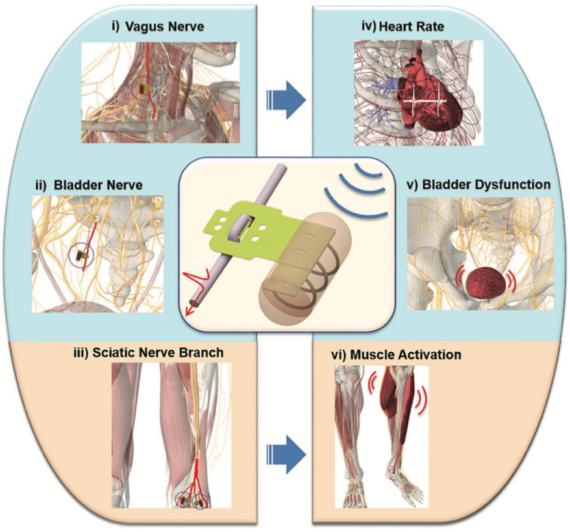

Figure 1.1: Depending on the anatomical site BEms, can interface with i) the vagus, ii) bladder and iii) sciatic nerve for iv) heart rate modulation, v) bladder control and vi) muscle pain alleviation. Image taken from [112].

Up to this point, one may argue why the BEms have not been realized so far. In order to answer this question, one has to analyze the technology of the existing AIMDs (e.g. spinal cord stimulators). Their main limitation relies on the utilization of bulky batteries that even in the state of the art devices [86] capture almost half of the device space, whereas their replacement requires the device explantation via invasive surgical procedures. In addition, their hermetic packaging materials (e.g. metals) employed to protect their electronics from the harsh physiological environment results into stiff devices that restrict the implantation site and compromise their non-obtrusive operation.

As a result, the BEm technology roadmaps have already been addressed [17] and collaboration between governments, industry, and academia will foster the development of the next generation of implants, transitioning the multidisciplinary research into commercial products. These include among other low-cost miniaturized devices with a total volume less than $1cm^3$ [66] that could be implanted via minimally invasive procedures and conform with the mechanical properties of the human tissue. The aforementioned requirements pose the cross-cutting challenges of merging soft, flexible and biocompatible encapsulation materials and wireless powering solutions [112] in the next generation of AIMDs. In this study, we will focus on these technological challenges, an overview of which is presented in the following introductory chapters.

1.2. POWERING IMPLANTS

The next generation of AIMDs requires alternative and sufficient power solutions that will replace the existing bulky batteries. This critical task raised the scientific interest of many researchers in this field since 1958 when the first battery operated pacemaker was developed [9]. It was including a nickel-cadmium battery that could last one week

of operation and a receiving coil for recharging it. Nevertheless, there are many different powering methods proposed since then, focusing on either electromagnetic (EM), acoustic and energy harvesting solutions.

Starting from the latter, the ability to scavenge energy from the human body seems an ideal solution for autonomous AIMDs. There are different approaches regarding the nature of the harvested energy that can be converted into electrical power. Reports include thermoelectric devices [150, 189] which leverage the body temperature gradients, piezoelectric [40, 96] and triboelectric devices [13, 52] that convert kinetic energy from the surrounding tissue and fuel cells [56, 94] that transduce chemical reactions. Nonetheless, these methods have the major drawback of limited power generation that lies in the μ-Watt range [159] and the need of relatively large harvesting areas [70], promoting the external power delivery as a more feasible solution.

One of the most studied wireless power transfer (WPT) method is that of EM power transfer. In the early years of 20th century, the pioneer Nikola Tesla [182] demonstrated its feasibility when he provided power to a 40 W lamp over 60 cm distance with two magnetically coupled coils. Since then, the research around WPT is escalated, introducing alternative transmission methods that can be classified into radiative (or far-field [51, 116]) and non-radiative (or near-field) EM coupling. The latter can be further distinguished into the near-field inductive [3, 87], resonant inductive [78, 100] and capacitive [88, 174] coupling. All of these techniques have their own merits and their selection depends on the effective transmission distance, the frequency of operation and the application power demands [110].

The most promising techniques from the aforementioned though is that of near field resonant inductive coupling (NRIC), which has been already approved by the Food and Drug Administration (FDA) for powering cochlear [79] and retinal implants [39]. Figure 1.2a depicts its principle of operation. Based on the Michael's Faraday discovery of EM induction [53] an electromotive force (EMF) is induced on the receiving coil when it is placed in the primary's near field reactive region. A breakthrough that improves the power transfer efficiency (PTE) over a larger distance from the non-resonant approach was made from a research group of Massachusetts Institute of Technology (MIT) [110] utilizing two high coils with high quality factors (Q-factors), that were tuned at the same resonant frequency.

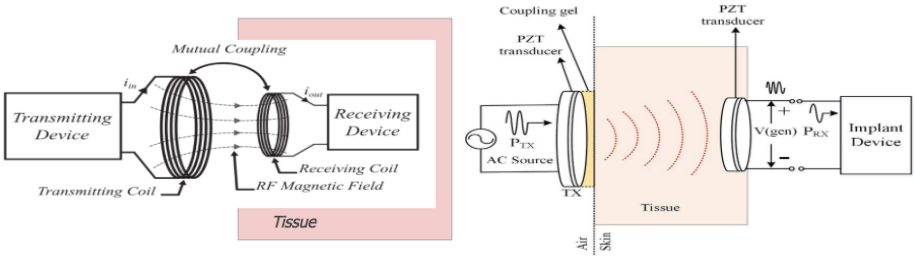

(a) (b)

Figure 1.2: WPT concepts of a) inductive and b) ultrasonic links. Images edited from [163] and [1] respectively.

1

On the other hand, power delivery by means of acoustic waves is an alternative powering solution with notable advantages. The ultrasonic power transfer employs two ultrasonic transducers as illustrated in Figure 1.2b, where the external is attached to the skin producing time-varying pressure waves that travel through the underlying tissue. As a result, the impinged waves excite the receiver and its mechanical energy can be converted in the electrical domain by the piezoelectric effect.

The great advantage of this technique is the low acoustic velocity inside the human tissue and thus, the wavelength of the acoustic waves even at low frequencies (e.g 1.5mm @1MHz) is comparable with the mm-sized acoustic transducers, rendering the energy conversion more efficient [138]. In addition, the tissue attenuation of US waves is almost negligible (i.e. $\sim 1 dBMHz^{-1}cm^{-1}$ [89]) and thus, the maximum FDA-allowed time-averaged intensity (i.e 7.2mW/mm) is even two orders of magnitude higher than the safety exposure limits of EM WPT, which vary between 10-100mW depending on the operating frequency and the implantation site.

In an attempt to verify the above, Denisov et. al. [42] made a comparative investigation between optimized at reasonable frequencies US (1 MHz) and NRIC (13.56 MHz) links. Their primary endpoint was to compare their efficiency in terms of transmission distance and receiver size. Figure 1.3a illustrates the former comparison, where the NRIC outperforms US only at short distance. In addition, it is evident from Figure 1.3b that as the receiver size shrinks, US links achieve a higher efficiency over the NRIC link, indicating that US is a favorable candidate for deep implantation and miniaturized receivers, whilst NRIC can be employed for shallow applications (i.e. <1cm [70]) with great results.

The question that still remains unanswered though in literature is their comparison in terms of their performance compatibility with the polymeric packaging materials. In this work, we will delve into this argument, investigating the impact of soft encapsulation materials and their thickness on the efficiency of NRIC links, yet the following literature review will provide all the relevant information to expand this study for US links.

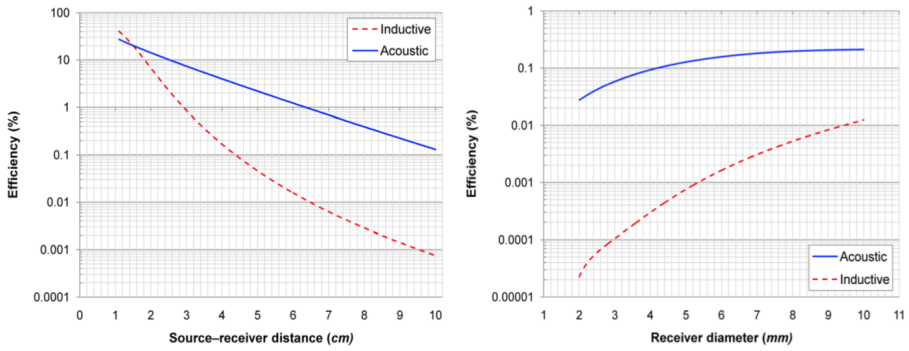

(a) (b)

Figure 1.3: Efficiency comparison between ultrasonic and inductive links as regards with their a) transmission distance and b) receiver size. Figures taken from [42].

1.3. PACKAGING APPROACHES

Conventional AIMDs typically employ laser-welded enclosures to provide a mechanically and chemically stable barrier over decades inside the hostile environment of the human body. Hermetic packages (see Figure 1.4a) made of metals such as titanium (Ti), platinum (Pt), tantalum (Ta) and their alloys [149] are currently vastly used to place the AIMDs' electronic components, accommodating the strict regulations of various clinical applications. However, metal packages have certain limitations for the realization of miniaturized BEms as they are bulky, rigid and high cost since their processing is complex for mass fabrication.

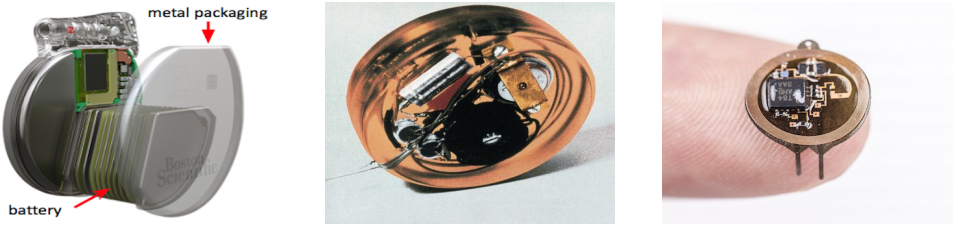

(a) (b) (c)

Figure 1.4: a) state of the art cardiac pacemaker employing hermetic metal packaging and bio-grade glass feedthroughs (Boston Scientific INOGEN EL ICD, 2015) , b) first implanted pacemaker with a silicone rubber cap [184] and c) BEm concpet employing a coil for inductive coupling [126].

Properties	Metals	Bioceramics	Polymers
Biocompatibility	Good	Good	Good
Young Modulus	High	High	Low
Hermeticity	Good	Moderate	Poor
RF transparency	Poor	Good	Good
Weight	Poor	Moderate	Good
Ease of fabrication	Difficult	Difficult	Easy
Cost	High	High	Low

Table 1.1: Packaging materials comparison. Table taken from [149].

One other category of hermetic packaging materials is that of biograde glasses (e.g Borosilicate) and bioceramics (e.g aluminum oxide, zirconia) that according to [90] were employed in order to bypass the radio-frequency (RF) opaqueness of metal packaging, allowing the communication with circuitry outside from the human body. Nonetheless, all of the aforementioned materials lack of structural biocompatibility [72], that is reported [7] to promote chronic inflammation from the mechanical mismatch between the device and tissue. As a result, the implantation site is so far restricted to specific areas (e.g. pectoral region) and most usually, extension wires and leads are utilized to reach the target nerves. The aforementioned results in invasive implantation procedures whereas the external components' fatigue increases the critical hazards for the patient safety [200].

1

Most recently, flexible and soft encapsulation schemes have been utilized to realize the concept of BEm. In general, the definition of soft materials refers to materials with a Young Modulus lower than 10^4MPa [161]. Polymers such as poly(p-xylylene) and its derivatives (e.g Parylene-C), polydimethylsiloxane (PDMS), polyimide (PI) and liquid crystal polymer (LCP) belong into this category and constitute some of the encapsulation candidates due to their favorable properties. Hassler et. al. [72] have summarized some of them, as shown in Table 1.1, underlying their low Young modulus that allows them to conform with the human tissue, high resistivity that insulates the device from the conductive nature of the surrounding environment, low density that results in lightweight devices and their wafer level processing that reduces significantly the manufacturing costs.

Concerning their favorable properties addressed above, one may wonder what is the main drawback of these materials and why they are not utilized so far in AIMDs. In order to investigate the aforementioned one has to look on the firstly cardiac pacemaker of Figure 1.4b that was developed by Zoll et. al. [184] during 1958. This device utilized a silicone rubber cap to encapsulate its electronics due to its ease of fabrication and low processing temperature. Silicone rubber along with epoxy resins were the conventional packaging until 1970. However, Maisel et. al. [121] report that the majority of 40,000 implanted pacemakers recalls were related with moisture ingress that resulted in the corrosion of the underlying electronic components.

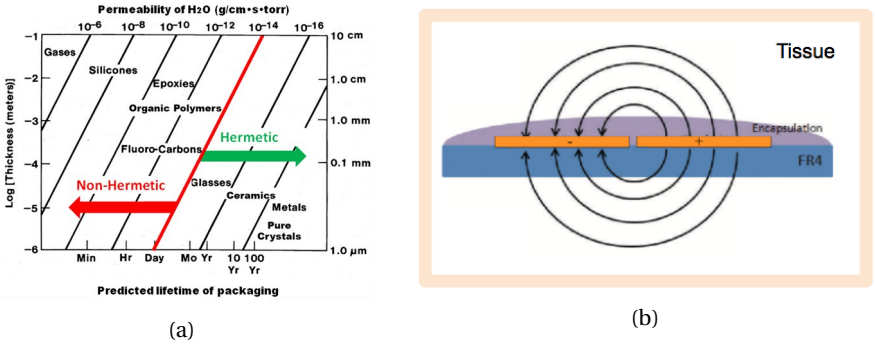

(a) (b)

Figure 1.5: a) Water vapor permeability chart for various classes of packaging materials [129]. b) Distribution of E-field within the substrate,soft encapsulation and the human tissue [38].

According to Stieglitz et. al. [176], polymers are non-hermetic by nature with their permeability being several order of magnitudes higher than other hermetic packaging materials, as shown in Figure 1.6a. As a result, the inevitable moisture ingress inside the soft encapsulation will change its mechanical [119] and dielectric properties [93]. Visweswaran et. al. [186] state that moisture will cause the polymer swelling and thereby its mechanical stress at the interface with the adhered substrate will increase over time. In addition, the introduced water vapor inside the polymer will alter its complex dielectric constant, compromising the performance of the passive electronics that are housed in it, as showed by [38].

One other basic limitation that the non-hermetic packaging introduces is illustrated

in Figure 1.6b, where the electric fields of the induction coils are distributed inside the surrounding materials and tissue. As a result, its highly conductive nature will electrically load them [188] compromising their inductive link efficiency [91]. As a result, an additional question that is introduced is how the soft encapsulation effectively insulates the device from the surroundings and how different materials and thicknesses influence the link efficiency. Concluding, although there are favorable advantages of using the polymers as encapsulation materials, their utilization in devices powered from wireless links consists a critical to quality (CTQ) parameter and thus, its consideration during the design of the WPT links requires further investigation.

1.4. RESEARCH OBJECTIVES

The aim of this work is to provide further insights regarding the impact of the soft encapsulation on the WPT links for bioelectronic medicine, focusing on NRIC links. However, since this effect is influenced by various factors the following research questions will be answered throughout this study, starting from its primary endpoint:

- What is the impact of the soft encapsulation on the near field resonant inductive link efficiency?
- What is the influence of the soft encapsulation on the electrical properties of the induction coils?
- What is the influence of the soft encapsulation materials and thickness at different implantation environments?
- Concerning the non-hermetic nature of polymers, what is the impact of moisture absorption on the electrical properties of the induction coils?

1.5. THESIS OUTLINE

This study is structured as follows:

- Chapter 2: In this chapter, the design procedure for efficient NRIC links will be given and the existing power losses in them will be presented, focusing on those related with the soft encapsulation.
- Chapter 3: The same topics discussed in the previous chapter will be given for ultrasonic links, enabling the qualitative comparison between the two of the most promising WPT links. However, the ultrasonic links are out of this study scope, yet this chapter sets the basis for further analysis.
- Chapter 4: This chapter analyzes the analytical and simulation models that were employed to study the influence of the soft encapsulation on their inductive links, including the in-vitro measurement setup for their validation.
- Chapter 5: This chapter shows detailed results of the soft encapsulation influence on the inductive link efficiency.

- Chapter 6: The novelty and conclusions of this work are given and accordingly, recommendations for further research are proposed.

2

NEAR-FIELD RESONANT INDUCTIVE COUPLING

This introductory chapter will firstly address the inductive link design procedure along with the key parameters for its optimization. Then an overview of different coil types, their geometry design, and modeling will be presented. Finally, the power losses that exist in such links will be given, focusing on those that are related to the soft encapsulation materials, thickness, and their moisture absorption.

2.1. LINK DESIGN

The design of efficient NRIC links is an iterative procedure, as shown in Figure 2.1, which starts from the application-specific design constraints. These include the frequency of operation, the maximum allowed dimensions of the receiving coil which is dictated by the implantation site, the receiver load that defines the power transferred to the implant and the working range of the link that is based on the PTE estimation and its tolerances.

Based on the above constraints, the geometry (e.g. conductor pitch) of the two magnetically coupled coils follows in order to extract their electrical parameters (e.g. quality factor) and estimate the link targets. So far, the majority of the studies in this field introduced state of the art power management electronics [99] and adaptive techniques [18] to improve and maintain the PTE on the desired levels, yet the operation of the implantable device is considered in free-space.

As discussed in the introduction though, the electrical performance of the induction coils is altered from the dielectric properties of the human tissue and consequently, this electrical loading will impact both the coil(s) geometry design and the link targets. It is therefore understood that additional considerations regarding the technology aspects are introduced. In this study we will delve into this effect, focusing on the the soft encapsulation impact on the NRIC link design and its PTE as the key metric of this evaluation.

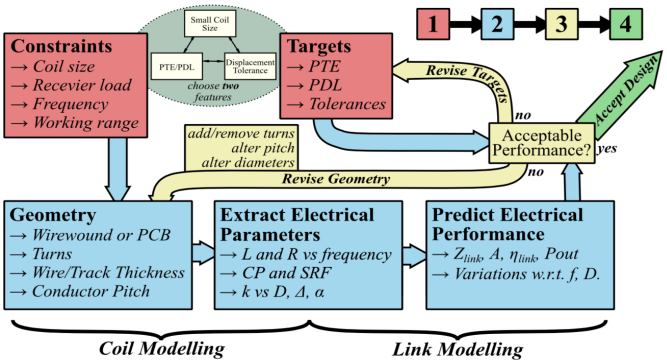

Figure 2.1: NRIC link design process which starts from the application-specific constraints and maximizes the PTE based on the geometry design of the induction coils and their electrical parameters. Image taken from [163].

2.1.1. KEY FACTORS FOR HIGH PERFORMANCE LINKS

The key factors for the performance of an NRIC link are the coupling coefficient $k_{1,2}$ between the coupled coils and their Q-factor [198]. A summary of those is given below:

- **Coupling coefficient $k_{1,2}$:** The coupling coefficient represents the portion of the magnetic flux that is coupled between the two coils and is a function of their mutual (M) and self inductances (L_1, L_2), as given in equation 2.1.1.1. The former depends on the coils displacement resilience which includes lateral and angular misalignments, whereas the self-inductance on the coil geometry. Notably, it is found [12] that the coupling coefficient decreases with the inverse cube of the coils separation distance, reasoning the poor performance of inductive links at distances larger than 1cm.

$$k_{1,2} = \frac{M}{\sqrt{L_1 L_2}} \tag{2.1.1.1}$$

- **Quality factor:** The Q-factor is defined as the ratio of the total energy stored (i.e. reactance) to the energy dissipated (i.e. resistance) per cycle of oscillation, as shown in equation 2.1.1.2. In NRIC, the utilization of high-Q coils is imperative since at (parallel) resonance, the induced voltage in the receiver is maximized (see Figure 2.2a). In addition, Schormans et. al. [163] demonstrated that the maximum theoretical efficiency of an inductive link could be high even if the $k_{1,2}$ is low, when the product of the transmitting and receiving coils q-factor is high (see Figure 2.2b). As a result, the geometry design that results in high-Q coils is one of the primary concerns in NRIC links.

$$Q = 2\pi \frac{\text{energy stored}}{\text{energy dissipated}} = \frac{\text{Im(Z)}}{\text{Re(Z)}} \tag{2.1.1.2}$$

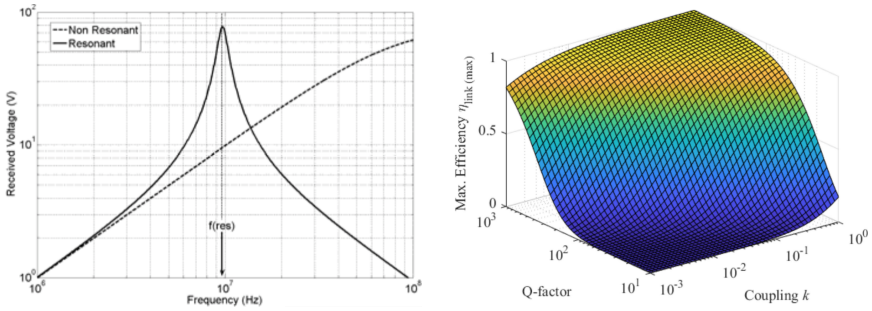

(a) (b)

Figure 2.2: a) Comparison of induced voltage between resonant and non resonant coils and b) Dependency of Q-factor and coupling coefficient on the maximum theoretical inductive link efficiency [163].

2.2. INDUCTION COILS

The first attempts in inductive links utilized multi-stranded insulated wires [152], namely litz wires since their twisting patterns equalize the current distribution in each strand, reducing the skin effect [144]. However, at frequencies higher than 1-2MHz the proximity effect increases significantly their effective resistance [179] compromising their Q-factor and the efficiency of their links.

Other approaches include the utilization of solid wires in various shapes with that of solenoid and flat spiral being the most frequently used. According to Buch et. al. [21], in applications where the total volume of the implant is restricted, such as injectable devices [196], solenoid coils are a better selection. The rational behind this conclusion is their three dimensional design that enhances their Q-factor in comparison with the spiral coils. For example, Ahn et. al. [4] utilized a solenoid coil in order to realize an $1-cm^3$ implantable device that could fit in the grey matter of the human brain.

However, litz wires require special wound machinery that makes their batch fabrication costly and even imprecise for every coil winding [91], whereas the solenoid coils integration on flexible substrates impose additional limitations. Therefore, planar coils that could be lithographically defined with high detail were introduced in the last decade, known as printed spiral coils (PSCs). PSCs can be found in various shapes such as polygonal, rectangular, square or circular. Among those, the last two are often found in literature due to their larger coupling area [46] and displacement resilience [57] respectively.

Harrison et. al. [71] studied the use of PSCs in NRIC with realistic secondary coil dimensions (i.e d_{out}=1cm) and concluded that these coils are viable candidates for WPT links, allowing the realization of flexible implantable devices that could conform with the surrounding tissue. As a result, in this work the effect of the soft encapsulation will be studied on PSCs.

2.2.1. GEOMETRY CONSIDERATIONS

The geometry design of the primary and secondary coils is based on the maximization of their coupling coefficient and Q-factors utilizing iterative algorithms that are based

on either analytical [82, 91] or finite element models (FEM) [55, 103]. In this study, a PSC design was adopted from Salvia Bioelectronics B.V., as depicted in Table 2.1, yet the rational of its geometry was classified. Accordingly, other PSC geometries are listed from literature, all of which are optimized for operation at 13.56MHz. This comparison enables the reader to quantify similarities in the geometrical parameters for the coils utilized in NRIC links.

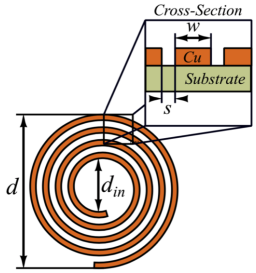

Figure 2.3: PSC cross-section.

Parameter	Symbol	Value			
Author		This study	[92]		[131]
Shape		circular	circular	rectangular	circular
Outer diameter (mm)	d_{out}	30	10	10	11.6
Inner diameter (mm)	d_{in}	24	7.2	5.5	0.5
Fill factor	ϕ	0.11	0.16	0.29	0.39
Number of turns	N	5	4	5	8
Trace width (μ m)	w	480	150	250	300
Spacing (μ m)	s	150	150	150	100
Trace thickness (μ m)	t_{psc}	70	30	30	38

Table 2.1: PSC parameters of this and other relevant studies in literature.

To start with, the first electrical parameter that is maximized through the aforementioned procedure is the inductance of the coils that enhances the Q-factor. For the case of a PSC, this could be implemented by increasing its number of turns (N) and minimizing the separation distance s between them (see Figure 2.4a). However, the aforementioned, introduce two design trade-offs.

The first includes the coil fill factor, which describes the concentration of its turns on the perimeter (i.e. $\phi = 0$) or the center of the PSC (i.e $\phi = 1$). In inductive links, ϕ is usually selected to be close to zero, as the inner turns do not contribute at the magnetic flux, whereas introduce additional ohmic losses [54]. The second trade-off includes the self resonance frequency (SRF) of the coil, above which it behaves as a capacitor and thus, the whole link performance is vanished. As a rule of the thumb, the SRF should be at least 10 times higher from the operation frequency [61] as a way to ensure that any additional electrical loading can not harness its performance. Figure 2.4b depicts the aforementioned trade-off where the increasing number of turns reduces the SRF significantly, yet maximizes the Q-factor.

Lastly, the coil conductor losses should be kept low. One way to mitigate this effect is to decrease the operating frequency, as the losses relating to the skin depth will be reduced in proportion with the $\sqrt{\omega}$ [194]. However, this is not usually feasible, since another design trade-off is introduced between the frequency of operation ω_0 that is preallocated within the frequency bands for medical applications (e.g. 13.56MHz ISM band) and the magnetic field strength [1]. For this reason, the geometry of the conductor trace is manipulated and more specifically, its width and thickness is increased in a way to reduce the losses from their finite resistivity. As it is clearly shown in the given table, the majority of the coils employ a conductor width that is much larger than their thickness in a way to increase their quality factors.

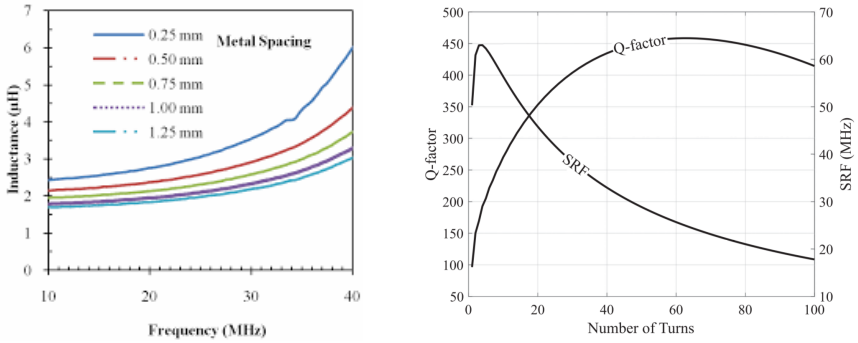

(a) (b)

Figure 2.4: a) Dependency of metal spacing on the self inductance [84] and b) Geometry design trade-off for a solenoid coil. The increasing number of its turns results in a higher Q-factor and lower SRF.[163].

2.2.2. INDUCTION COIL MODELING

The next step of the link design process is to extract the electrical parameters from the induction coil geometry. The frequency response of the coil input impedance Z_{in} can be described using its series equivalent circuit model of Figure 2.5a.

Its imaginary part (ImZ) relates the energy storage within the near-field of the coil and is a function of the reactive elements self inductance L and parasitic capacitance C_p. On the other hand, the real part (ReZ) is related with the energy dissipation and consists of the series resistance R_s from the finite conductivity of the coil traces and the dielectric loss R_p, which refers to the power dissipated into the surrounding materials and/or environment, modeled in parallel with R_s. In order to model the total losses of the inductor, the parallel equivalent model of Figure 2.5b is often employed [2] and in addition it is also used for the efficiency calculation [91] in the receiver, where the parallel loss resistance R_{loss} is calculated from the series resistance and the quality factor as follows:

$$R_{\text{loss}} = R_s(1+Q)^2 \tag{2.2.2.1}$$

In general, inductors exhibit a non-ideal frequency response due to their self resonance and non-linear current characteristics [122]. As a result, various authors in literature have been involved in order to provide analytical formulas that describe the electrical behavior of the individual elements depending on their shape, geometry and frequency of operation.

Starting from the self inductance, Wheeler et. al. [191] introduced a simple analytical model in 1928 for the calculation of a radio coil inductance. Based on this model, Mohan et. al. [128] give an analytical equation for a PSC on PCB, which can be modified to study various coil shapes (e.g. spiral, square) noting that its accuracy is close to 8% in comparison with real-world measurements.

Regarding the series resistance R_s, analytical expressions that describe the skin and proximity effects on various conductor shapes are given by Kuhn et. al. [109]. However,

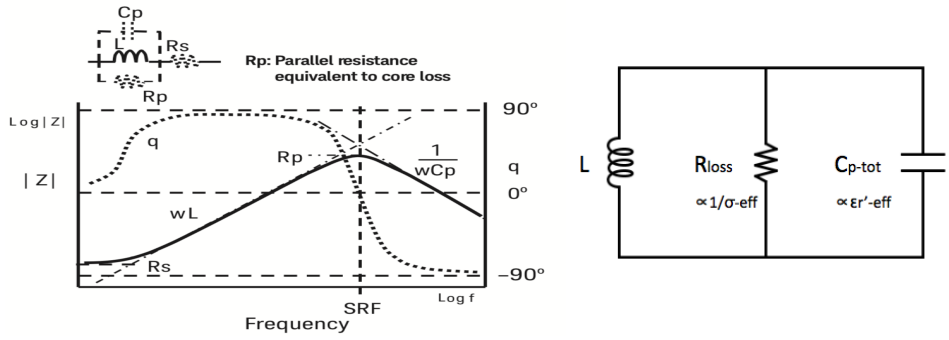

(a) (b)

Figure 2.5: a) Impedance magnitude |Z| and phase q of an inductor over frequency. At low frequencies, its impedance is purely inductive with a phase angle (q) of 90°. As the frequency increases though, the distributed capacitance starts to contribute up to the resonance point (i.e SRF), where the impedance is purely resistive and therefore maximized. From thereafter, the impedance decreases with a voltage phase shift of −90°, behaving as a capacitor and thus, it cannot be employed for inductive coupling. Image taken from [181]. b) parallel equivalent circuit

these equations were employed for spiral coils in integrated circuits (ICs), where the skin depth is larger than the conductor thickness, introducing errors in the calculation of R_s at lower frequencies. Schormans et. al. [163] delved into this effect and provided empirical factors to improve the accuracy of the aforementioned study for PSCs on FR4 substrates.

Moreover, the parasitic capacitance C_p appears in parallel with the inductor, as its coil windings are in close proximity with their neighbors and arranged in parallel. Empirical formulas that include the effect of substrate are given by Jow et. al. [91] with good accuracy. However, when the model includes a multilayer of substrate and/or superstrate materials (e.g. soft encapsulation), the technique of conformal mapping is often utilized. This method models the contribution of each dielectric layer as opposed to one (i.e coil metal traces) [68].

The first effort to model C_p with a lumped equivalent component was made by Pettenpaul et. al. [143] who provided analytical formulas based on conformal mapping for miniaturized spiral inductors on ICs, operating in the GHz frequencies. Gevorgian et. al. [63] exploited this technique for its use in multilayer substrates and superstrates providing analytical expressions for both the parasitic capacitance and parallel loss resistance. In order to investigate the validity of these models, Ghione et. al. [64] address their assumptions which include the use of perfect squared conductors with rounded corners and substrate (or superstrate) layers whose dielectric properties decrease or increase monotonically from the conductor traces. One other basic limitation for the calculation of the R_p is the skin depth, which has to be similar or larger than the thickness of the conductor at the modeled operating frequency [62].

As a result, studies [97, 131] that model the parasitic elements from the effect of the surrounding tissue utilize conformal mapping to find the effect of C_p since that of R_p is not valid for the majority of PSC geometries (see Table 2.1). Also, the novel study of Jow

and Ghovanloo et. al. [92] who verified their analytical expressions (based on conformal mapping) with measurements and simulations, explicitly state that the wide coil traces deviate from the validity range of the employed model. A formula which can model the finite resistivity of the coil's superstrate is given by Olivo et. al. [136], yet lacks the ability to capture the effect of multiple layers (e.g. soft encapsulation and tissue).

It is therefore understood that the validity of these models is not easily adapting on the coils geometry for WPT. Thus, the majority of authors in this field [92, 95, 97, 131, 195] suggest the use of numerical methods using finite element modeling (FEM) and more specifically the high frequency structure simulator (HFSS). This three dimensional (3D) full-wave simulator is usually preferred since it employs the flexibility of FEM to model complex geometries with different material properties in the frequency domain [178] and thus it is selected for the purpose of this study.

2.2.3. DIELECTRIC RESPONSE OF A MEDIUM TO AN APPLIED E-FIELD

The alternating E-field in the MHz range of the induction coils will polarize the free and bound charges of the dielectric medium (e.g. tissue) [20]. As a result, dipole moments are formed (i.e dipolar polarization) that rotate to align with the applied E-field. However, this rotation comes with an expense of energy that is converted to heat (i.e. dielectric loss) since thermal agitation opposes the dipole orientation with a phase lag.

The dielectric response of a medium to an applied E-field can be described with its complex relative permittivity [166] as given in Equation 2.2.3.1. Its real part also called dielectric constant (ϵ'_r) is related with the amount of energy stored in the material, whereas its imaginary part (ϵ'') describes the electromagnetic energy dissipation which is proportional to its loss tangent ($tan\delta$) according to Equation 2.2.3.2. As a result we can rewrite the complex dielectric permittivity according to Equation 2.2.3.3 and the ac conductivity according to Equation 2.2.3.4.

$$\epsilon_r^* = \epsilon - j\frac{\sigma}{\omega} = \epsilon'_r - j\epsilon'' \tag{2.2.3.1}$$

$$tan\delta = \frac{\epsilon''_r}{\epsilon'_r} \tag{2.2.3.2}$$

$$\epsilon_r^* = \epsilon'_r(1 - j\,tan\delta) \tag{2.2.3.3}$$

$$\sigma = \omega\epsilon_0\epsilon'_r\,tan\delta \tag{2.2.3.4}$$

Based on the above and employing a capacitor with a lossy dielectric, where A is the area of its plates and d their distance, we can model with lumped circuit elements the admittance of the dielectric medium with a parallel combination of a capacitance and resistance $R_p = 1/G_p$ as given in Equations 2.2.3.5 and 2.2.3.6 respectively. Note that, the capacitance of the dielectric is proportional to the ϵ'_r whereas the parallel resistance inversely proportional to its conductivity which includes both ϵ'_r and $tan\delta$.

$$C_p = \frac{\epsilon'_r \epsilon_0 A}{d} \tag{2.2.3.5}$$

$$R_p = \frac{d}{\omega \epsilon_0 \epsilon_r tan\delta A} = \frac{d}{\sigma A} \tag{2.2.3.6}$$

2.3. POWER LOSSES IN INDUCTIVE LINKS

In order to investigate and discriminate the influence of soft encapsulation on the NRIC link efficiency the apriori consideration of all the power losses in such links is required. Leaving aside the losses related with the power electronics which are out of this study scope, the major power losses in inductive links are briefly discussed below in order to reason the selections made in this study, whereas those related with the soft encapsulation will be further analyzed in the next chapter.

- **Displacement resilience:** The angular and lateral misalignments are strongly dependent on the application and the separation distance between the coupled coils, affecting as already mentioned their coupling coefficient and hence the link efficiency. For example, in cochlear implants the coils are located in close proximity their coaxial fixation is applicable. On the other hand, in applications where the receiver is located out of the body other techniques are utilized. One approach proposed in literature [140, 158] is the utilization of intermediate coil(s) between the primary and the secondary in order to increase their coupling and hence the effective operation distance [15]. However, this approach requires more size in the implantable device and thus is neglected in this study. Other methods proposed by Perkins and Donaldson et. al. [45] includes an optimum diameter for the transmitting coil in order to reduce the displacement resilience. Moreover, the bending movements of the flexible substrates (and encapsulation) will also have an effect on the coils relative position, as studied by Misran et. al. [127] who found a drop of 4.5% in their link efficiency over a 20 mm bending radius of their flexible substrate. In order to decouple the aforementioned losses from this study, two co-axially aligned coils will be assumed that are printed on rigid substrates.

- **Human tissue:** The human tissue can be characterized as an inhomogeneous, non-linear, anisotropic and dispersive medium [142]. Gabriel et. al. [58] explicitly states "biological matter has free and bound charges; an applied electric field will cause them to drift and displace, thus inducing conduction and polarization currents". As a result, the transmitting energy through the human tissue will be attenuated, due to the frequency dependent dielectric losses[1]. According to [74], at frequencies below 20MHz where the dipolar polarization mechanisms are dominant, the tissue attenuation is almost negligible. The aforementioned is validated in a variety of studies [131] investigated this effect, concluding that the SAR limits of the of $SAR_{1g} < 1.6W/kg$ (IEEE C95.1999) are satisfied. As a result, the indus-

[1] The magnetic permeability of the human tissue is almost equal to that of free space and thus the magnetic field through the tissue will not attenuate.

trial, scientific and medical (ISM) radio bands of 6.78MHz and 13.56MHz are most commonly used in NRIC links. In this study that of 13.56MHz will be utilized.

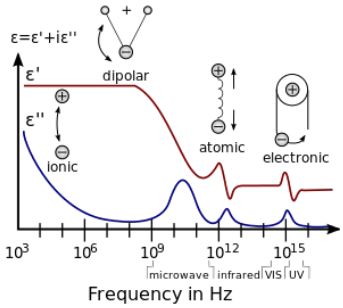

Figure 2.6: Illustration of dielectric permittivity spectrum, where the ϵ' denotes the (real) relative permittivity or the ability of dielectrics to store energy and ϵ'' its imaginary part that relates to power dissipation. The polarization mechanisms from lower to higher frequencies include: a) ionic ($< 10^1 Hz$), b) dipolar or orientational ($\sim 10^1 - 10^9 Hz$), c) atomic ($\sim 10^9 - 10^13 Hz$) and d) electronic ($\sim 10^13 - 10^15 Hz$) polarization [193]. In addition, the dispersive properties of dielectrics are depicted, where at lower frequencies both the conductivity

- **Conductor losses:** The conductor losses of an induction coil includes the DC resistance which is dependent on the conductor trace geometry (i.e width, total length and thickness) and its material properties (i.e resistivity). However, when a high frequency AC current is flowing into the coil, losses from the skin and proximity effect are introduced [47]. More specifically, in high frequencies, the current density through the conductor is concentrated to its outer surface or 'skin', increasing its effective resistance. In addition, the generated magnetic fields of the primary or the adjacent conductors of the secondary will introduce eddy currents according to the Lorentz law which oppose the current flow, increasing the power losses. However, for induction coils implanted within the human tissue, besides the conductor losses, the dielectric losses are expected to increase, as discussed in the next chapter.

2.3.1. SOFT ENCAPSULATION

There are a few studies existing in literature that investigate the impact of soft encapsulation on the electrical properties of induction coils and their link efficiency. Table 2.2 depicts some of the most relevant studies, addressing their encapsulation thickness on top of the coil traces, materials and implantation environments which are the main factors where this study focus.

To start with the most relevant study, Jow and Ghovanloo et. al. [92] demonstrated an optimization procedure for their PSCs including the dielectric properties of the muscle tissue. Also, they varied the encapsulation thickness of both the transmitter and the receiver, from which they found an optimum for their link PDMS of 270 μm. Based on the above, their Q-factor and PTE were degraded in comparison with free-space by 65% and 73% respectively, whereas employing the optimized coils by 25% and 43%. However, the quantification of the soft encapsulation impact in this study wasn't directly coupled

Author	Kim et. al. [101] (@2.765MHz)		Jow et. al. [92] (@13.56MHz)		Ginefri et. al. [67] (@300MHz)
Coil type	Litz wire		PSC		PSC
Coating	Parylene-C (3μm)	Parylene-C (6μm)	PDMS (270μm)		PDMS (35μm)
Environment	PBS	PBS	Muscle	Muscle opt.	Saline
ΔQ-factor	10.6%	0.01%	65%	35%	75%
ΔPTE	-	-	48.2%	38%	-

Table 2.2: Literature review findings for the influence of soft encapsulation on the induction coils and their links.

with its thickness, yet included the influence of the coupling coefficient reduction since the link distance was increased two times the encapsulation thickness.

Moreover, since the focus of this work is coupled with the BEm requirement of miniaturization, it would be relevant to address studies where thin polymers are utilized. As an example, Ginefri et. al. [67] report a 70% reduction in their Q-factor for a PSC encapsulated with a 35μm PDMS that was fully immersed into saline. In addition, Cheng et. al. [31] compared two different PDMS encapsulation thicknesses of 100μm and 500μm and concluded that the electric loading from the surroundings were reduced for the latter. However, they didn't report their influence on the Q-factor and the link efficiency between those. With the same rational, Kim et. al [101] compared the electrical behavior of two litz wire coils inside PBS encapsulated with 3 μm and 6 μm of Parylene-C. From their findings they showed that the latter mitigated the effect of PBS whereas that of 3 μm resulted into a 10.6% drop of its Q-factor.

Of course, although the frequency of operation is low, their results come in a contradiction with the previous findings in literature. For this reason, one can conclude that either the litz wires were coated with an additional ceramic layer, or the dielectric properties of Parylene-C insulate better the coils than PDMS. However, the latter opposes with the dielectric properties shown in Table 2.3, which suggest that the loss tangent of Parylene-C is higher than that of PDMS. Concerning the uncertainty of the dielectric constant findings and their insulation behavior found in literature, it was selected to investigate further the comparison between PDMS and Parylene-C. As a result, since the majority of the BEm candidate have comparable dielectric properties we will investigate if their selection rise additional considerations for the PTE estimation.

Dielectric properties (@1MHz)	PDMS	Parylene-C	Polyimide	LCP	SU-8	PEEK
Relative permittivity (ϵ_r)	3	2.95	3.6	3.7	3.2	3.6
Loss tangent ($tan\delta$)	0.001	0.013	0.031	0.034	0.04	0.03
Moisture absorption (%)	<1	0.06	0.8-1.4	0.03	0.55-0.65	<0.1

Table 2.3: Dielectric properties of potential candidates for the encapsulation of BEms [72], [92]

Concluding, it was shown that the impact of the soft encapsulation is strongly coupled with the coil geometry design, the dielectric properties of the soft encapsulation and the implantation site. Also, it is evident from literature that although the effect of soft encapsulation on the electrical behavior of coils is known, there is no study that includes all the aforementioned factors having as the primary endpoint their impact on

the PTE of a NRIC link when employing thin polymers. Finally, recalling the comparison between the NRIC and US links of Figure 1.3a, where the NRIC links are favored for shallow implantation, there is no study so far that investigates the implantation within fat which will be made in this work.

2.3.2. MOISTURE ABSORPTION

Based on the inevitable saturation of polymers with water vapor, one may wonder how this effect could influence their dielectric properties and further, the electrical behavior of the coils. In literature, there is no relevant study as regards with these type of coils that operate at low frequencies. On the other hand, there are few of those that report a drift over their resonant frequencies (f_r) over time and attribute this effect on the moisture absorption. For example, Warty et. al. [188] reports a f_r reduction of 0.78% on its antenna encapsulated with $400\mu m$ thick PDMS.

Nevertheless, one has to look the properties of the encapsulation materials that are coupled with this effect. Hassler et. al. [72] report the percentage of moisture absorption by mass (%) of different polymers from which one can deduce that Parylene-C (0.06%) outperforms that of PDMS (<1%) since the water vapor content within it is almost negligible. This difference could be reasoned from the molecular structure of each polymer. According to Hill et. al. [75] the degree of the polymers crystallinity affects their mechanical (i.e. density, young Modulus) and barrier properties. As a result, the semi-crystalline structure of Parylene-C that exibits both amorphous and crystalline regions results in a more dense material that favors its low gas permeability, yet its stiffness limits the resulting thickness without being fragile to a few tens of microns [115].

In order to experimentally quantify the change of the polymers' dielectric properties due to the presence to moisture absorption, techniques that combine dielectric (DEA) and solubility analysis are utilized. However, this technique requires the use of special equipment while the polymer under test cannot be deposited on substrates. A more straightforward approach is that of gravimetric analysis where the sample is placed inside a humid environment (e.g. water) and its mass increment is monitored until it saturates (M_{sat}). According to Hayward et. al. [73] the relative permittivity change $\Delta\epsilon'_{sat}$ of a polymer is analogous to the change of its mass (ΔM_{sat}) and as a result the effect of moisture absorption can be directly quantified.

Besides the experimental methods, several analytical models that predict the effective dielectric properties of porous media in the presence of a permeant can be found in literature. Examples include models based on the well established Maxwell-Garnet mixing rule [60] and its variation [156] to study the effect of the permeant size. Other models such that of Lichtenecker's mixture formula that is derived from Maxwell's equations was employed by Curran et. al. [37] who studied the impact of moisture absorption a on a dipole antenna coated with Polyimide. From the simulations performed they concluded that a 2% moisture by mass decreased its f_r by less than 0.2%, while a 4% of moisture sorption by 0.7%.

One other mixing formula is that of Landau-Lifschitz-Looyenga (LLL) [118] which assumes the water vapor absorption to be homogeneously distributed as spherical clusters. Employing this formula, Giacomelli et. al. [65] verified their gravimetric experiments, where the relative permittivity of the utilized Kampton film (M=2%) increased by

0.7%. Based on the above, the mixing formula of LLL will be employed in this study, yet for the experimental verification none of the aforementioned approaches could be utilized due to the need of special equipment. As a result, the input impedance of the coils will be monitored over time and will be verified using the LLL the model.

3

ULTRASONIC POWER TRANSFER

In this chapter, the US link design and its key parameters will be presented. Next, a review around different ultrasonic transducers, their geometry design and the major losses in ultrasonic links will be discussed, focusing on those related with the soft encapsulation. Based on those, a qualitative comparison between the US and NRIC links will be given.

3.1. LINK DESIGN

Ultrasound is a method vastly used in medical imaging, where the propagating through the human body sound waves can capture various tissue characteristics producing an image. The basic principle of diagnostic ultrasound relies on the reduction of the transducers quality factors as a way to enhance their bandwidth. On the other hand, in ultrasonic WPT, transducers with high quality factors should be employed as a way to transduce more energy for the implantable device [32].

Based on the acceptable acoustic attenuation levels and comparable wavelength with the size of the receiver, the idea to use acoustic waves for wireless power delivery has born since 1985. Cochran et. al [34] developed the first ultrasonically powered internal fixation plate that could support bone fractures and accordingly stimulate osteogenesis. The aforementioned experiment spurred a considerable amount of research over the last years that could enable the powering of implants at larger depths, which is the main limitation of NRIC links.

A typical system level design of an US link is illustrated in Figure 3.1. It usually includes a transmitter and in its far-field, the implantable device. The latter consists of an ultrasonic receiver, matching networks, power management electronics (e.g. rectifier) and the application load(s). Under the assumption of operation at resonance though, the matching network can be disregarded (i.e. η_{match}), simplifying the calculation of the soft encapsulation impact on the PTE.

Based on the above, the total PTE of the US link can be calculated according to Equation 3.1.0.1. Among those, we will focus on receiver's aperture efficiency ($\eta_{\text{RX-aper.}}$), since according to [10, 27] it can "capture the effect of the packaging and the interaction of

the acoustic field". However, according to the author's knowledge there is no study that delves into the effect of soft encapsulation, yet other studies [170] argue on its shape which is not the focus of this literature review.

$$\eta_{\text{total}} = \eta_{\text{TX-aper}}\eta_{\text{RX-aper}}\eta_{\text{AC-DC}} \tag{3.1.0.1}$$

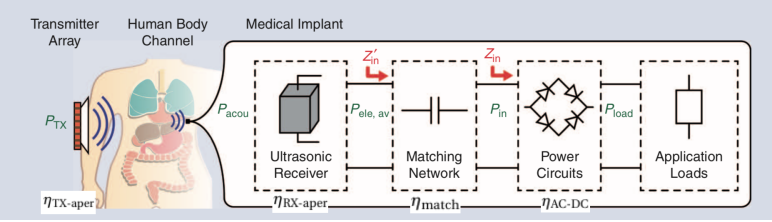

Figure 3.1: Ultrasonic system level design [10].

3.1.1. KEY FACTORS FOR HIGH PERFORMANCE LINKS

The key parameters for efficient US links in energy harvesting applications are listed below:

- **Acoustic impedance** Z_c: The acoustic or characteristic impedance of a material is a function of its density ρ and the sound velocity (v) within it, as given in equation 3.1.1.1. Since US links are based on the propagation of a sound pressure wave, the acoustic impedance of the transmission medium and materials should be carefully taken into account to avoid power reflections in the acoustic domain.

$$Z_{acou} = \rho v \tag{3.1.1.1}$$

- **Electromechanical coupling coefficient** k_{ij}: This coefficient is the ratio of the converted (mechanical) acoustic wave energy to the electrical domain and vice versa (see Equation 3.1.1.2). In energy harvesting applications, a transducer with high k_{ij} coefficient is desired, meaning that more of the excitation energy will be converted to electrical energy. Its value is dependent on the transducer material, volume and the generated strain [32]. However, Prasad et.al [148] states that this coefficient does not represent the actual energy transduction efficiency of the system, since the mechanical or electrical loadings should also be included for its estimation.

$$k_{ij} = \sqrt{\frac{W_{mech-out}}{W_{elec-in}}} \tag{3.1.1.2}$$

- **Mechanical Q-factor**: The mechanical Q-factor is the ratio of the vibrational energy stored (i.e reactance) to the energy dissipated (i.e resistance) during each

mechanical oscillation of the transducer. The Q-factor is strongly coupled with the transducer's energy conversion efficiency and in general, materials with high Q-factor should be selected for energy harvesting applications. However, careful should be given in the fact that datasheets report the Q-factor's value operating in air, which will be influenced from system integration and in-vivo operation. Therefore, its value should be estimated considering all the losses related with the transducer as will be analyzed in next chapters.

$$Q_m = \frac{f_a^2}{2\pi f_r C_0 (f_a^2 - f_r^2)} \tag{3.1.1.3}$$

, where f_r and f_a are the resonance and antiresonance frequency, where the US transducer exhibit minimum and maximum impedance respectively, Z_r is the transducer impedance at resonance (or short-circuit impedance) and C_0 is its intrinsic capacitance.

3.2. ULTRASONIC TRANSDUCERS

The US transducers can be categorized based on their fabrication technology into bulk piezoelectric ceramics and micromachined ultasonic transducers (MUTs). The latter can be further distinguished based on the transduction process into piezoelectric MUTs (pMUTs) and capacitive MUTs (cMUTs).

Starting from the basic principle of the latter, cMUTs employ a thin membrane with an electrode on top and a vacuum cavity in between with its substrate that features the bottom electrode (see Figure 3.2a). When a sound pressure wave is impinged on the membrane surface it is deflected and an AC signal is produced from the change in capacitance of the biased electrodes. The requirement of approximately 100V DC biasing though [98] is the basic disadvantage of cMUTs, since it is not feasible in energy harvesting applications. As a result, efforts to design cMUTs without the need of bias, namely cMUTs in the collapsed mode [44] could be an alternative solution for US energy harvesting.

On the other hand, the piezoelectric ceramics and pMUTs are based on the piezoelectric effect which is the property of crystalline materials to develop charge upon stress or pressure (i.e direct piezoelectric effect) and vice versa (i.e converse piezoelectric effect) [22]. The difference between them relies on the mode of deformation, where the piezoelectric ceramics deform in their thickness or length expansion mode, while the pMUTs in the flexural mode of their thin piezoelectric film (see Figure 3.2b). In order to understand the origin of this effect, one has to look at the molecular level of these materials. When an external force is applied, their crystal structure deforms and is no longer centrosymmetric [175]. This effect leads to ionic charge displacement and as a result, small dipoles are generated. That is to say, the material is being polarized generating an internal electric field that is collected from the deposited electrodes.

The selection between pMUTs and the conventional ceramics is application dependant since both have their own merits. More specifically, pMUTs are fabricated utilizing the MEMs technology and thus, their batch fabrication, miniaturization and integration with electronics and substrates are some of their advantages [5]. On the other hand,

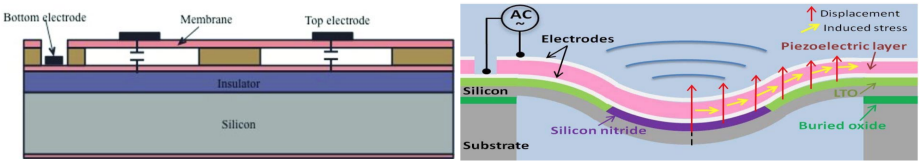

(a) (b)

Figure 3.2: Cross-section of a) cMUTs [48] and b) pMUTs [6].

since the transduced power is dependent on the volume of the piezoelectric material the bulk piezoelectric ceramics can achieve higher efficiencies, progressing them for further analysis in this study.

The piezoelectric ceramics are divided into two groups, the soft and hard ceramics, depending their elastic properties. The former offer the advantage of high piezoelectric charge d and electro-mechanical k coefficients, rendering them suitable for energy harvesting applications [167]. Examples include the widely used transducers based on lead zirconate titanate such as PZT-5H and PZT-5A. However, lead is not biocompatible and therefore materials such as aluminum nitride (AlN), zinc oxide (ZnO), barium titanate ($BaTiO_3$) and lithium niobate ($LiNbO_3$) are alternative solutions [164]. In addition, efforts to increase the k factor with the use of piezoelectric composites are also addressed in literature [134] that are often neglected since they are prone to increased dielectric losses.

3.2.1. GEOMETRY CONSIDERATIONS

The piezoelectric ceramics have to be processed in order to align their random oriented dipoles in a specific direction, a process called poling. During this process, a high DC electric field is applied from the deposited electrodes and leads to a permanent material polarization. The piezoelectric materials due to their anisotropic nature, exhibit different properties along the three orthogonal directions, as shown in Figure 3.3a.

Concerning the aforementioned, the geometry of US transducers and more specifically, their strain and poling direction should be taken into account in order to obtain a higher electromechanical coupling [85]. Between the various geometries, the length expansion (Figure 3.3b and thickness mode (Figure 3.3c) offer the convenience to receive (and transmit) longitudinal waves, generating an electric field that is parallel to their mechanical vibration (i.e 3-3 mode). This effect is also a limiting factor for the MUTs, where the generated E-field is perpendicular to the generated strain (i.e. 3-1 mode). As a result, in this study, US transducers in 3-3 mode will be examined.

Based on the above, the design of US links starts from the geometry design of the US transducers, which determine the operating frequency of the links and the expected converted energy on the implantable device. More specifically, the dimensions and the piezoelectric properties (e.g. acoustic velocity, k_{33}) of the US transducers determine the operating frequency and its aperture size. The latter, introduces the design trade-off between the incident acoustic intensity and the implant size [27]. Based on those, the transducer input impedance Z_{in} is determined and should be matched with the implant

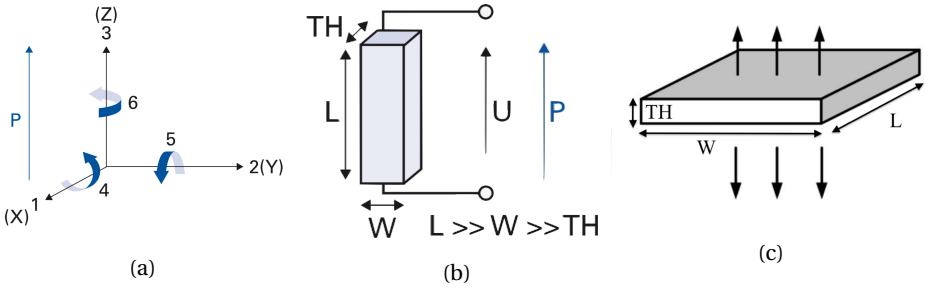

Figure 3.3: a) Coordinate system that describes the properties of polarization and expansion of the US transducers, b) transducer in length expansion and c) in thickness mode.

load for maximum power transfer.

3.2.2. ULTRASONIC TRANSDUCERS MODELING

There are several approaches existing in literature that model the piezoelectric transducers' behaviour. The most commonly accepted among them are the models developed by the pioneer Mason (i.e Mason model) [124], Krimholtz, Leedom and Matthaei (i.e KLM model) [107] and Butterworth Van Dyke (i.e Van Dyke model) [102].

Sherrit et. al. [169] compared the KLM and Mason models and concluded that they are equivalent and describe precisely the response of the ultrasonic transducers. The difference between them is that the former utilizes an explicit transmission line analogy while the latter, a T-network approach [187]. In addition, Mason model employs a not physically realizable negative capacitance in its electrical port imposing modeling constraints [130] that could be bypassed using the modified Mason model of Redwood et. al. [154], enabling its use for simulations with commercial software (e.g. LTspice) [192].

In this study, the Van Dyke model and the KLM model will be described since both can be utilized to study the effect of the soft encapsulation. The former is proposed by the IEEE standard on piezoelectricity in terms of simplicity [175] while the KLM is prefered since it represents better the mechanical properties of multiple matching layers [43, 151].

3.2.2.1. VAN-DYKE MODEL

The frequency response of an ideal piezoelectric transducer can be described near its mechanical resonance by the Butterworth-Van Dyke model (see Figure 3.4a). This circuit utilizes two branches. The electrical branch includes the clamped capacitance of the PZT element and the mechanical one is modeled with a mass-spring-damper system that is equal in the electrical domain, with an LCR resonant circuit as follows:

- C_o is the intrinsic capacitance resulted from the electrodes and the dielectric properties of the PZT transducer.
- C_1 is the motional capacitance, representing the energy introduced to the material when an electric field or mechanical stress (e.g sound pressure wave) is applied.

- L_1 is the equivalent, in the mechanical domain, moving mass of the piezoelectric element.
- R_1 is the motional resistance that illustrates the mechanical energy dissipation.

The Van Dyke model of Figure 3.4b though can be manipulated in order to model a multilayer piezoelectric transducer and hence, the effect of the soft encapsulation can be captured. Based on [175], additional LCR branches (i.e. $R_2L_2C_2$ ... $R_nL_nC_n$) can be introduced in order to model the behavior of additional layers on top of the transducer. Zhang et. al. [197] demonstrated its feasibility, validating the impedance response of their multilayer transducer with FEM. Based on this modified model, Holland et. al. [81] state that the electrical and mechanical losses can also be included when taking into account the complex coefficients of the materials stiffness and permittivity.

3.2.2.2. KLM MODEL

Before describing the KLM model, it is first insightful to address its assumptions and limitations, as reported by Kino et.al.[102]:

- The model is valid under the application of longitudinal waves, which are considered as one-dimensional.
- The ultrasonic receiver is either a large plate (thickness mode) or a thin bar (length expansion mode) so that the stress from their sides (i.e x,y axis) is zero.
- The electrodes are deposited in opposite surfaces along the z direction, parallel to the poling direction, assuming the electric field along the x,y axes to be zero.

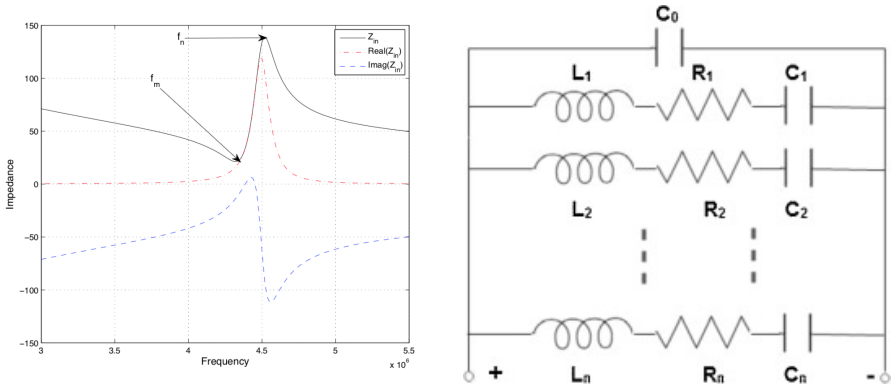

(a) (b)

Figure 3.4: The response of a piezoelectric receiver can be distinguished in three phases. The first one, is below its mechanical resonance (f_m), where the transducer behaves as a capacitor. Next, the point where the receiver is oscillating most readily with minimum impedance is its resonance frequency. From this point, the phase of the transducer impedance is purely inductive, until it reaches the point where its impedance is maximum, or at its anti-resonance frequency f_n. b) Modified Van Dyke model including additional mechanical branches to capture the effect of soft encapsulation and/or additional layers which are noted with the subscripts from 2 to n.

- The model assumes an idealized transducer, without taking into account losses arising from the piezoelectric material and mechanical dissipation due to structural damping or acoustic radiation. However, they could be included by inserting additional elements in the acoustic or electrical ports of the model.

According to [102], the piezoelectric transducer can be represented as a three-port network with two acoustic ports (i.e front and back) and one electrical port. The KLM model in power receiving mode [107] is illustrated in Figure 3.5. In the front acoustic port, a force source is loaded with the front characteristic impedance Z_F, which represents the effective acoustic impedance of the soft encapsulation and tissue on top of the US transducer. The ultrasonic energy is carried through the transducer's acoustic transmission line, with characteristic acoustic impedance Z_C and sound velocity v_o and splitted to the back acoustic port, loaded with the back acoustic impedance Z_B (i.e backing), and the electrical port. In energy harvesting applications Z_B should be close to zero in order to ensure that no power leakage from the transducer backing occurs [10].

Next, the front acoustic port is connected to a frequency dependent transformer, which converts the incident acoustic energy to the electrical domain, the motional capacitance C' and intrinsic capacitance C_0. Finally, the electrical port is loaded with the input impedance $Z_{in'}$ of the power electronics interface.

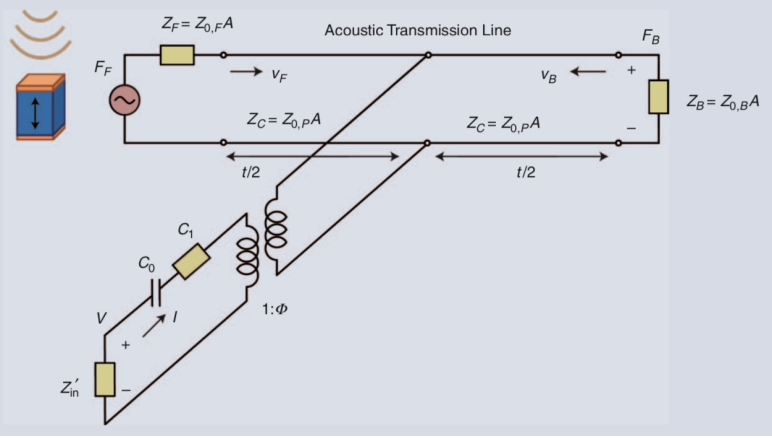

Figure 3.5: Simplified KLM model in power receiving mode [10].

3.3. POWER LOSSES IN ULTRASONIC LINKS

In this chapter the power losses that exist in ultrasonic links will be briefly discussed in a way to decouple their impact from the investigation of the losses related with the soft encapsulation, which will be further analyzed in chapter 3.3.1. The dominant power losses in a US link can be summarized below:

- **Beam divergence:** As a way to enhance and ensure that the transmitted power will be delivered on the receiver interface, Christensen et. al. [33] showed that the ul-

trasonic beam could be larger than the size of the receiver. In addition, Ozeri et. al [138] demonstrated that the optimal distance between the two transducers is the distance where the pressure field converges to a natural focus, which is known as the Rayleigh distance. According to [137] in this distance, the receiver is independent on the transmitter's unstable near-field pressure waves that renders the calculation of the delivered power uncertain.

- **Tissue absorption:** The propagating ultrasonic wave through the human tissue will be attenuated, which refers to the reduction of its amplitude and thus to energy loss. The degree of this reduction is dependent on the tissue attenuation coefficient α which is almost equal for the majority of human tissues [10]. In addition, α is inversely proportional with the operating frequency and the propagation distance (i.e. $dB \cdot MHz^{-1} \cdot cm^{-1}$). Since the resonance frequency is inversely proportional with the transducer thickness, a design trade-off is introduced between the size of the transducer and the tissue absorption. Suzuki et. al [180] argued on the aforementioned and recommended an operating frequency around 1MHz.

- **Support loss:** The support losses are related with the transducer's backing. As a result, when the power receiving transducer is mounted on rigid surface (e.g. substrate), the dynamics of its vibration are influenced and the clamped response of the transducer is leading to the reduction of its Q-factor. Unfortunately, there isn't any study in literature, investigating an optimal mounting solution. Nonetheless, there are some researchers that report these losses. For example, Dongjin et. al [165] state that the experimental validation of their model was not overlapping the analytical results, as the fixture employed heavily dampened the electromechanical transduction of their US transducer, reducing more than 10 times its Q-factor.

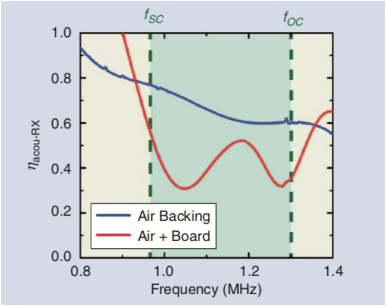

Figure 3.6: Impact of the US transducer integration on a rigid substrate on its aperture efficiency ($\eta_{\text{RX-aper}}$) that is referred in this figure as $\eta_{\text{acou-RX}}$. Image taken from [10].

Arbabian et. al. [10] in an attempt to investigate this issue, compared the operation of its transducer with and without a mounting surface (i.e. substrate) satisfying the air-backing requirement in both cases. From their simulation results (see Figure 3.6), they demonstrated that the aperture efficiency ($\eta_{\text{RX-aper}}$) of the receiver was significantly decreased (approx. 30%) and stated that, it remains a topic that needs further investigation. As a result, in order to investigate the impact of the soft en-

capsulation, the requirement of air backing $Z_{back} \approx 0$ should be satisfied or taken into account before the transducer encapsulation.

- **Front and back electrodes:** Electrodes are deposited on opposite surfaces of the transducer in order to collect the generated charge. Sittig et. al demonstrated [173] that their thickness and bonding materials should be considered and kept small compared to the ultrasonic wavelength, in a way to mitigate their influence on the transducer's impedance.

- **Piezoelectric material losses** There are several loss mechanisms in the piezoelectric materials. Ceramic transducers exhibit dielectric, mechanical (e.g. internal friction, thermoelastic dissipation) and piezoelectric losses, as a result of an applied electric field, stress or the coupling effect between them respectively. There are many authors in literature, studying the transducer losses [81, 183] and their relation with the electromechanical transduction [25, 125, 168], which is on of the key element in energy harvesting applications. Last but not least, the aforementioned losses were investigated [135] for micro-scaled transducers and concluded that bulk material losses are negligible in these dimensions.

3.3.1. SOFT ENCAPSULATION

Biocompatible materials such as PDMS or Parylene-C can be utilized in order to protect the device from the harsh physiological environment. However, to the best of the author's knowledge, the packaging considerations (e.g materials, thickness) and their influence on US links have not been studied in literature, yet their importance has been reported by Arbabian et. al. [10]. The losses related with the soft encapsulation could be summarized as follows:

- **Reflections:** The soft encapsulation could be considered as a matching layer between the ultrasonic transducer (i.e. $Z_c \approx$30MRayl) and the human tissue ($Z_t \approx$ 1.5MRayl). As a result, its acoustic impedance is of primer importance since the power reflections lead in power losses [32]. An effective way to reduce them is to introduce a quarter wavelength matching layer [105], a technique that is vastly used in medical imaging applications. However, this technique reduces undesirably the Q-factor [10, 30, 185] and as a result the aperture efficiency ($\eta_{\text{acou-RX}}$). As a result, the power reflections in US links are often disregarded since the requirement of US transducers with high Q-factors is the primary requirement for efficient links.

- **Acoustic radiation loss** The acoustic radiation loss also known as the added (or virtual) mass effect was introduced by the pioneer J.W. Strutt (a.k.a. Lord Rayleigh) [177] while studying analytically the response of a vibrating disk inside an aqueous environment. The findings of this study showed that the virtual added-mass has a dependency on the transducer's natural frequency of vibration, reducing markedly its resonance frequency (see Equation 3.3.1.1) and introduce more losses. The virtual mass can be described as the inertia added to the transducer as it vibrates and displaces some volume of the encapsulation and the tissue (see Figure 3.7a).

The subsequent experimental study of Lamb et. al. [111] validated Rayleigh's findings and accordingly determined that the corresponding acoustic radiation loss is solely dependent on the characteristic acoustic impedance of the materials.

$$f_{sc} = \frac{1}{2\pi\sqrt{sM_{eff}}} = \frac{1}{2\pi\sqrt{s*(M_{PZT}+M_{v-coat}+M_{v-tissue})}} \quad (3.3.1.1)$$

- **Viscous drag:** Kozlovsky et. al [106] investigated further the previous experiments, studying the medium viscosity contributions on the virtual mass and the energy dissipation at the front of the transducer. Their findings demonstrate that the viscosity of the medium is inversely proportional to the transducer's area and contributes to the Q-factor reduction. Experiments made by [135] showed that when a circular plate transducer was operating in ethanol in comparison with air, the Q-factor became five times smaller, supporting Kozlovsky's et. al. study.

After analyzing the above, we can progress the acoustic radiation loss and viscous drag the primary losses coupled with the soft encapsulation. As already mentioned, the effect of packaging on the US transducers' impedance and their US link efficiency is not studied yet. However, as can be seen in Table 3.1, Chang et. al. [26] report that the losses in their measurements were higher than in calculations, since the latter did not include the influence of the packaging as they are almost negligible. Also they did not report the thickness of the encapsulation, yet state "a thin layer of PDMS is utilized". Notably, for the case of BaTiO3, its ReZ was almost 130% higher than from calculations, whereas the resonance frequency decreased according to the equation 3.3.1.1.

Author	**Chang et. al.** [[26]] (@~1Mhz)								
Encapsulation	"thin layer of PDMS"								
Material	PZT5H			BaTiO3			PZT4		
Method	Calc	Meas	Δ (%)	Calc	Meas	Δ (%)	Calc	Meas	Δ (%)
f_{sc} (MHz)	0.95	0.82	-13.7	1.49	1.45	-2.7	1.06	0.96	-9.4
R_{sc} ($k\Omega$)	1.15	1.74	+51.3	1.94	4.46	+129.9	2.28	2.48	+8.06

Table 3.1: Chang et. al. [29] report the calculated and measured resonance frequency f_sc and resistance R_sc of their US transducers. It is demonstrated that during measurements both of the above deviated (Δ(%) from calculations due to the impact of the soft encapsulation which was not considered in their calculations.

On the contrary, one may argue that the reason that this effect might be negligible is that the employed soft encapsulation was as explicitly stated "a thin (tens of microns) PDMS encapsulation". Thus, its added mass was negligibly small due to the low thickness and acoustic radiation impedance of PDMS (i.e 1.16 MRayl). The question however that arises, is what is the influence of a thicker PDMS encapsulation and what is the difference employing Parylene-C, which has a higher acoustic radiation impedance (i.e 2.84 MRayl). A quick answer for the latter would be that for the same coating thicknesses, Parylene-C will introduce more losses, achieving a lower aperture efficiency.

Lastly, the effect described above should be considered in PZTs with various dimensions, as the effect of added mass will be relatively larger for small PZT transducers. This assumption could be verified from Charchad et. al. findings [27], depicted in figure 3.7b, where the impact of soft encapsulation is more evident at thinner US transducers.

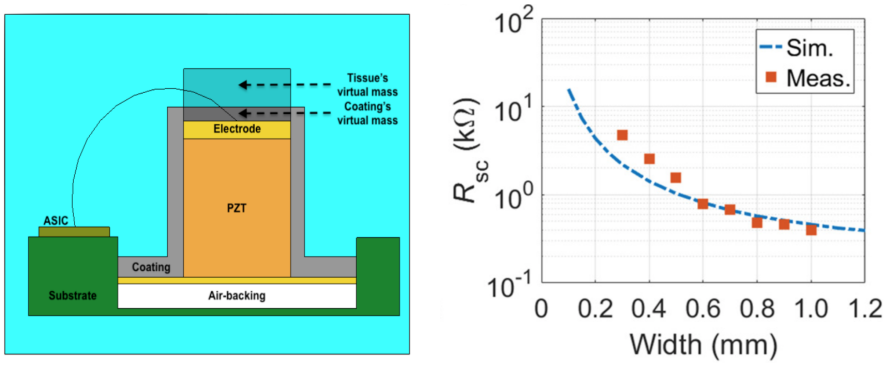

(a) (b)

Figure 3.7: a) Illustration of added mass effect on a PZT transducer (M_{PZT}) from the the tissue ($M_{v-tissue}$) and the soft encapsulation (M_{v-coat}). b) Illustration of the impact of the soft encapsulation on the resistance of an US transducer. It is demonstrated that especially at small transducer's dimensions the effect of soft encapsulation should be considered for accurate results [27].

3.4. CONCLUSION

Considering all the addressed factors in both NRIC and US links, one can elaborate conclusions. Table 3.2 gives a qualitative comparison based on the BEm requirements and the effect of the soft encapsulation.

Starting from the basic requirement of BEms, that of miniaturization, it is evident that US receivers surpass those of NRIC. The induction coils are small compared to the operating frequency wavelength that renders their radiation resistance poor and thus the power energy conversion [30]. On the other hand, US transducers are favoured for miniaturization due to their comparable size with the wavelength at low frequencies.

Moreover, based on the technology aspects and associated power losses presented, one can progress the integration capabilities of PSCs with flexible substrates a more feasible solution that enables the batch fabrication, reducing the fabrication costs of BEms. It was shown that the aperture efficiency of the PZT transducers efficiency is degraded when mounted on a surface, even if the air-backing requirement is satisfied. Hence, alternative receivers that are compatible with MEMS technology such as pMUTs or CMUTs seem more realistic candidates.

Concerning the effect of soft encapsulation and based on the literature review findings it was shown that in in both links, the proper selection of different polymers could lead in a higher WPT link efficiency. Based on the materials focused in this study, we can progress PDMS in both NRIC and US since they exhibit a lower loss tangent and acoustic radiation impedance respectively.

In addition, it was demonstrated that the thickness of the encapsulation materials will have an opposite effect on the behavior of the wireless powered receivers. In the case of NRIC and based on literature, thicker encapsulation materials could effectively mitigate the dielectric losses from the surrounding tissue. On the contrary, thin polymers are selected to encapsulate the piezoelectric ceramic transducers as a way to avoid the

acoustic radiation losses that degrade their Q-factors.

Concluding, it was found that utilizing ultrasound to wireless transfer power to the implant is a method that besides the lower tissue attenuation at larger depths as regards with NRIC links, it is also feasible to realize thin devices, satisfying the fundamental requirement of BEms, that of miniaturization. However, the aforementioned conclusion is purely based on the literature findings and still remains a topic that needs further investigation for the case of US links, since that of NRIC will be investigated further in the next chapters.

Technology aspect	NRIC	US	Comments
Receiver miniaturization	-	+	US transducers are favored due to their comparable size to the incident acoustic wavelength.
System integration	+	-	PSCs could be patterned with high accuracy using MEMS technology. On the other hand, MUTs are progressed over PZTs to satisfy the same criteria.
Soft encapsulation material	+	+	In both WPT links the material selection could lead in higher link efficiencies. From the compared materials we can progress PDMS over Parylene-C.
Soft encapsulation thickness	-	+	In US links, a thin encapsulation should be utilized to avoid acoustic radiation losses, favouring miniaturized BEms.

Table 3.2: Qualitative comparison between the NRIC and US links focusing on their wireless energized receivers and soft encapsulation, where the plus and minus signs depict the advantage and disadvantages respectively.

4

NEAR-FIELD RESONANT INDUCTIVE LINK CHARACTERIZATION

In this chapter, the methodology to study the impact of the soft encapsulation on the inductive link efficiency will be given. Accordingly, the development of an analytical and simulation model will be presented along with the steps followed for their experimental validation.

4.1. ANALYSIS FLOW

In order to study the effect of the soft encapsulation on the PTE of an inductive link, an analytical and simulation model were developed which were validated with experiments. The analysis flow of this work is illustrated in Figure 4.1 and summarized below:

- **Step 1.** The inductive link under investigation is defined, addressing its specifications and assumptions.
- **Step 2.** Coil characterization in air: setting the reference values.
    a) Characterize the electrical behavior of the coil printed on its substrate. Its electrical properties and the PTE in air will be found and compared between the developed models.
    b) Characterize the encapsulated coils with PDMS and Parylene-C comparing the behavior of each model on the soft encapsulation thickness. I t has to be noted that in this study, the encapsulation thickness will be accounted from the top of the coil traces.
- **Step 3.** In-vitro coil characterization using the HFSS model, showing the impact of the following factors on the electrical properties of the coil and the PTE:
    a) Dielectric loading from the surrounding tissue, where the developed simulation model will be compared with the experimental measurements.

b) Soft encapsulation thickness in fat and muscle tissue.

c) Different encapsulation materials, where the insulating behavior of PDMS and Parylene-C will be compared in the aforementioned implantation environments.

d) Moisture absorption.

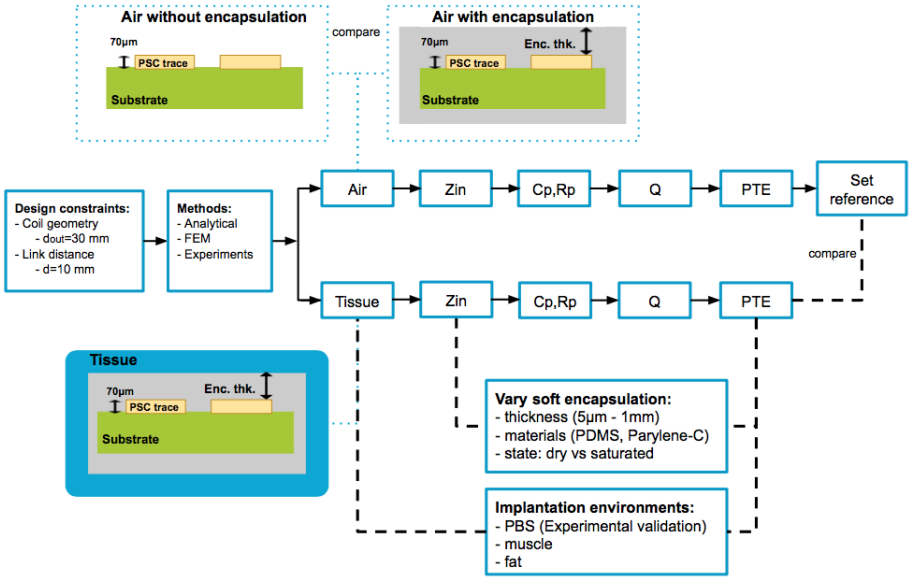

Figure 4.1: Analysis flow, showing the different scenarios under investigation and the methodology steps that were made to relate the effect of the soft encapsulation on the PTE.

4.2. SYSTEM LEVEL DESIGN

The system level design of the inductive link under investigation is depicted in Figure 4.2a and its equivalent circuit model in Figure 4.2b. It is modeled with two coils which both employ the same geometry presented in chapter 2.2.1 and will be assumed to be co-axially aligned over a 10mm distance.

The external coil (primary or TX) operates in air and the implanted (secondary or RX) is encapsulated with soft materials and placed within different tissue environments. These are the fat and muscle tissue, employing the realistic thicknesses of the human forearm [11], whereas the simulation model developed in HFSS will be experimentally validated within a PBS. However, although this environment is not realistic, since its total thickness on top of the secondary will be around 50mm, it will enable the in-vitro coil characterization representing the worst case scenario of dielectric loading. Also, in this work the properties of the tissue will assumed to be homogeneous, isotropic and non-magnetic.

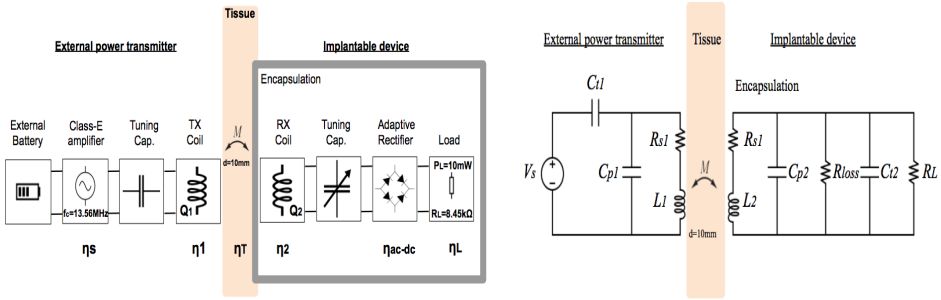

Figure 4.2: a)System level design of the inductive link and b) Schematic diagram of the inductive link with lumped equivalent circuit components, where C_{p2} and R_{loss} represent the total parasitic components from the surrounding environment and materials.

The primary coil is driven by a class-E amplifier with a carrier frequency (ω_0) of 13.56MHz, that generates power from the dc supply of the external transmitter battery. Implantable systems using the NRIC method typically employ capacitors (i.e. C_{t1} and C_{t2}), forming LC tanks that resonate at the same frequency, increasing the voltage gain between them [15]. In order to constantly ensure operation at resonance, adaptive methods have been developed that could be either performed in the primary, adapting the operating resonance frequency to match the detuning of the secondary [172], or with adaptive matching networks at the receiver [99] that ensure resonance at ω_0. In this study, the latter method will be assumed and thus, the C_{t2} will change its value to include the introduced parasitics from the surroundings.

Moreover, the tuning capacitors in NRIC links are usually connected in a series-to-parallel (SP) topology [24], due to the low input impedance at the transmitter and the high output impedance at the receiver that results in more power dissipation at the load, increasing the PTE [15]. In addition, the power is delivered with a low current and high voltage, satisfying the rectifier operation [117] that is usually above 12V DC [163].

Lastly, the load R_L connected in parallel with the tuning capacitor C_{t2} represents the effective load of the implantable device, including the effect of the adaptive rectifier that presents a constant load to the secondary. Based on the above, if $12V$ is required after rectification, the implant voltage requirements should be at least $13V$. Also, selecting 10 mW as the nominal power demand of the implant, the calculation of its load including the effect of the rectifier could be calculated according to Donaldson et. al. [45] as follows:

$$R_L = \frac{V^2}{2P} = 8.45k\Omega \tag{4.2.0.1}$$

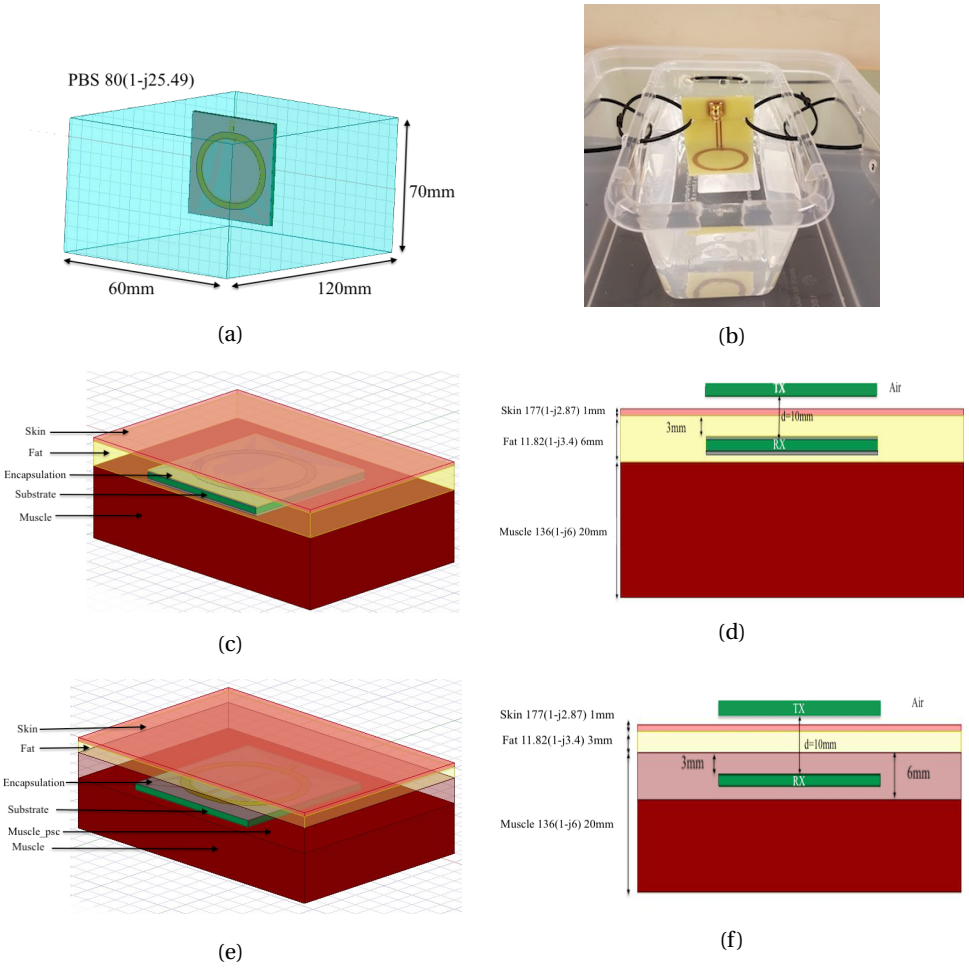

Figure 4.3: Implantation environments under investigation, including a,d) the HFSS model validation in PBS, b,e) fat and c,f) muscle tissue.

4.2.1. POWER TRANSFER EFFICIENCY

One of the quality metrics to assess the performance of a wireless link is its PTE, which is defined [91] as the ratio of the power delivered to the load R_L to the power dissipated at its source (i.e battery), including all the power stages in between. In implantable applications, efficient WPT links are typically preferred since the power losses (i.e heat generation) inside the human tissue are minimized and the life of the transmitter battery is prolonged. However, it should be noted that a high PTE is not meaning a high power delivered to the load (PDL). In this study though, we will focus only in the PTE.

Assuming the design of an efficient class-E amplifier ($\eta_s \approx 1$) and adaptive rectifier ($\eta_{ac-dc} \approx 1$) [120] and concerning the negligible tissue attenuation below 20MHz ($\eta_T \approx 1$), the PTE strongly depends on the partial efficiency of the transmitting (η_k) and the

implanted coil (η_2) as given below:

$$PTE = \eta_s \cdot \eta_k \cdot \eta_T \cdot \eta_2 \cdot \eta_{ac-dc} \approx \eta_k \eta_2 \tag{4.2.1.1}$$

Figure 4.4 illustrates the inductive coupled circuit, in which the implanted device appears as a reflective impedance to the primary [14]. This impedance is dependent on the coupling coefficient $k_{1,2}$ ($\ll 1$) between the coils which can be modeled as a transformer, comprised of the leakage inductance $L_{leak} = (1-k^2)L_1$ ($\approx L_1$) and the magnetized inductance $L_{Tmag} = k^2 L_2$ that represents the magnetic flux coupled with the secondary [113].

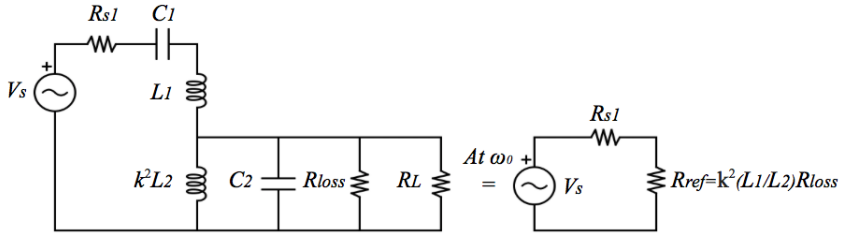

Figure 4.4: Simplified inductive coupled circuit.

Under the condition of resonance at the carrier frequency ω_0, the series $L_{leak}C_1$ tank shorts and the parallel $L_{mag}C_2$ tank opens, where $C_1 = C_{p1}+C_{t1}$ and $C_2 = C_{p2}+C_{t2}$. Thus, the current flowing in the primary will induce a voltage in series with the secondary, which can be seen as a purely resistive (reflected) load R_{ref} which is dependent on the coupling between the two coils (see Figure 4.4). As a result, the energy generated from the primary will be dissipated within its resistive element R_1 and the reflected load R_{ref}.

Moreover, the energy in the implantable device will be dissipated between the load R_L and the total losses of the secondary, modeled with the parallel loss resistance R_{loss}. As a result, a high value of R_{loss} will render more power dissipation to the load, increasing the PTE. Also, the total quality factor of the secondary Q_2' will be influenced from that of the load, where $Q_L = \omega R_L C_2$.

Based on the above, the total PTE will be the product of the primary-secondary efficiency (η_k) and the secondary (η_2) as given in Equation 4.2.1.2, while the reader is prompted to the analysis of Baker et. al. [14] for its derivation.

$$PTE = \eta_k \cdot \eta_2 = \left(\frac{k^2 Q_1 Q_2'}{1 + k^2 Q_1 Q_2'}\right)\left(\frac{Q_2}{Q_2 + Q_L}\right), \text{where } Q_2' = \frac{Q_2 Q_L}{Q_2 + Q_L} \tag{4.2.1.2}$$

4.3. ANALYTICAL MODELING OF INDUCTION COILS

The analytical model developed in MATLAB calculates the electrical parameters of the secondary coil with and without the encapsulation materials. In the equations given below, the numerical subscripts are discarded for simplicity. However, it has to be noted that in order to calculate the PTE, the electrical parameters of the transmitting coil will be the same as the secondary without encapsulation.

4.3.1. COIL IMPEDANCE

Recalling the analysis flow presented in chapter 4.1, the analytical model will be employed in two different scenarios, with and without the soft encapsulation and only in air environment, since it is not valid inside tissue. For both of those, it can be modeled using the equivalent RLC circuit of Figure 4.5, where the self inductance L and series resistance R_s are in parallel with the parasitic capacitance C_p and parallel resistance R_p. The impedance of the coil is given in Equation 4.3.1.1, where the only frequency dependant parameter is that of R_s while the others are constants.

$$Z(\omega) = \frac{R_s R_p + j\omega L R_p}{(R_s + R_p - \omega^2 L R_p C_p) + j\omega(L + R_p R_s C_p)} \tag{4.3.1.1}$$

For the case of the coils without encapsulation, the R_p can be neglected since its value is much larger than the admittance of the capacitor ($R_p \gg X_c$) [133].

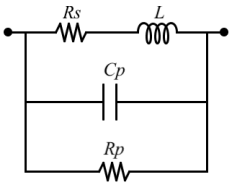

Figure 4.5: Lumped RLC model of the coil input impedance.

4.3.2. SELF INDUCTANCE

The main electrical parameter that characterizes the behavior of the coil is its self inductance. Mohan et. al.[128] gives the following equation for the case of a PSC:

$$L = \frac{\mu N^2 d_{avg}}{2} * \left(ln\left(\frac{2.46}{\phi}\right) + 0.2\phi^2\right) \tag{4.3.2.1}$$

, where μ is the conductor's magnetic permeability, N the number of its turns, $d_{avg} = (d_o + d_i)/2$ the average turn diameter and $\phi = (d_o - d_{in})/(d_o + d_{in})$ the fill factor. This formula calculates the self inductance with an error 8%, under the condition of s<3w, while it looses accuracy when $\phi \leq 0.1$ or $N \leq 2$. According to the geometry of this study, the aforementioned conditions are satisfied.

4.3.3. PARASITIC CAPACITANCE

The parasitic capacitance in free-space including the effect of the substrate only can be calculated using the empirical formula of [91] as follows:

$$C_p = (\alpha\epsilon_{air} + \beta\epsilon_{sub})\epsilon_0 \frac{t_{PSC}}{s} l_g \tag{4.3.3.1}$$

, where $\alpha = 0.9$ and $\beta = 0.1$ are empirical factors, ϵ_{sub} and ϵ_{air} are the relative permittivity of the FR4 substrate and air respectively, t_{PSC} is the conductor thickness and l_g is the coil gap length found from [97].

For the case of encapsulated coils with polymers the method of conformal mapping will be employed. Figure 4.6 shows the cross section of the coil traces, comprised of the substrate and the top encapsulation, satisfying the monotonic increment of the relative permittivity from the top to the bottom materials ($\epsilon_{r1}<\epsilon_{r2}$) [62]. The total parasitic capacitance of the PSC can be found from the superposition of the partial capacitances as oposed to the coil traces:

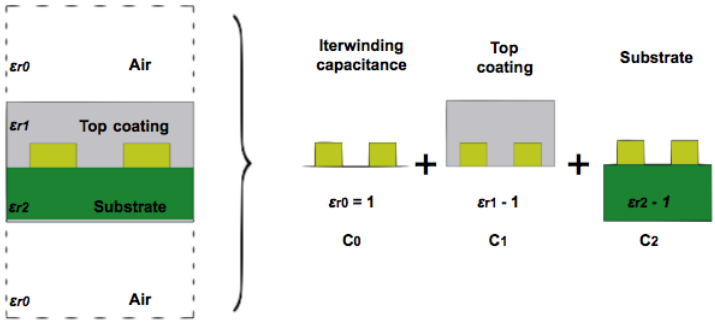

Figure 4.6: Method of conformal mapping, where the total parasitic capacitance is found from the superposition of the partial capacitance of the top and bottom coating and that of the substrate.

$$C_p = C_0 + C_1 + C_2 = \epsilon_{eff} C_0 \tag{4.3.3.2}$$

The parasitic capacitance of the coil in free-space C_0 is given using the Schwartz transformation [63] as follows:

$$C_0 = \epsilon_0 \frac{K'(k_0)}{K(k_0)}, k_0 = \frac{2s}{s+2w} \text{and } k_0' = \sqrt{1-k_0^2} \tag{4.3.3.3}$$

, where $K(k_0)$ is the complete elliptic integral of the first kind. For more information regarding its calculation, the reader is prompted to the work of Gevorgian et. al. [62].

The effective relative permittivity ϵ'_{r-eff} that takes into account the relative permittivities and the thickness of each dielectric layer is given below:

$$\epsilon'_{r-eff} = 1 + \frac{1}{2}(\epsilon_{r1} - \epsilon_{r0}) \frac{K(k_0)K(k_1')}{K(k_0')K(k_1)} + \frac{1}{2}(\epsilon_{r2} - \epsilon_{r0}) \frac{K(k_0)K(k_2')}{K(k_0')K(k_2)} \tag{4.3.3.4}$$

4.3.4. SELF RESONANCE FREQUENCY AND TUNING CAPACITANCE

After finding the inductance and the parasitic capacitance in the previous sections, the SRF of the coil can be found from the following equation:

$$SRF = \frac{1}{2\pi\sqrt{LC_p}} \tag{4.3.4.1}$$

Based on the above and the assumption of maintaining resonance at the secondary, its tuning capacitor C_t is found as follows:

$$C_t = \frac{1}{\omega_0^2 L} - C_p \tag{4.3.4.2}$$

4.3.5. SERIES RESISTANCE

The series resistance R_s of the coil is comprised of the DC and AC losses as given below:

$$R_{series} = R_{DC} + R_{AC} = R_{DC} + R_{skin} + R_{prox} \tag{4.3.5.1}$$

The DC resistance is dependent on the conductor length l_{PSC}, width w and thickness, and the material dependent resistivity ρ, which in this work is copper.

$$R_{DC} = \rho \frac{l_{psc}}{wt} \tag{4.3.5.2}$$

At higher frequencies the current density will be concentrated to its outer surface or 'skin', increasing its effective resistance. The skin effect is dependent on the conductor material, shape and frequency. Analytical expressions that describe the skin effect in various conductor shapes are reported with high accuracy in [54], as follows:

$$R_{skin} = \frac{R_{DC}}{\delta(1 - e^{(-\frac{t}{\delta})})} * \left(\frac{1}{1 + \frac{t}{w}}\right) \tag{4.3.5.3}$$

,where the skin depth δ is found from:

$$\delta = \frac{\rho_c}{\sqrt{\pi f \mu_r \mu_0}} \tag{4.3.5.4}$$

, where μ_0 and μ_r is the magnetic and relative permeability of free-space and copper respectively. In addition, according to the Lorentz law, the generated magnetic fields from the flowing currents will introduce eddy currents to the adjacent conductors. Kuhn et. al [109] investigated the effect of current crowding in spiral coils, giving the following equation:

$$R_{eddy} = \frac{1}{10} R_{DC}\left(\frac{\omega}{\omega_{crit}}\right) \tag{4.3.5.5}$$

,where ω_{crit}, is the frequency at which the current crowding effect begins to become significant:

$$\omega_{crit} = \frac{3.1(s+w)}{\mu_0 w^2} R_{sheet} \tag{4.3.5.6}$$

The equation above though approximates the losses from the proximity effect in IC spiral coils where the skin depth is equal or larger than the conductor thickness. Schormans et. al. [163] investigated this effect and gave an empirical factor for the sheet resistance that is equal to $5m\Omega$ as a way to bypass the introduced errors.

4.3.6. PARALLEL RESISTANCE

The parallel resistance arises from the finite conductivity of the packaging materials, which in our case is the soft materials PDMS and Parylene-C. According to [133], the parallel resistance is found from the equation below:

$$R_p = \frac{t_{enc}}{\sigma_{enc} w l_{PSC}} \tag{4.3.6.1}$$

,where t_{enc} is the thickness of the polymer and σ_{enc} is its conductivity at ω_0 according to Table 2.3, while the w and l_{PSC} is the width and total length of the coil trace.

4.4. DIELECTRIC COMPOSITE MODELING OF COMPOSITE MATERIALS

In order to find the complex dielectric properties of the polymer with the water vapor within it, the mixing formula of Landau-Lifschitz-Looyenga (LLL) that was experimentally validated by [141] is employed. This model assumes that the permeant is introduced inside the dielectric as spherical clusters, and its the equivalent dielectric constant is given as follows:

$$\epsilon'^{1/3}_{ts} = v_w \epsilon'^{1/3}_{w} + (1 - v_w)\epsilon'^{1/3}_{d} \tag{4.4.0.1}$$

,where ϵ'_{ts} is the total complex dielectric constant of the saturated with water vapor polymer, ϵ'_w and ϵ'_d is the dielectric permittivity of the water vapor and dry polymer respectively. Lastly, v_w (v/v) is the volume percentage of water absorption inside the polymer, which is in relation with the percentage of the water uptake by mass m_w (w/w) that is given in the polymer data-sheets and in Table 2.3. The above are related by $v_w = m_w/\rho$, where ρ is the polymer density in g/ml (i.e. $\rho_{\text{PDMS}} = 0.965 g/ml$ [145] and $\rho_{\text{Parylene-C}} = 1.289 g/ml$ [36]).

4.5. FINITE ELEMENT MODELING (FEM) IN HFSS

In this work, a simulation model was developed using the high frequency structure simulator (HFSS v.18). This full-wave simulation software provides both the electric (E) and magnetic (H) fields simultaneously, by solving the Maxwell equations.

The steps that are followed during a simulation using FEM (see Figure 4.7) are given briefly below and in more detail in the following chapters:

- **Step 1:** Draw the geometrical model and assign the material properties.
- **Step 2:** Set the simulation setup and boundary conditions to solve the Maxwell equations for the E and H fields.
- **Step 3:** Subdivide the modeled geometry into small elements, namely the mesh, where the gradient of the fields will be computed.
- **Step 4:** Obtain the electrical parameters (i.e. output variables) of interest.
- **Step 5:** Post-process the results, plotting the fields and the output variables.

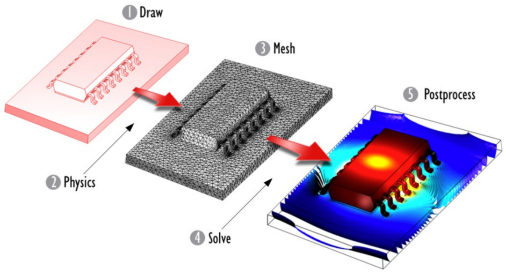

Figure 4.7: Numerical simulation steps in HFSS. Image taken from [8].

4.5.1. DRAWING THE MODEL GEOMETRY

The first step in FEM is to draw the geometry of the simulated element. In this study, the 2D Gerber files of the fabricated PCB design were imported to the HFSS 2D layout package of Ansys electronic desktop. After its import, geometry corrections were automatically applied to improve the volume approximation, as HFSS does not capture efficiently curved surfaces [80]. As a result, the coil was subdivided into 26 segments improving the accuracy of the fields calculation in the given volume.

Next, the 2D layout was exported to the 3D HFSS simulator by setting the appropriate material thicknesses. That of metal conductors was set to t_{psc}=70 μm and that of FR4 substrate to t_{sub} =1.6 mm, generating the coil on top of its substrate. Moreover, the source which generates the flowing currents through the inductor was set by introducing a shorting connection between the two interconnects and assigning a 50Ω lumped port. This step is necessary in order to define the current's return path, satisfying the continuity condition of Maxwell's equations.

The design of the soft encapsulation follows, which was drawn on top and the bottom of the PSC as shown in the cross section of Figure 4.8a. For both polymers its geometry was subdivided into 5 areas. This will enable the mesh seeding in the regions where the E-fields are expected to be stronger and reduces the aspect ratio of the mesh cells [8]. As a result, the first layers called *top_coating_fill* and *bottom_coating_fill* are 70μm

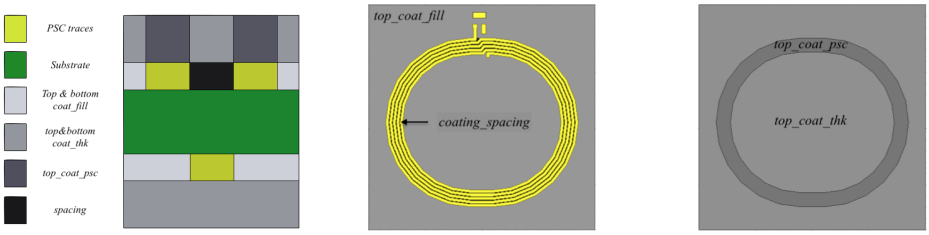

(a) (b) (c)

Figure 4.8: HFSS geometry design in HFSS depicting a) the cross section of the encapsulated PSC with PDMS, b) the PSC top view and c) the top coating view.

thick rectangular boxes on the top and bottom surfaces of the substrate respectively. On top of them, the layers that represent the coating thickness that is going to be swept are drawn ((*top_coating_thk* and *bottom_coating_thk*)) and for the case of the top coating, an additional circular layer on top of the coil traces (i.e. *top_coat_psc*) is defined (see Fig. 4.8c). Finally, an internal coating shape called *coating_spacing* was drawn between the coil traces. It has to be addressed though that for Parylene-C the aforementioned subdivision deviates from reality since it is deposited conformally. However, concerning the introduced errors when a thin sheet was applied it was bypassed.

The dielectric properties of the materials and their thickness are listed in table 4.1. During their assignment, careful should be given in the way that the user inputs the dielectric properties of each material, since in HFSS only the relative permittivity and loss tangent should be specified, whereas the (bulk) conductivity should be defined as zero [49].

Material	FR4	PDMS	Parylene-C	PBS	Muscle	Fat	Dry skin
$\sigma(S/m)$	1.33e-4	2.26e-6	2.89e-5	1.5	0.62	0.03	0.38
ϵ_r	4.4	3	2.95	80	136	11.82	177.13
$\tan(\delta)$	0.04	0.001	0.013	25.49	6	3.4	2.87
$\lambda(m)$	10.54	12.77	12.88	2.47	0.99	4.26	1.16

Table 4.1: Material properties at 13.56MHz, derived from [59] and [92].

4.5.2. SIMULATION SETUP

After constructing the geometry of the simulated structure the solution setup has to be defined. HFSS uses an adaptive algorithm that reconstructs in each iteration the mesh size in each material until the correct field solution is produced based on the maximum change between two iterations of the S-parameters (ΔS). This iteration process refines the mesh based on the wavelength of each material on the solution frequency. Also, an initial mesh size could be defined before starting the simulation for each geometry of interest, a process called seed meshing. As a rule of a thumb, [190] reports that an initial value of $\lambda/4$ for the geometries that need to be described with high accuracy, and thus this rule was set for the different areas of the soft encapsulation described earlier.

In this study, the solution frequency where the fields will be calculated was set to 13.56MHz, as this is the operating frequency of the coil where its Q-factor will be obtained, while the frequency range was set 300kHz-100MHz simulated in steps of 10kHz. The convergence criterion was selected to be ΔS =0.01 and an additional criterion was set for both the ImZ and ReZ part of the coil input impedance, which were restricted to vary by 3% for improved accuracy.

In addition, the following boundary conditions were applied in order to simplify the geometric complexity of the simulated model:

- **Radiation box** By default, HFSS assumes that the solution volume is covered with a perfect electric conductor, rendering the EM model closed. Simulating a radiating element though, an open model has to be defined, where the EM energy can radiate infinitely away from the solution space, approximating the free space. According to the HFSS manual [123], for a week radiating element, the radiation box

should be placed $\lambda/10$ away from the surfaces of the simulated element (i.e. coil). In our case, that leads to a "radiation box" of 2.2 m from each side of the coil as the wavelength at 13.56MHz is 22 m. Therefore, the number of mesh elements will would extremely high, vanishing the available computational resources. In order to compensate that, a "virtual box" which has half the size of the "radiation box" was drawn, improving the accuracy of the mesh in close proximity with the PSC.

- **Finite conductivity boundary** According to Popovic et. al. [147], when the conductor thickness (i.e $70\mu m$) is larger than twice the skin depth (e.g. $\delta = 17$) at the operation frequency, the current density inside the conductor will be exponentially decreased. In this case, the mesh inside the conductor will be extremely small, producing a large number of mesh cells. Instead, the application of the finite conductivity boundary assumes a uniform current distribution from the conductor surface to the skin depth calculating the surface resistance. For this boundary condition, the following formula holds:

$$E_{tan} = Z_s(\hat{n} \times H_{tan}) \tag{4.5.2.1}$$

,where Z_s is the surface impedance that is equal to the plane wave propagating along the z axis into the conductor

$$Z_s = \frac{1+j}{\delta\sigma} = (1+j)\sqrt{\frac{\omega\mu}{2\sigma}} \tag{4.5.2.2}$$

,where δ,σ and μ are the skin depth, conductor's conductivity and magnetic permeability respectively. Also, examining the validity of this boundary condition, the frequency at which the conductor thickness (t_{psc}) is equal or larger than 2 skin depths is found to be 3.53MHz, using the following formula obtained from [153]:

$$f_s = \frac{4}{\pi\mu\sigma t_{psc}^2} \tag{4.5.2.3}$$

4.6. EXPERIMENTAL VALIDATION

The experimental validation of the analytical and HFSS models required a series of actions. These included the fabrication and encapsulation of the coils under test (CUTs) with different polymers (i.e PDMS and Parylene-C) and thicknesses, ensuring accordingly that any reliability issue arising due to contamination or adhesion loss is eliminated. Then a measurement setup for their characterization was developed. The main requirement of this setup was to conduct repeatable and reproducible measurements, which was satisfied after investigating the systematic, drift and random errors.

4.6.1. COILS UNDER TEST (CUTS)

To start with, the CUTs were fabricated from the PCB design of Figure 4.9a. As can be seen, it employs two interconnects with a length similar to the coil diameter, as a way to minimize the parasitic effects from the mounted SMA. The commercial 1.6 mm FR4

substrate was selected for its rigidity and low fabrication costs, as the investigation of flexible or thin substrates was out of this study scope.

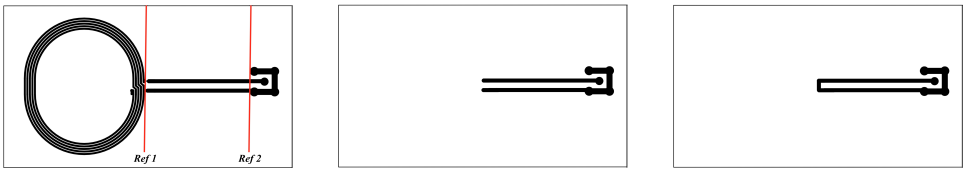

(a) (b) (c)

Figure 4.9: PCB design of a) the fabricated CUTs and their b) open and c) short fixtures for de-embedding.

Accordingly, the interconnects in an open (Fig. 4.9b) and short (Fig. 4.9c) fixture were also realized in order to remove the parasitics added from them and the SMA, as described in the next chapter 4.6.2. In this way, the measured reference plane "ref2" (Fig. 4.9a) after de-embedding will include only the electrical properties of the CUTs in the reference plane "ref1", complying with the analytical and simulation model.

After their fabrication, they were encapsulated with PDMS and Parylene-C of different thicknesses. In each one of them, an identification number (ID) is given as shown in Table 4.2, that reveals their coating material and thickness on top of their copper traces. For example, the sample PC5 translates to a sample encapsulated with Parylene-C with a $5\mu m$ thickness on top of its traces.

ID	Material	Thickness (μm)
UCA	-	0
PC5	Parylene-C	5
PC15	Parylene-C	15
PD35	PDMS	35
PD50	PDMS	50
PD65	PDMS	65
PD360	PDMS	360

Table 4.2: Coils under test with their ID, material and coating thickness measured on top their copper traces.

It has to be mentioned that the initial goal was to have thin encapsulations of equal thicknesses, enabling the comparison between PDMS and Parylene-C. However, for the latter, the maximum thickness that could be deposited within the Else Kooi Laboratory (EKL) was $15\mu m$, whereas the dip-coating process that was utilized for the PDMS encapsulation is uncontrolled as regards with the final thickness.

4.6.2. ONE PORT DE-EMBEDDING

The one port de-embedding technique [104] was utilized in order to decouple the parasitic effects of the interconnects and the SMA from the measured electrical properties of the CUT. More specifically, it will be decoupled from the introduced series inductance ($L1, L2$) and shunt capacitance (C_1, C_2), as shown in Figure 4.10a. Since the latter is in

parallel with the CUT, the admittance (Y) of the open fixture Y_{open} (Fig. 4.10b) is measured and subtracted from the admittance of the CUT, Y_{full}. Next, the series components (L, R_s) are removed by subtracting the admittance of the open fixture Y_{open} from the short Y_{short} . The resulting de-embedded impedance $(Z_{CUT_{de}})$ is found from:

$$Z_{CUT_{de}} = \frac{1}{(Y_{full} - Y_{open})} - \frac{1}{(Y_{short} - Y_{open})} \tag{4.6.2.1}$$

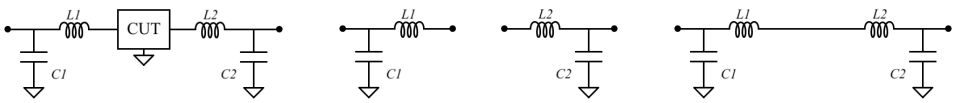

(a) (b) (c)

Figure 4.10: One port de-embedding method, where the parasitics posed to the a) CUTs, were decoupled from the b) stray capacitance and c) self inductance and series resistance.

4.6.3. PDMS DEPOSITION BY DIP-COATING

The procedure of the PDMS encapsulation can be discretized in four phases, that of the cleaning, PDMS preparation, dip-coating and curing process. Recalling that the surfaces where the soft encapsulation materials will be deposited have to be particle-free, the first step of the PDMS encapsulation starts from their thorough cleaning, as shown in Figure 4.11. Initially, the samples were placed in Pyrex dishes and cleaned with an acetone swab to remove the excess solder flux. Then, they were ultrasonically cleaned inside acetone and Isopropyl Alcohol (IPA) for 5 minutes each, at 45°C. After this cleaning process, they were blow dried with a nitrogen gun and placed into the oven for 2 hours at 50°C in order to ensure the moisture evaporation.

Next, the PDMS Nusil MED-6215 was prepared for the dip-coating process. This low viscosity elastomer, is a two-part component kit with a 10:1 (A:B) analogy of Part A, the base, and Part B, the catalyst. Therefore, 8 small containers of 14g:1.4g were weighted

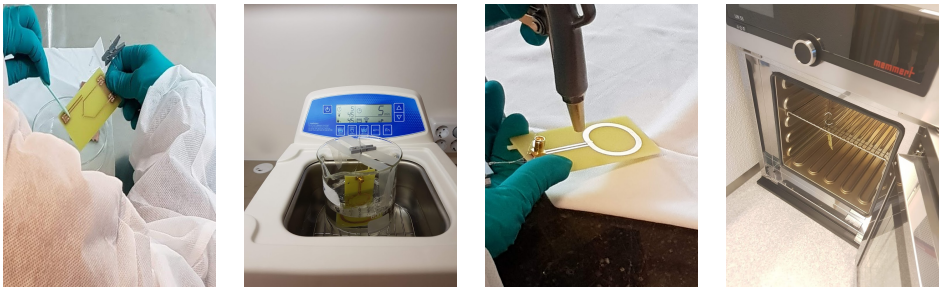

(a) (b) (c) (d)

Figure 4.11: Cleaning process: a) swab the samples' surface with Acetone, b) US cleaning with Acetone and IPA for 5mins, c) blow drying and d) drying for 2 hours at 80°C.

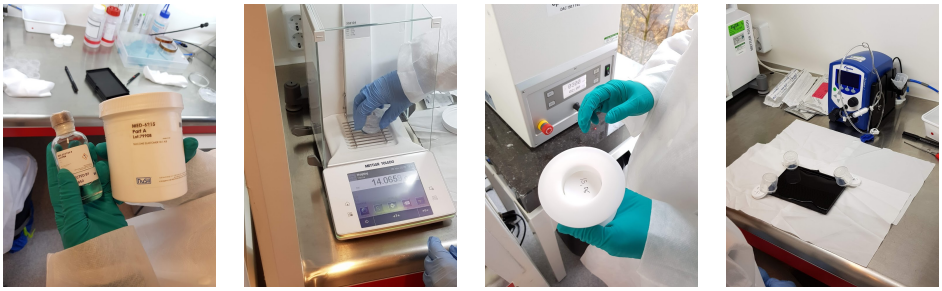

(a) (b) (c) (d)

Figure 4.12: PDMS processing: a) catalyst and base of the utilized PDMS Nusil MED-6215, b) weight measurement, c) speed-mixing for 2min at 2000rpm and d) PDMS pouring into a particle-free container.

and then placed in a speed mixer for 2min at 2000rpm. The thoroughly mixed elastomer is then poured into a particle-free container, where the CUTs were immersed.

Moreover, care should be taken to minimize voids or air bubbles at the interface between the PCB substrate and the encapsulant. Therefore, after the dip-coating process the container was degased into a vacuum concentrator for 1 hour. As can be seen in Figure **??**, at the start of this process a lot of air bubbles are emerged to the surface, while at figure 4 is after 1 hour were the degased PDMS can be observed. Lastly, the samples were carefully released from the degased PDMS container and hanged in order to remove the excess polymer. The time of their hanging determines the resulting thickness of the polymer. More specifically, it was found experimentally, that in order to produce 35,50 and 65μm PDMS thick samples, they were hanging for 30, 20 and 10 minutes respectively. After this time period the samples were cured in the oven overnight at 70C.

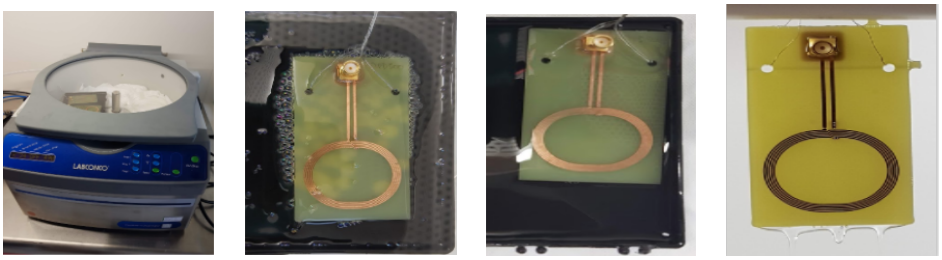

(a) (b) (c) (d)

Figure 4.13: Dip-coating and curing processes: a) degassing, b) bubble formation at the first minutes of the degassing procedure, c) sample after degassing and d) sample hanging to remove excess PDMS and define its final thickness.

Lastly, for the 360μm thick PDMS sample (i.e. PD360), the procedure described above was repeated two times. More specifically, after its initial dip-coating, it was hanged for 5 min. and placed inside the furnace for 30 min. in order to increase its viscosity and make its surface to adhere to the second layer that was deposited repeating the same dip-coating process.

4.6.3.1. PDMS THICKNESS MEASUREMENT

Following the PMDS encapsulation procedure described above, the coating thickness was measured in order to compare the experimental results with that of simulations and calculations. A small incision was made close to the SMA (see Figure 4.15) to ensure that after their immersion into PBS, the solution will not penetrate inside it. Then, a step profilometer was used in the EKL cleanroom facilities and the measurement results depicted in Figure 5.13.

The total encapsulation thickness for the samples PD35, PD50, PD65 and PD360 was found 105.77 μm, 119.40 μm, 135.86 μm and 433.66 μm respectively. However, in this study the coating thickness is specified as the polymer that exists on top of the coil traces, which is reflected to the small bump of the figures at approximately 25 mm distance from the incision point. Concerning the 70μm of the CUT's trace, the coating thickness on top of the traces is 35μm, 50μm, 65μm and 360μm for the samples mentioned before after rounding their thickness for simplicity.

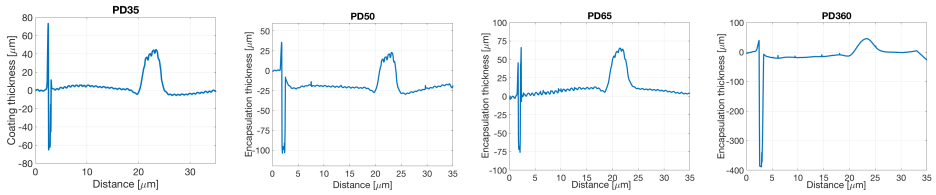

(a) (b) (c) (d)

Figure 4.14: Total coating thickness on top of the CUT: a) PD35, b) PD50, c) PD65 and d) PD360

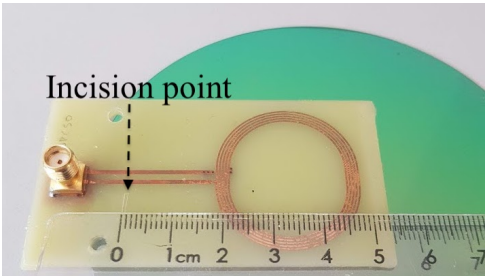

Figure 4.15: PDMS thickness measurement

4.6.4. PARYLENE-C DEPOSITION

For the Parylene-C deposition, the same cleaning process was followed as described in the previous section 4.6.3. The procedure of the polymer deposition was made by chemical vapour deposition (CVD), using the Gorham [69] process of Fig. 4.16 in the facilities of Else Kooi Lab (EKL), TU Delft.

Figure 4.16 illustrates this process, where in the first step (stage 1) the dimer precursor in powder form is heated to change into a vapour state. Then, the vapour is heated

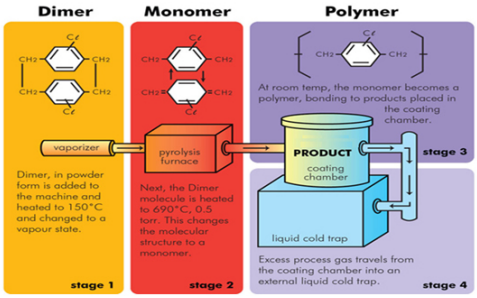

Figure 4.16: Parylene-C deposition process using the Gorham process.

at elevated temperatures (above 550°C), until it vaporizes (stage 2). The outcome is a monomer gas that fills the substrate that exists in the deposition vacuum chamber (stage 3) and is polymerised at room temperature; an advantage that enables its deposition in heat-sensitive substrates without thermal damage. Finally, the excess gas travels from the deposition chamber into a separate container (stage 4).

The resulting thickness of the pin-hole free film is then calculated based on the dimer precursor that was used. In this work, the samples PC5 and PC15 were coated with Parylene-C using 10g and 30g of dimer respectively.

4.6.5. MEASUREMENT SETUP FOR IN-VITRO EXPERIMENTS

The main goal of the developed measurement setup of Figure 4.18a was to make repeatable and reproducible measurements. For the one port measurement of the coils, the network analyzer HP 8753E with a frequency range of 30kHz-6GHz was employed. This type of measurement yields the reflection coefficient S_{11}, from which the impedance of the coils can be calculated as follows:

$$Z = Z_0 \frac{1 + S_{11}}{1 - S_{11}} \tag{4.6.5.1}$$

, where Z_0 is the 50Ω characteristic impedance of the network analyzer port. However, the above equation becomes inaccurate (see Figure 4.17), when the S_{11} is close to -1 or 1. According to [83], when the measured impedance is within the range of 2 Ω to 1.5 $k\Omega$, it is measured with an accuracy of approximately 10%, whereas when its value is close to 50 Ω with 1%.

The aforementioned accuracy though require an adequate calibration (i.e open, short and load) which was made using the high precision HP 85033C calibration kit before starting a series of measurements. Also, in order to reduce the random errors [171] and improve accuracy during measurements and calibration, the intermediate frequency (IF) bandwidth was set to 100Hz and an averaging factor 10 was selected. Also, the network analyzer was warmed up for 2 hours before conducting measurements, in a way to mitigate the drift errors that usually arise from temperature fluctuations of the instrument's electronic components.

Regarding the structure of the measurement setup, an 1m long coaxial cable was fixated on the table so that it is stable during calibration and measurements and in a safe

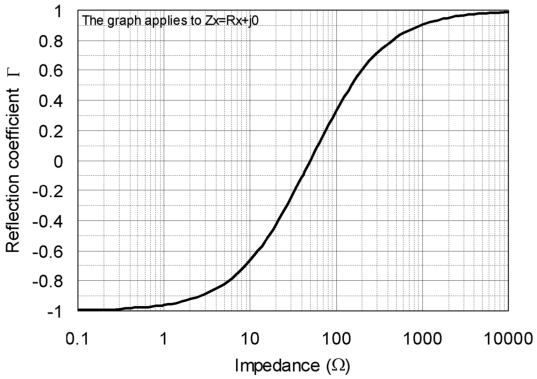

Figure 4.17: Relationship between the reflection coefficient (Γ) and the measured impedance. As shown, the measurement lacks of sensitivity when the measured impedance is much smaller or larger than the characteristic impedance of 50Ω [83].

distance from the network analyzer. Then a big container for protection was placed on the table and a smaller one (60 mm x 120 mm x 70 mm) was mounted within it, where the coils were fixated using plastic straps. The material of these containers is a low density Polyethylene with a low complex dielectric constant of 2.2(1-j0.0001) and therefore the parasitics introduced on the samples expected to be negligible. For the in-vitro measurements, the small containers were filled with 0.5L of 1X PBS (Gibco, pH 7.4) at room temperature so that the coils are covered up to their reference plane "ref 1" (see Figure 4.9a.

Moreover, the distributed elements of the RLC model described in chapter 4.3 cannot be obtained directly during measurements. Instead, its effective series resistance (R'_s) and apparent inductance L' are returned as shown in their RL model of Figure 4.18b, which include the effect of the parasitic capacitance C_p. The parallel equivalent circuit model that will be employed in this study, where the the parallel loss resistance R_{loss} can be found from its series equivalent model [83] using the Equation 4.6.5.2.

In addition, when the parasitic capacitance is comparable with the impedance of the measured electrical component and the SRF is known, the following corrective equations can be used [114]. The aforementioned equations will be employed only in free-space in order to compare them with the analytical model. Finally, it has to be noted that the apparent inductance is measured at 1 MHz and the $C_{\text{p-tot}}$ is found using equation 4.3.4.1, where the SRF is obtained from the frequency where Im(Z) = 0Ω.

$$R_p = R_s(1+Q)^2 \tag{4.6.5.2}$$

$$L = L'\left(1-\left(\frac{\omega}{\omega_0}\right)^2\right) \tag{4.6.5.3}$$

$$R_s = R'_s\left(1-\left(\frac{\omega}{\omega_0}\right)^2\right)^2 \tag{4.6.5.4}$$

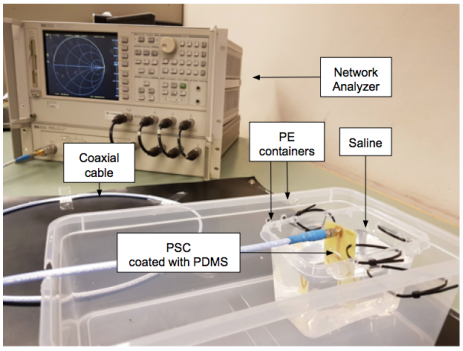

(a)

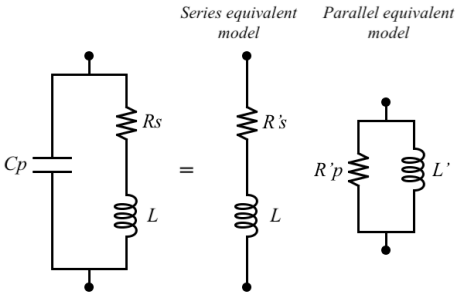

(b)

Figure 4.18: a) Measurement setup, b) Distributed RLC model of analytical methods and its equivalent series and parallel model, obtained during measurements.

5

INFLUENCE OF SOFT ENCAPSULATION

In this chapter, the research questions of this study will be answered. Initially, the coils will be characterized in free-space and then inside the human tissue. In all the aforementioned scenarios, the electrical behavior of the coils will be related to the PTE of the inductive link.

5.1. COIL CHARACTERIZATION IN FREE SPACE

In this section, the electrical properties of the coils will be compared in two different scenarios: a) without (Figure. 5.1a) and b) with soft encapsulation (Figure. 5.1b), where its series equivalent circuit model is depicted in Figure 5.1c. In every scenario the simulation and calculation models will be compared with the empirical measurements, which represent the real behavior of the coil. Before starting the aforementioned comparison though, the steps followed to ensure reproducible measurements will be presented first.

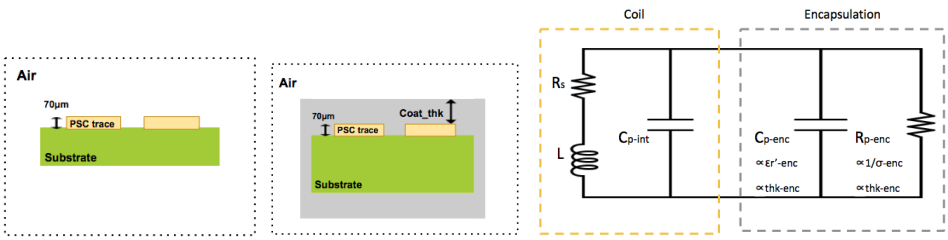

(a) (b) (c)

Figure 5.1: Scenarios under investigation in air environment including a) coil on its substrate and b) encapsulated coil on its substrate. Their series equivalent circuit model is shown in c) where the effect of encapsulation is neglected in the first scenario and that of substrate in both for simplicity. The proportionality factors as regards with the encapsulation thickness (i.e. thk-enc) will be reasoned in the following sections.

5.1.1. INVESTIGATING THE MEASUREMENT REPRODUCIBILITY

The first step of the experimental measurements started from the identification of the systematic and random errors that should rely within a specified margin. Starting from the former, the network analyzer with the 1m coaxial cable were calibrated using the settings of section 4.6.5. Then, the coil UCA was measured, but a repeatable and time invariant error was showing between the frequencies 28-35 MHz. For this reason another coil (d_{out}=20 mm) for WPT was examined, changing also the coaxial cable as shown in Figure 5.2a. In both of these measurements, the same error occurred (see Figure 5.2b), implying that either a systematic error or a form of resonance exists from the measurement setup and will appear in all of the following measurements.

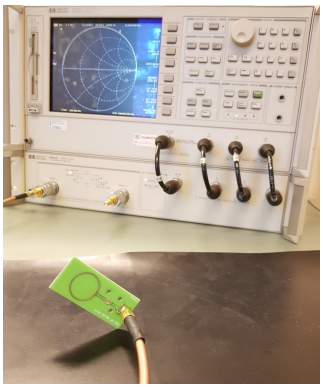

(a)

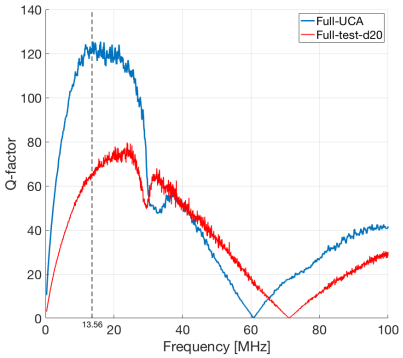

(b)

Figure 5.2: a) Measurement of a different coil for WPT with an outer diameter of 20 mm, employing also a different coaxial cable and b) the same error occurs between the frequency range of 28-35 MHz.

Before analyzing the random errors, the reference plane of the fabricated coils has to include only the inductor and not its interconnects, complying with the other methods (i.e. "ref1"). After performing the one-port de-embedding as described in section 4.6.2, the interconnects and SMA added 26 nH inductance, 75 $m\Omega$ resistance and 2.21 pF parasitic capacitance, as shown in Table 5.1. These values are in an expected range, since the effective inductance loop area of the interconnects is negligibly small, while the effect of their finite conductivity, soldering and SMA is similar to the works of [77, 163].

However, the parasitic capacitance of the de-embedding fixtures is in the same order of magnitude with the inductor's inter-winding capacitance. As a result, the introduced parasitics increased the SRF by 31.87%, from 60.71 MHz to 83.73 MHz, demonstrating that the influence of the interconnects and measurement setup was not negligible. The effect of de-embedding is illustrated in the plot of Q-factor over frequency (see Figure 5.3a), from which one can deduce that indeed, its value is slightly higher at ω_0 after de-embedding, while the biggest the difference occurs at the point it gets zero, or at its SRF.

Next, the measurement relative uncertainty was determined by calculating the mean value of 10 consecutive measurements for the uncoated sample UCA and its difference from the maximum and minimum values. As a result, the ReZ is measured with a relative uncertainty of ± 92 $m\Omega$ (9.38%), while the imaginary part with ± 0.1 Ω, which trans-

Parameter	Full	De-embedded	Rel. Uncertainty (±)	Rel. error (%)
L (μH)	1.47	1.44	0.0015	0.1
Rs (Ω)	1.05	0.98	0.092	9.38
Rp (kΩ)	15.88	15.68	6.87	1.39
Cp (pF)	4.71	2.50	0.01	0.50
SRF (MHz)	60.71	83.73	0.28	0.29
Q-factor	120.07	123.66	5.7	4.61

Table 5.1: In this table the measured (i.e full) and de-embedded values of the coil "UCA" is shown along with the measured uncertainty range and percentage and accuracy.

lates into a ±0.01 pF (0.5%) uncertainty in C_p and ±0.38 MHz (0.29%) in SRF. Lastly, the Q-factor is measured with a relative error of 4.61%. Reviewing the reported errors, the low values of the real part of impedance at ω_0 fall into the already mentioned in chapter 4.6.5 error of 10%. Therefore, when the investigated factors (e.g polymeric materials, surrounding environment, moisture ingress) that can influence the electrical performance of the coil deviate from the reference values by a value that lies within the specified uncertainty, its impact will be assumed negligible, or undetectable.

Lastly, it was ensured that all the fabricated coils before depositing the encapsulation materials had the same electrical properties. Their relative difference was found to be within the measurement uncertainty of UCA, as illustrated in Figure 5.3b. Therefore, their electrical properties in air environment that are shown in the second column of the Table 5.1 represent the reference values upon which the different case studies that follow will be compared.

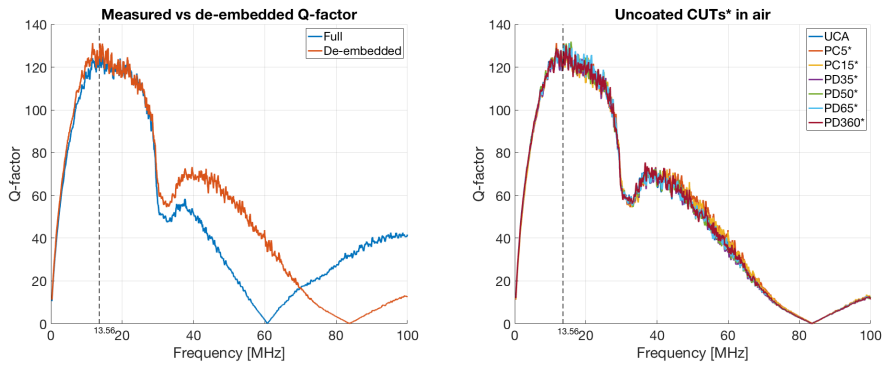

(a) (b)

Figure 5.3: a) Measured vs de-embedded Q-factor of the test sample UCA and b) validating that all coils before encapsulation have the same electrical properties.

5.1.2. EXPERIMENTAL VALIDATION IN FREE-SPACE

Revising the methods followed in this study, the mathematical model employs the calculation of the frequency dependent series resistance and the constant self inductance, ca-

pacitance and parallel resistance. On the other hand, obtaining the coil impedance from the S-parameters during measurements and simulations yields into the apparent inductance, equivalent series resistance (ESR), that will be referred as ReZ, and self resonance frequency (SRF), from which the parasitic capacitance C_p is found. In all methods, the parallel loss resistance of the parallel equivalent circuit is calculated through Equation 2.2.2.1.

The electrical properties of the uncoated coil on its FR4 substrate are listed in Table 5.2, in which the relative difference between simulations and calculations from the measurements is depicted in the columns Δ(%).

Method	**Measurements**	**Simulations**		**Calculations**	
Parameter	Value	Value	Δ (%)	Value	Δ (%)
$L(\mu H)$	1.44	1.39	3.47	1.31	9.03
$R_s(\Omega)$	0.98	0.87	11.22	0.83	15.30
$R_{loss}(k\Omega)$	15.68	16.79	7.08	16.35	4.27
$C_p(pF)$	2.50	2.81	12.40	2.91	16.40
$C_t(pF)$	92.88	96.10	3.47	101.86	9.66
$SRF(MHz)$	83.73	80.35	4.04	81.28	2.93
Q-factor	123.66	136.89	10.70	136.02	9.99
$M(\mu H)$	0.22	0.22		0.22	
$k_{1,2}$	0.151	0.159		0.169	
$\eta_k(\%)$	98.53	98.75		98.93	
$\eta_2(\%)$	64.90	66.41		64.97	
$PTE(\%)$	63.95	65.59		64.27	

Table 5.2: Electrical properties of the coils and inductive link characteristics in free-space between measurements, simulations and calculations.

Starting from the measured, simulated and calculated (apparent) inductance of Figure 5.4a, one can deduce that their values are in good agreement since at 1 MHz they are 1.44 μH, 1.39 μH and 1.31 μH respectively. The latter, is close to the expected 8% accuracy of the equation 4.3.2.1, varying by 9.03% from the measured one. In addition, from Figure 5.4b we can validate the inductive behavior (q=90°) of the coils below their SRF. Note that, the phase angle (q) of the mathematical model does not employ a frequency dependant reactive behavior and thus, it drops abruptly when q becomes resistive (i.e q=0°).

The measured C_p is higher by 12.4% and 16.4% than simulations and calculations respectively that results in a deviation of 4.04% and 2.93% in their SRF. The latter is related with the stray capacitance added to the open measurement fixture during de-embedding, resulting in a lower de-embedded C_p.

Regarding the real part of impedance, one can see in Figure 5.4c that all of the selected methods have the expected frequency response. More specifically, at low frequencies the R_s is relatively low, because the skin depth is thicker than the conductor and thus, the current is evenly distributed inside it. At higher frequencies though, the AC resistance manifests, increasing its value with the square root of frequency ($\sqrt{\omega}$) since the flowing current in the conductor is confined on its edges. Moreover, it is clearly

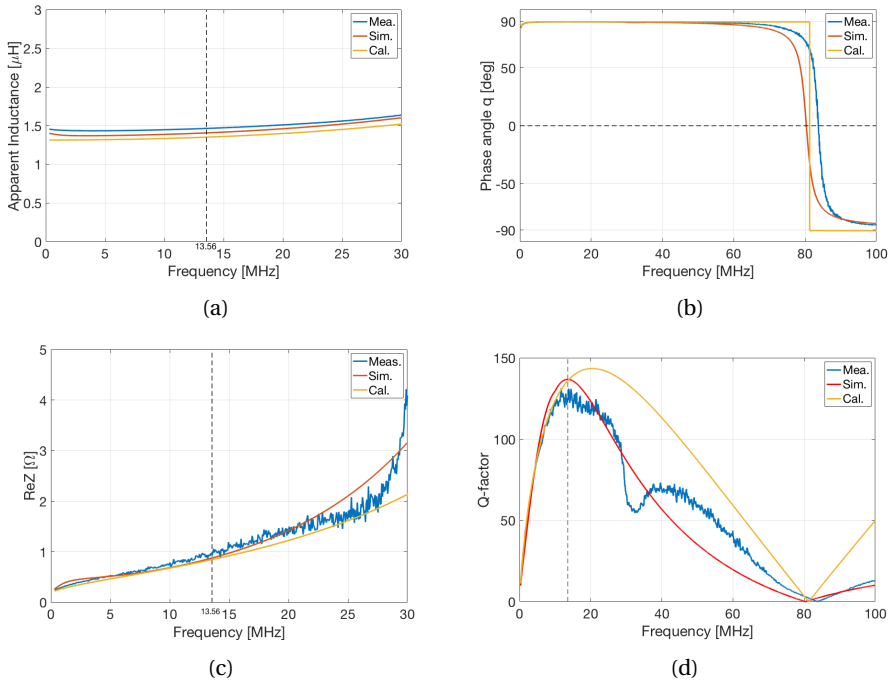

Figure 5.4: Comparison between measurements, simulations and calculations over frequency (300kHz-100MHz) for a) apparent inductance, b) phase angle, c) ReZ and d) Q-factor.

demonstrated that at the operating frequency, the R_s between measurements (i.e 0.98 Ω), simulations (i.e. 0.87 Ω, Δ = 11.22%) and calculations (i.e. 0.83 Ω, Δ = 15.30%) is in reasonable agreement concerning also the reported manufacturing variations for the conductor thickness (i.e. 50 μm-70 μm), surface roughness and conductor shape that result in higher losses [76]. Consequently, the Q-factor from simulations and calculations vary approximately by 10% from the measured Q-factor of 123.66, denoting a good approximation with the real-world behavior of the coil.

Finally, employing the MATLAB script "CuCCo" given by Schormans [162] one can calculate the coupling coefficient and the mutual inductance of the coupled coils, which depends on their (co-axial) alignment and thus its value of 0.22 μH is the same in all methods. Moreover, the slight differences between the measured, simulated and calculated inductance leads to a small deviation in their coupling coefficient $k_{1,2}$, being 0.151, 0.159 and 0.169 respectively. Based on the high $k_{1,2}$, the primary-secondary efficiency η_k is maximized to 98.63% and thus the PTE of the link will be strongly dependent on the efficiency of the secondary η_2. Based on the previous findings and employing the equations of section 4.2.1 the PTE is found to be 63.95% in measurements, 65.59% in simulations and 64.27% in calculations.

5.1.3. INFLUENCE OF SOFT ENCAPSULATION IN FREE-SPACE

In this section, the encapsulated coils with Parylene-C (5 μm and 15 μm) and PDMS (35 μm, 50 μm, 65 μm and 360 μm) will be characterized in air environment. Comparing the results between measurements, simulations and calculations (see Tables B.2, B.1 in Appendix B) will help us to a) study the impact of the encapsulation thickness on the electrical properties of the coil, b) validate that all methods can capture the aforementioned effect and c) understand the uncertainty and accuracy of each model.

Figures 5.5a and 5.5d illustrate the dependency of the encapsulation thickness on the measured, simulated and calculated C_p and ImZ respectively. It is evident that as the soft encapsulation becomes thicker, the parasitic capacitance increases, rendering the ImZ to slightly surge. Note that in calculations different equations were employed for the coil with and without encapsulation and thus, the C_p of sample UCA, is drastically increased from UCA to PC5.

The trend of C_p and ImZ in simulations though is rather fluctuating within the 3% of the additional convergence criteria that was set, as shown in Figure 5.5d. The aforementioned can be reasoned by looking the relative difference of the measured sample PD360 from UCA. Its ImZ deviates by a mere of 2.7% implying that in simulations this difference will be computed within its relative error. In addition, one can notice that the measured sample PC5 has a high C_p (i.e 4.4 pF) that according to the other methods had to be close to that of UCA. The nature of this discrepancy relies on the high aspect ratio of the mesh produced within the soft encapsulation thickness (see Appendix A); an issue

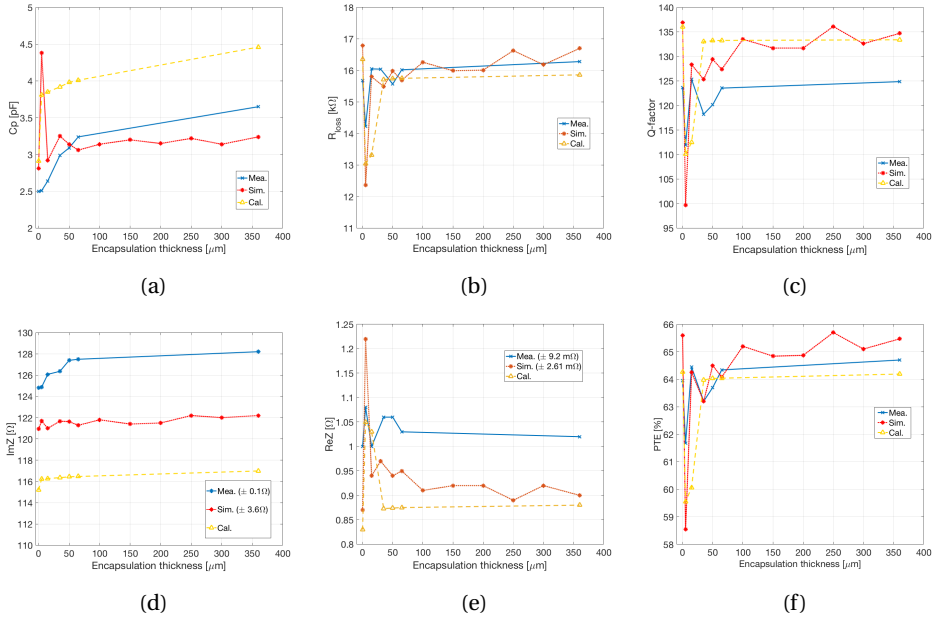

Figure 5.5: Influence of the soft encapsulation in air environment on a) parasitic capacitance C_p, b) parallel loss resistance R_{loss}, c) Q-factor, d) ImZ, e) ReZ and e) PTE.

that according to [123] may lead to erroneous results.

On the other hand, the presence of thin polymers on top of the coil traces introduces minor resistive losses that renders their ReZ at ω_0 to slightly surge from its reference value (i.e. without encapsulation), as shown in Figure 5.5e. This effect can be explained monitoring the parallel loss resistance R_{loss} and leaving aside the erroneous result of the simulated PC5, one can notice that as the encapsulation thickness increases, R_{loss} follows the same trend. The same fluctuating effect is noticed for both ReZ and R_{loss} since it can be seen in calculations that for the PDMS samples, the change on their ReZ is less than 5 $m\Omega$. Lastly, in all methods one can see that for the coil PD360 approaches the reference values of the uncoated coil since it provides a high resistance in parallel with the coil that renders its ReZ unaffected.

Beyond the above observations on the coils input impedance, one has to look these effects on their Q-factor, as a way to analyze the influence of soft polymers on the wireless power reception. Figure 5.5c illustrates that in all methods the presence of thicker encapsulation materials results in a Q-factor that is almost equal to that of UCA, while the thinner encapsulations of Parylene-C result in a Q-factor reduction, complying with the findings of Ginefri et. al. [67]. However, it can be seen that this effect is almost negligible. For example, the PTE of PC15 (Fig. 5.5f) decreased from its reference value by a mere of 0.49%, 1.34% and 4.21% in measurements, simulations and calculations respectively.

5.1.4. CONCLUSIONS

Based on the above, we can draw the following conclusions for the encapsulated coils in air environment:

- The total parasitic capacitance $C_{\text{p-tot.}}$ is proportional to the effective relative permittivity $\epsilon_{\text{r-eff}}$ of the multilayer structure and proportional to the soft encapsulation thickness ($\propto$ thk-enc).

- The parallel loss resistance R_{loss} is inversely proportional to the effective conductivity σ_{eff} and proportional to the soft encapsulation thickness ($\propto$ thk-enc). These proportionality factors are illustrated in the studied parallel equivalent model of the coils as shown in Figure 5.6. However, it has to be noted that the aforementioned factors in this circuit model are only valid in air environment.

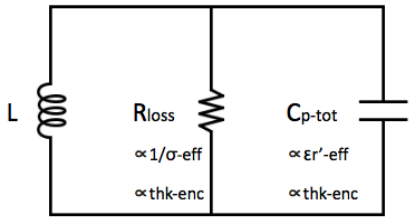

Figure 5.6: Parallel equivalent circuit model in air environment, including the effect of the soft encapsulation.

- The introduced parasitic elements from the soft encapsulation has a negligible effect on the Q-factor of the coils and the PTE in air environment, coinciding with the findings of Kim et. al. [101].
- Comparing the utilized models, the same behavior is obtained as the thickness of the soft encapsulation increases, yet one has to take into account the reported uncertainties of each method.

5.2. IN-VITRO COIL CHARACTERIZATION

In this section, the encapsulated coils will be implanted in tissue (see Figure 5.7a) resulting in the equivalent circuit model of Figure 5.7b. Initially, the insulating behavior of the soft encapsulation will be studied in PBS and accordingly, the HFSS model will be compared with the experimental measurements. After its validation, the investigation in realistic implantation environments (i.e. fat and muscle) follows, where the impact of soft encapsulation thickness, different materials and moisture absorption on the PTE will be given.

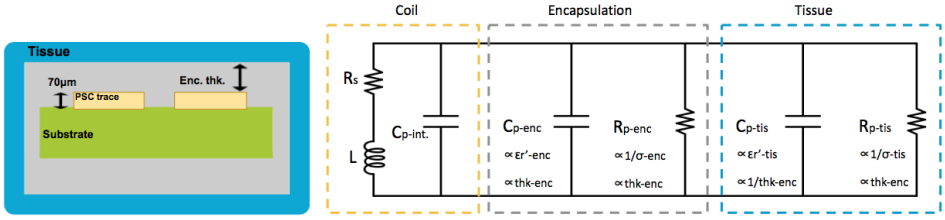

(a) (b)

Figure 5.7: a) Encapsulated coil inside the human tissue b) its series series equivalent circuit model. The proportionality factors as regards with the encapsulation thickness (i.e. thk-enc) will be reasoned in the following sections.

5.2.1. INSULATING BEHAVIOR OF SOFT ENCAPSULATION

Let us now delve to the scenario of encapsulated coils immersed into PBS, which enables the comparison between the developed model in HFSS and the experimental measurements. Figures 5.8a, 5.8b and 5.8c illustrate the measured and simulated SRF, ReZ and Q-factor in PBS over a variable encapsulation thickness, from which the thicknesses of 5 μm and 15 μm refer to the samples encapsulated with Parylene-C (i.e. PC5 and PC15) and the rest with PDMS. In addition, the measured and simulated Q-factors over frequency, along with the electrical properties of the coils and the inductive link characteristics are given in Figure B.1 and Tables B.1, B.2 of Appendix B .

The high relative permittivity of PBS $\epsilon'_{\text{r-PBS}}$ increases the effective permittivity $\epsilon'_{\text{r\_eff}}$ of the coils and as a result, their total parasitic capacitance $C_{\text{p-tot}}$. The latter, leads to a severe reduction of their SRF especially when a thin encapsulation is employed. For example, as can be seen in Figure 5.8a, the SRF of the sample PC5 is lower than the operating frequency in both measurements and simulations and thus, its inductive behavior is vanished ($Q_{PC5} \approx 0$).

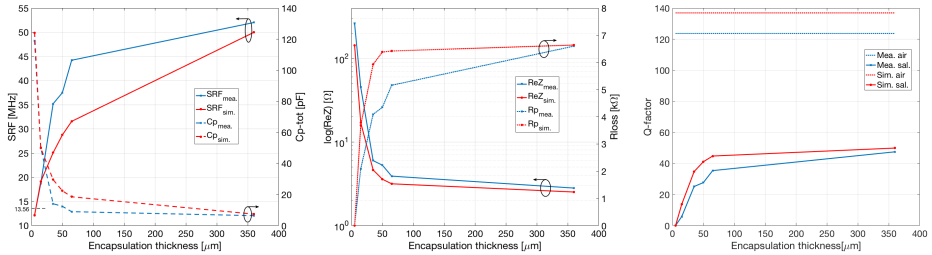

(a) (b) (c)

Figure 5.8: Comparing the electrical parameters a) SRF, b) ReZ and c) Q-factor between the HFSS model and experimental measurements in PBS. It has to be noted that the encapsulation thickness of 5 and 15 microns refer to the samples with Parylene-C and the others with PDMS.

On the contrary, the presence of soft materials on top of the coil traces alleviates the dielectric loading of the surrounding medium, since their relative permittivity is much lower than that of PBS ($\epsilon'_{\text{r-enc.}} < \epsilon'_{\text{r-PBS}}$); an a effect that is strongly coupled with the encapsulation thickness [92]. More specifically, employing thicker polymers, the $C_{\text{p-tot}}$ is drastically reduced (see Figure 5.8a) and hence the SRF levels to higher frequencies, approaching 52.01 MHz in measurements and 48.88 MHz in simulations for the sample PD360.

In the same fashion, the soft encapsulation conductivity is much lower than that of PBS ($\sigma_{\text{enc.}} < \sigma_{\text{PBS}}$). As a result, as the encapsulation thickness is increased, the parallel loss resistance follows the same trend and thus the ReZ is drastically reduced, as shown in Figure 5.8b. Examining the aforementioned for the coil with the thicker encapsulation (i.e. PD360), its Q-factor is significantly higher than the others (see Figure 5.8c), yet still lower from its reference value in air environment, by 61.62% in measurements and 63.56% in simulations.

Summarizing the above, we can state that the soft encapsulation insulates the coils from the surrounding medium. In addition, it was shown that R_{loss} is analogous with the encapsulation thickness, whereas the C_{p-tot} follows the opposite trend. The aforementioned can be illustrated in the parallel equivalent circuit model of Figure 5.9, where the introduced proportionality factors are valid for encapsulated coils inside the human tissue.

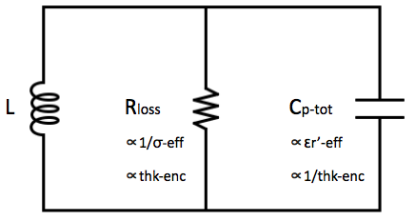

Figure 5.9: Parallel equivalent circuit model in tissue, including the effect of the soft encapsulation.

However, the aforementioned investigation consists the worst case scenario of dielectric loading as already addressed in section 4.2. Thus, the realistic implantation environments of fat and muscle tissue will be investigated further, using the HFSS model. Before analyzing the aforementioned though, we will compare the HFSS model accuracy with the experimental measurements in the next section.

5.2.2. NUMERICAL SIMULATION MODEL (HFSS) VALIDATION

In this section we will argue on the accuracy of the simulation model developed in HFSS. Table 5.3 includes the relative difference of the HFSS model from the experimental measurements listed in the columns $\text{Sim}\Delta_{\text{mea}}$ for SRF, ReZ and the Q-factor of the encapsulated coils under test in PBS. Accordingly, it includes the relative difference of measurements and simulations from their reference values in air environment in the columns "$\text{Meas}\Delta_{\text{air}}$" and "$\text{Sim}\Delta_{\text{air}}$" respectively. Based on the given table we can report the following accuracies:

	SRF			ReZ			Q-factor		
	Mea. Δ_{air}(%)	Sim. Δ_{air}(%)	Sim Δ_{mea}(%)	Mea. Δ_{air}(%)	Sim. Δ_{air}(%)	Sim Δ_{mea}(%)	Mea. Δ_{air}(%)	Sim. Δ_{air}(%)	Sim Δ_{mea}(%)
PC5	85.43	84.91	0.65	26635	30015	45.15	100	100	-
PC15	77.69	76.55	2.19	4502	5084	62.26	95.30	89.97	136.31
PD35	57.97	68.79	28.75	511	582	22.70	79.67	74.60	38.26
PD50	55.21	64.21	23.33	439	507	32.00	77.61	69.96	48.51
PD65	47.21	60.72	28.59	298	348	18.97	71.39	67.30	26.54
PD360	37.88	37.82	4.29	187	223	10.32	61.62	63.56	5.12

Table 5.3: Investigation of the HFSS model accuracy in PBS.

- The SRF is simulated with an accuracy between 0.65% (Δ_{PC5}=0.08 MHz) and 28.75% (Δ_{PC35}=10.12 MHz).
- The ReZ is simulated with an accuracy between 10.32% (Δ_{PD360}=1.79 Ω) and 62.26% (Δ_{PC15}=28.08 Ω).
- The Q-factor is simulated with an accuracy between 5.12% (Δ_{PD360}=2.43) and 136.31% (Δ_{PC5}=7.92).
- The biggest deviation for ReZ and Q-factor occurs for the Parylene-C samples PC5 and PC15, where their SRF is close to the operating frequency.

However, the above difference between measurements and the simulations is hindered due to following factors:

- The dielectric properties of both the PBS and the polymers were not obtained via dielectric spectroscopy, yet from literature. More specifically, the conductivity range of PBS is given between 1.5-1.7 S/m [16, 23, 108], whereas for PDMS different brands of polymers were employed from the literature findings. Also, it is known that the dielectric properties of PMDS is coupled with the variation between the mixing ratio of the base and the catalyst [28] introducing another uncertainty factor.

- The dip coating process results in a non-uniform thickness distribution [4]. Additionally, the thickness of PDMS was defined by a single measurement covering only the first encountered traces proximal to the SMA (see Figure 4.15) and not the whole coil diameter. As a result, the PDMS thickness might be thinner from the reported.

- The mounting method of the coils in the PBS container (see Figure B.1b) could possibly led in a small portion of interconnects covered with PBS. As a result, concerning also the above uncertainty factors, the dielectric loading in measurements was higher than simulations, as can be seen in the figures of section 5.2.1 and the Table B.1 and B.2 of Appendix B.

Concluding, although the HFSS model is not accurate enough with the experimental measurements, it can effectively capture the soft encapsulation thickness. More specifically, it was shown that for the main electrical parameter of interest (i.e. Q-factor), the relative difference from its reference values in air environment (see columns "MeasΔ_{air}" and "SimΔ_{air}") is comparable between the two methods. Hence, we can be confident that the developed HFSS model can be utilized for further investigating realistic implantation environments, that of fat and muscle.

5.2.3. IMPACT OF ENCAPSULATION THICKNESS IN FAT AND MUSCLE TISSUE

In the previous sections it was demonstrated that the dielectric loading from the surrounding environment is evident. However, this effect is highly dependent on its dielectric properties, where the parasitic elements $C_{\text{p-tis}}$ and $R_{\text{p-tis}}$ of Figure 5.7b are a function of the tissue relative permittivity and conductivity respectively.

Figure 5.10 compares the SRF of the encapsulated coils with PDMS in muscle and fat tissue. The latter, has an order of magnitude lower relative permittivity ($\epsilon'_{\text{r-fat.}} = 11.82$) from muscle ($\epsilon'_{\text{r-fat.}} = 136$) and hence, even when a 15 μm PDMS is utilized, the coils could withstand the impact on their SRF with an approximately 50% drop from the air

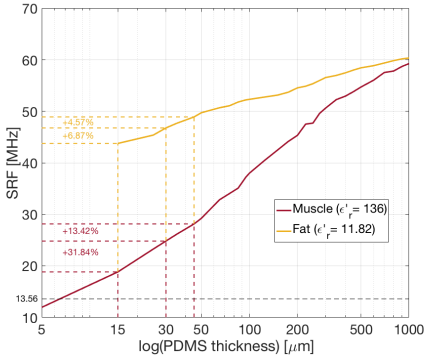

Figure 5.10: PDMS dependency on the SRF in fat and muscle tissue. For the case of fat, the simulated thickness of 5μm did not converged and thus, it is not shown, whereas that of 15 μm was found increasing the convergence criteria to 6 % for ReZ and ImZ.

environment, whereas in muscle approach the ω_0. As a result, it is shown that the influence of the encapsulation thickness is different in these environments. For example, when the PDMS thickness is swept from 15 μm to 30 μm and 45 μm, the SRF in muscle improves by 31.84% and 13.43%, whereas in fat by a mere of 6.87% and 4.57% respectively.

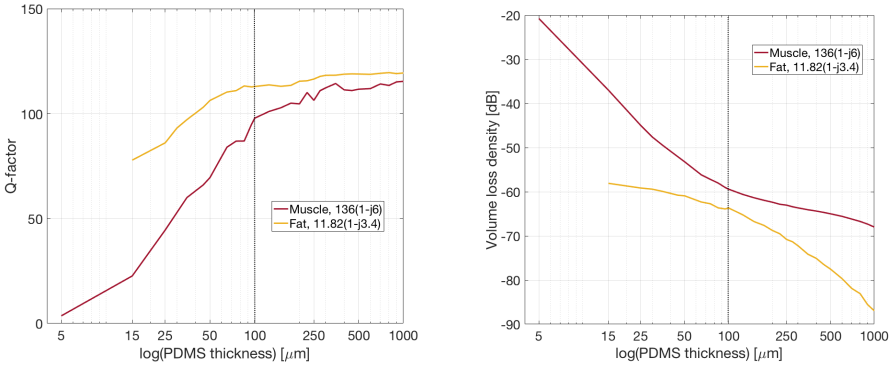

(a) (b)

Figure 5.11: a) Influence of soft encapsulation thickness on the Q-factor and b) volume loss density of dissipated power that is converted into heat, demonstrating the dielectric losses from the surrounding tissue.

Moreover, it was shown in the previous section 5.2.1 that when the parallel loss resistance drops, the total losses (i.e. ReZ) increase. It has to be noted though, that the aforementioned is not attributed with the conductor losses which are the same as the air environment, yet with the dielectric losses. These account the dissipated power that is converted to heat (see Figure 5.11b) within the tissue layers where the coils are implanted.

The aforementioned is reflected on the Q-factor (see Figure 5.11a) of the coils where their degradation within muscle tissue is more severe due to its higher conductivity. Comparing the simulation results with the study of Jow et. al. and Ghovanloo et. al. [92], it is found that at 270μm the Q-factor of their optimized coils was reduced by approximately 35%, whereas in this work by 20%. Obviously, a direct comparison is not valid since different coil geometries were utilized. On the contrary, it indicates a comparable Q-factor reduction, concerning also the fact that in their study the thickness of muscle tissue on top of the coil traces was 50 mm as opposed to the 7 mm (i.e. 3 mm muscle, 3 mm fat and 1 mm dry skin) of this one. As a result, the influence from the surroundings in their study was higher [160].

Moreover, employing the simulated Q-factors of Figure 5.11a and Equation 4.2.1.2, the PTE of the link can be calculated and plotted over a variable PDMS thickness in Figure 5.12. As can be seen, at thicknesses lower than 100μm, the soft encapsulation has a strong dependency on the PTE. As shown previously though, the encapsulation thickness behaves differently in these two implantation environments. As a result, varying the encapsulation thickness from 15 μm to 45 μm with a step of 15 μm, the PTE is enhanced by 4.18% and 2.4% in fat whereas by 12% and 4.18% in muscle respectively. Besides the

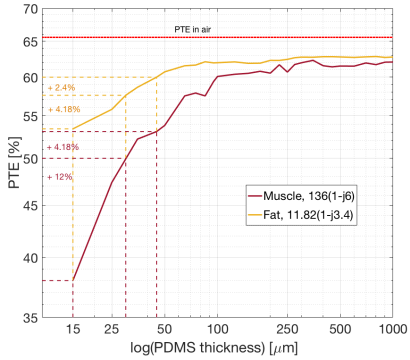

Figure 5.12: Influence of the soft encapsulation thickness on the PTE in fat and muscle tissue.

different behavior though, we can deduce that thin devices with high PTE can be realized in fat tissue, since even with an encapsulation of 15 μm, the PTE dropped by an acceptable percentage of almost 12% as regards with the operation in air environment.

Summarizing the above, it was demonstrated that the consideration of the soft encapsulation thickness should be carefully accounted, especially when the device miniaturization is a priority. Also, it was shown that the impact of the encapsulation thickness is highly coupled with the dielectric properties of the surrounding tissue. Based on the aforementioned, we can argue upon the selections made in study of Ghovanloo and Jow et. al. [92], who state that an optimum encapsulation thickness was found and employed for implantation in both muscle and saline. Based on the findings of this study though, the optimum value of the encapsulation thickness will be different in each implantation site.

As a result, these findings signal the attention during the PTE optimization process. More specifically, we can clearly state that the definition of the inductive link constraints should include a) the dielectric properties of the implantation environment and b) the total volume of the implant including the substrate and the thickness of the coil traces in order to determine the maximum available encapsulation thickness that could be utilized to alleviate the impact from the surrounding medium.

5.2.4. INFLUENCE OF SOFT ENCAPSULATION MATERIALS IN FAT AND MUSCLE TISSUE

As demonstrated in previous sections, as the soft encapsulation thickness is increased the parasitic elements from the surrounding tissue are effectively reduced. This reduction though, besides the dielectric properties of the human tissue, is also a function of the encapsulation relative permittivity (analogous to $C_{\text{p-enc}}$) and loss tangent (analogous to $R_{\text{p-enc}}$), as can be seen in Figure 5.7a. Thus, we will now investigate the aforementioned comparing the effect of PDMS and Parylene-C on the electrical behavior of the coils in fat and muscle tissue.

To start with, since the relative permittivity of PDMS and Parylene-C are almost the same (i.e. $\epsilon'_{\text{r-PDMS}} = 3$, $\epsilon'_{\text{r-Parylene-C}} = 2.95$), their SRF is almost equal. The SRF of the

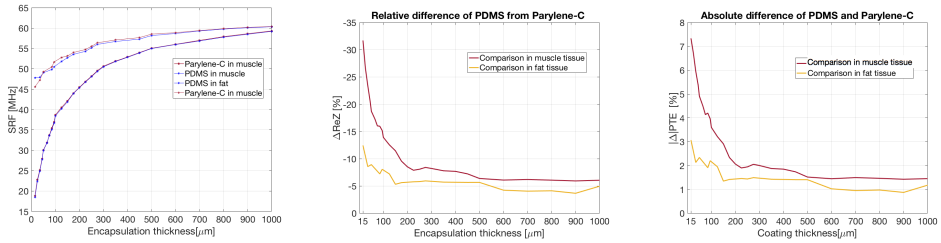

(a) (b) (c)

Figure 5.13: Dependency of the soft encapsulantion materials' a) relative permittivity on the SRF, b) loss tangent on the ReZ and c) PTE within fat and muscle tissue. In all plots, the thickness of 5 μm is neglected since in fat this thickness was not simulated and in muscle, the SRF was below the operation frequency.

coils though does not impact their PTE, yet it matters when it approaches the operating frequency. Concerning the comparable relative permittivity of the polymeric candidates for the BEm encapsulation (see Table 2.3), we can deduce that their selection as regards with the ϵ_r' is not of primary importance.

The biggest deviation between the investigated polymers though is expected in their ReZ, since according to the literature review findings, the lost tangent of PDMS is by one order of magnitude lower (i.e. $tan\delta = 0.001$) than that of Parylene-C (i.e $tand\delta = 0.013$). From Figure 5.13b one could deduce that the difference between them is evident especially below 200 μm. Notably, employing a 15 μm thick PDMS results in even 30% lower ReZ than Parylene-C in muscle tissue, whereas in fat it lies within 12%.

This effect is also depicted in the PTE of the link where employing a 15 μm PDMS results in almost 7.5% more efficient link in muscle and a mere of 3% in fat. At higher thicknesses than 200μm though, the difference in PTE is in the order of 1-2%. As a result, one can deduce that the selection between the polymeric materials should be taken into account only when the coils are placed into a high conductivity environment and if the total encapsulation thickness is restricted, whereas in fat the optimization of the PTE can be decoupled from the material selection.

On the contrary, recalling from section 5.2.3 that the Q-factor within muscle was severely degraded when employing a PDMS encapsulation of 15 μm, we can deduce that the primary concern in the design of a NRIC link is limited to the consideration of the encapsulation thickness.

5.2.5. INFLUENCE OF MOISTURE ABSORPTION

The moisture ingress in the soft encapsulation is expected to alter its relative permittivity and loss tangent. In order to investigate the aforementioned, the SRF and ReZ of the encapsulated coils were compared between their first measurement in PBS ($t_{0\text{-PBS}}$) and after three days ($t_{\text{sat-PBS}}$), assuming their saturation with water vapor that is reported [28] to occur within the first 20 hours.

The results of this experiment did not quantify any changes in the aforementioned electrical parameters which were within the measurement uncertainty of 0.29% for SRF and 9.38% for ReZ. However, this effect could be explained from the fact that the ex-

pected minor changes (as discussed in chapter 2.3.2) are small compared with the parasitics introduced from the surrounding environment. In addition, in a few samples the measurements were not reproducible since a lower ReZ was obtained that could possibly caused due to PBS evaporation.

As a result, another experiment was conducted, where the samples were taken out from the container ($t_{\text{sat-air}}$), wiped with a tissue paper and measured after 1 hour in order to ensure that the excess amount of PBS was not present on their outer surface. Then, their electrical behavior compared with the initial measurements in air environment (t_{0-air}). Figure 5.14a illustrates the findings from the aforementioned experiment from which one could deduce that their loss tangent was unaltered or cannot be quantified, since the ReZ_{sat} of all the samples were measured within the specified error of 9.38%.

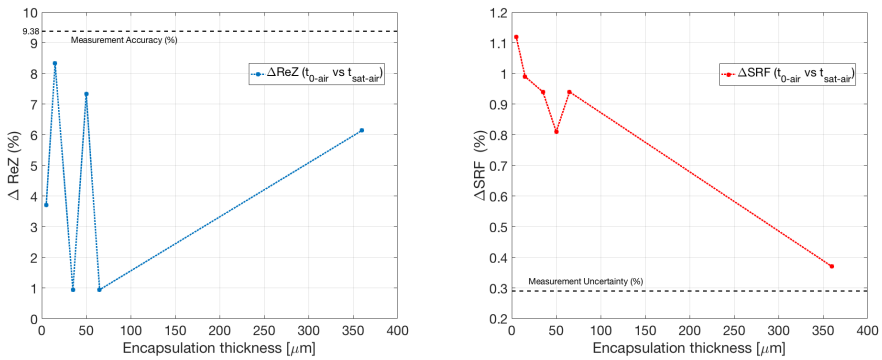

(a) (b)

Figure 5.14: Comparison between air vs air sat.

However, the SRF of all the samples decreased above the accuracy range of 0.29% as illustrated in Figure 5.14b. In addition, it can be noticed that even the least permeable PC5 and PC15 were influenced more than the PDMS samples. In order to explain this effect, we investigate the case of Parylene-C, employing the LLL model to estimate the dielectric properties of the encapsulation assuming their moisture absorption of 0.06% by mass. Next, using the analytical model we can calculate the SRF of PC5 and PC15 which were decreased by a mere of 0.1%, 0.22% respectively and thus, they did not approach the measured relative change on their SRF of 1.15% and 0.99% respectively.

As a result, we could deduce that this effect is not related with the moisture absorption, yet on the presence of PBS on top of the encapsulation. On the contrary we can also claim that the analytical model does not capture accurately the change of the ϵ_r' as regards with the real world measurements. In fact, as observed in Figure 5.5a of Section 5.1.3, the parasitic capacitance in measurements was increased from PC5 to PC15 by 4.92% whereas by a mere of 1.04% in calculations.

As a result, we investigate further this effect in order to reason the smaller deviation of the sample PD360 in comparison with the thinner PDMS samples (i.e. PD35, PD50 and PD65). Figure 5.15 illustrates the estimated (using the LLL model) change of the effec-

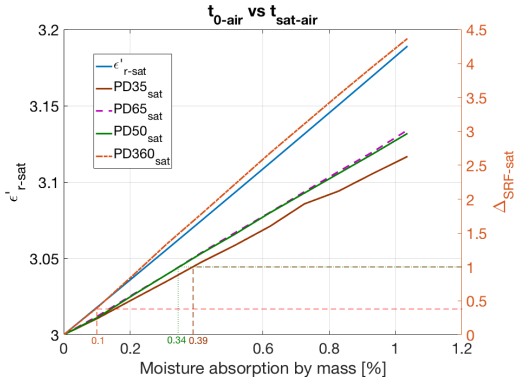

Figure 5.15: Dielectric composite modeling and its comparison with the SRF of the coils.

tive relative permittivity ϵ'_{r-sat} as a function of the moisture absorption by mass, within the given [72] range of 0.01%-1%. Next, employing the analytical, it was found that in order to result in an SRF change of 0.94%, 0.81% and 0.94% for the samples PD35, PD50 and PD65 respectively, the corresponding moisture absorption by mass is 0.39%, 0.34% and 0.33%, whereas for the PD360 a mere of 0.1%. As a result, the moisture ingress in the thicker encapsulation of PDMS was less than the others, resulting in a lower relative change in its SRF.

Concluding, investigating the effect of the moisture ingress within the soft encapsulation materials it was found that a negligible change on the coil SRF and ReZ occurs. As a result, we can state that satisfying a particle-free polymer depositon, the non-hermetic nature of the soft materials does not impact the electrical properties of the coils in their operation frequency and thus, the PTE.

6

DISCUSSION

In this chapter, the selections made during the inductive link design will be revised and the influence of the soft encapsulation upon different design approaches will be given.

6.1. INDUCTIVE LINK DESIGN

Considering the assumptions made in the system level design of the inductive link (see section 4.2), one can quantify design alternatives that can improve the PTE. As a result, we will argue on the influence of the soft encapsulation on the load optimization procedure or when an external coil with a high Q-factor is employed.

6.1.1. LOAD OPTIMIZATION

The power demand of the implantable device was set to 10 mW that resulted in a load of $R_L = 8.45k\Omega$ and a PTE of 65.39% in air environment. However, when the main requirement of the NRIC link is to maximize the total PTE based on a set of coupled coils and their Q-factors, an optimal load can be found as shown by Baker et. al. [14]. Under this condition and employing the same system level design, an optimum load of 1125 Ω for the uncoated coil in air environment (i.e. UCA) can be calculated in order to maximize the PTE to 86.57%, as illustrated in Figure 6.1.

Employing the measured Q-factors of the encapsulated coils into PBS, we will argue on the impact of the soft encapsulation on the R_L optimization. Table 6.1 depicts that indeed, considering the dielectric loading of the surrounding medium and estimating the influence of the encapsulation thickness, the optimum value of R_L is different. Notably, the calculated load for the sample PC15 was half than that of UCA. In addition, it is shown that for all samples the PTE using this method is higher than that of fixed load. For example, the PC15 resulted in a PTE reduction of 34.70% when its optimum load of 480 Ω was utilized in comparison with the other approach which reduced by 50.53%.

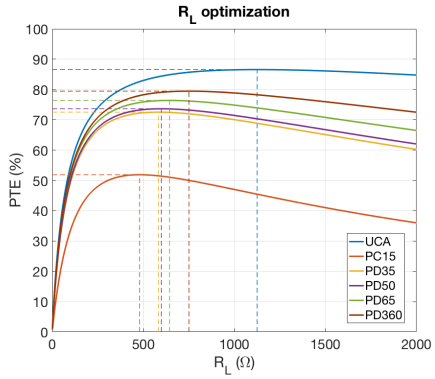

Figure 6.1: Optimum load variation considering the impact of the soft encapsulation and the losses inside the human tissue.

	R_L optimization			$R_L = 8.45k\,\Omega$
	R_L (Ω)	PTE (%)	$\lvert\Delta_{PTE}\rvert$ (%)	$\lvert\Delta_{PTE}\rvert$ (%)
UCA	1125	86.57	-	-
PC5	-	-	-	-
PC15	480	51.87	34.70	50.53
PD35	583	72.52	14.05	34.81
PD50	599	73.64	12.93	33.18
PD65	644	76.39	10.18	28.70
PD360	751	79.46	7.11	22.68

Table 6.1: Absolute difference of the PTE between the NRIC with optimized load versus the case of constant load that provides 10mW to the implant (i.e. 8.45$k\Omega$).

6.1.2. INFLUENCE OF THE EXTERNAL COIL Q-FACTOR

In the inductive link under investigation, we employed an external coil that was coaxially aligned with the secondary and separated over a 10mm distance. This selection rendered a high coupling coefficient ($k_{1,2}$=0.151) that maximized the primary-secondary efficiency η_k to 98.63%. Considering the above and maintaining the same system level design of Section 4.2, we increase the transmission distance to 30 mm in order to reduce the η_k and decouple the dependency of the PTE solely on the efficiency of the receiver η_2. This modification in air environment results into a $k_{1,2}$, η_k and PTE to 0.023, 63.36% and 44.23% respectively.

In addition, we use the scenario of the worst dielectric loading within PBS and vary the Q-factor of the external coil from 135 to 250, 500 and 1000 as a way to investigate the influence of the soft encapsulation in this scenario. Figure 6.2 illustrates the total PTE over a variable Q-factor of the external coil and Table 6.2 their PTE. As it is clearly

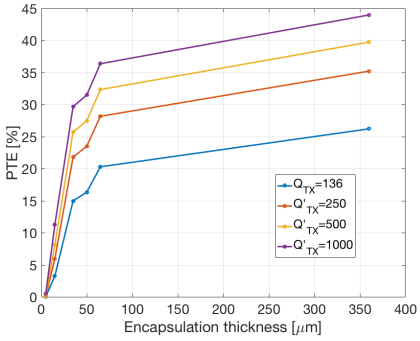

Figure 6.2: Influence of external coil Q-factor.

Q_{TX}	136	250	500	1000
PTE_{UCA}(%)	44.23	53.10	60.31	64.71
PTE_{PC5}(%)	-	-	-	-
PTE_{PC15}(%)	3.27	5.94	8.14	11.27
PTE_{PD35}(%)	14.98	21.82	25.72	29.70
PTE_{PD50}(%)	16.36	23.51	27.49	31.49
PTE_{PD65}(%)	20.31	28.19	32.35	36.38
PTE_{PD360}(%)	26.23	35.23	39.75	43.99

Table 6.2: PTE in air (i.e. UCA) and PBS under a variable Q-factor of the external coil.

shown, the total PTE in all scenarios is slightly improved, yet the degradation from the surrounding environment is still evident and even when an external Q-factor of 1000 is employed and a 360μm thick PDMS, the PTE is still degraded up to ~20%.

Based on the above scenarios on the inductive link design, one can conclude that the effect of the soft encapsulation and especially its thickness should be carefully considered during the PTE optimization of an NRIC link.

7

CONCLUSIONS AND RECOMMENDATIONS

7.1. CONCLUSIONS

Reviewing the research questions of Chapter 1.4 and starting from the primary endpoint of this study, the following conclusions can be drawn:

What is the impact of the soft encapsulation on the near-field resonant inductive coupling (NRIC) link efficiency?

This question constitutes the main goal of this work. The results of the comparative case studies demonstrated it is imperative to include in the link design constraints the dielectric properties of the surrounding tissue and the total volume of the implant, as a way to estimate and/or improve the PTE of the inductive link.

In addition, we can draw conclusions based on the bioelectronic medicine requirements. This work provides evidence that implantation in superficial soft tissue allows the realization of thin devices with efficient links, decoupled from the selection among the BEm polymeric candidates. On the contrary, employing inductive links for deep AIMDs, necessitates the utilization of thick polymers with a low dielectric loss tangent. As a result, this study provides a preliminary conclusion that US links, besides the low attenuation of the acoustic waves, could be further promoted for deep implantation since the quality factors of their ultrasonic transducers are not influenced when a thin encapsulation is utilized.

What is the influence of the soft encapsulation on the electrical properties of the induction coils?

In this study, we demonstrated that the soft encapsulation alleviates the dielectric loading from the surrounding tissue as follows:

- The soft encapsulation relative permittivity is lower than that of tissue. As a result, the effective relative permittivity of the coils drops and their SRF increases, satisfying their inductive behavior.
- The soft encapsulation conductivity is lower than that of tissue, reducing the effective conductivity of the coils. As a result, their parallel loss resistance, quality factor and thus the PTE are improved.

Based on the above, we can conclude that predicting the electrical performance of the coils under in-vivo conditions, the optimization of the inductive link efficiency could be made. The latter is coupled with a series of design choices for the PTE improvement, including the coil geometry or load optimization and the use of an external coil with a high Q-factor.

What is the influence of the soft encapsulation materials and thickness at different implantation environments?

Regarding the influence of the soft encapsulation materials and their thickness it was found that they are coupled with the dielectric properties of the implantation environment. As a result we can draw the following quantitative and qualitative conclusions for implantation in fat and muscle tissue:

- The influence of the soft encapsulation thickness is different in fat and muscle tissue and in addition, it is critical when the device miniaturization is a priority. For example, for thicknesses on top of the coil traces between 15 μm and 100 μm, the implantation in fat resulted in a drop from the air environment ($\Delta_{\text{PTE-air}}$) from 12.5% to 4% respectively, whereas in muscle from 27.5% to 5.5%.
- The impact soft encapsulation materials is also different in fat and muscle tissue and it is critical when employing thin polymers at high conductivity environments. From the comparative studies results, it was shown that utilizing PDMS over Parylene-C and for thicknesses between 15 μm and 100 μm, the PTE in muscle tissue is higher by ~7% to ~3.5%, whereas in fat from ~3% to ~2% respectively.
- Based on the above, we can decouple the link design from the material selection for shallow applications, and in addition we can promote the consideration of the soft encapsulation thickness as the design constraint that should be carefully examined.

Concerning the non-hermetic nature of polymers, what is the impact of moisture absorption on the electrical properties of induction coils?

From the experiments made, we can conclude that the impact of the moisture absorption leads to a negligible impact on the electrical properties of the induction coils at their operation frequency that lies in the MHz range. Satisfying a particle-free polymer deposition, we can state that the Q-factor of the coils remain unaltered and hence, the PTE is decoupled from this effect.

7.2. OWN CONTRIBUTION

In this work, the bioelectronic medicine requirements were initially drawn, the electrical parameters of the induction coils inside the human tissue were extracted, including the influence of the soft encapsulation thickness and different materials. Based on those, the efficiency of the NRIC link was evaluated and as a result, we can draw the following conclusions regarding the novelty of this study:

- Starting from the literature review, an end-to-end comparison regarding the impact of the soft encapsulation on the PTE of ultrasonic and inductive links was given, which according to the author knowledge is not existing in literature. In this comparison, different technology aspects were reviewed, including different types of externally powered receivers, their geometry design and integration feasibility on flexible substrates. Also, the most important losses in the previous links were reported, introducing a methodology that decouples them from the investigation of the soft encapsulation.

- A simulation model in HFSS was developed. Concerning the limited computational power that was available (i.e. 8 GB RAM) and the small simulated sizes (i.e. 5 μm) compared to the wavelength at the operation frequency (i.e 22 m @13.56 MHz), various techniques were applied to reduce the computational demands and model effectively the geometries of interest (i.e. soft encapsulation). As a result, this model can be employed to accurately estimate the performance of the device inside the human tissue, including its system integration and packaging.

- Although a few authors studied the impact of soft encapsulation on the PTE of inductive links, we made an investigation that exploited its behavior in different scenarios. More specifically, realistic scenarios that do not exist in literature were studied, while focusing on the BEm requirement of miniaturization. More specifically, we investigated the a) implantation in fat tissue b) comparison of the PTE over a variable encapsulation thickness and c) comparison of different encapsulation materials which are candidates for the BEm packaging.

7.3. RECOMMENDATIONS FOR FUTURE WORK

Based on the findings of this work and the developed models, the following recommendations can be given as future research proposals:

- In this work, we focused in depth on the the effect of the soft encapsulation in resonant inductive links. However, the same methodology can be applied in order to study its effect on the ultrasonic transducers and their links efficiency, introducing

a novel comparison between these WPT methods as regards with the BEm packaging. Based on the literature review findings in Chapter 3, it seems that utilizing thin polymers the operation of US transducers remains unaltered, whereas the difference between various polymers is expected to be more significant, since their acoustic radiation impedance significantly differs. Also, it was found that the main drawback of the bulk ceramic transducers relies on their integration on flexible substrates which compromise their mechanical vibration. As a result, one could also investigate various transducer integration schemes or to make a comparative study between the aforementioned and pMUTs. In addition, it was found that a FEM software should be employed, since the assumptions made in the analytical transducers models (e.g. KLM model) can not capture these effects. Based on the research made, the software "Onscale" is proposed, since it automatically extracts the dynamics of the transducer in electrical parameters that can be employed to find its input impedance and thus, to estimate the PTE of US links.

- The developed HFSS model could be employed to capture the total losses of the implantable device, considering both the system integration and packaging. For example, thin and flexible substrates can be modeled and their misalignment based on their maximum allowable bending radius can be found. As a result, combining the aforementioned with the findings of this study the total expected variations in the PTE can be estimated and its optimization can be realized finding an optimum combination between the technology aspects and the coil geometry design. For the latter, the Q-factors computed in this study could be employed in order to optimize their geometry in fat or muscle tissue.

- Based on the uncertainty factors of the developed measurement setup and the samples under test, one can realize a dedicated in-vitro test setup. More specifically, the PDMS thickness can be deposited with methods such as spin-coating where its total thickness would be known. In addition, the coils can be fabricated on thin and flexible substrates, whereas dielectric spectroscopy can be applied for the materials which dielectric properties are uncertain. In addition, interdigitated capacitors (IDCs) can be employed to study more precisely the effect of moisture ingress, extracting the variation of the polymer's dielectric properties. Finally, realistic tissue phantoms can be realized and a better mounting solution for the coils inside them can improve the measurement accuracy as regards with the developed models. Finally, the external coil can also be included in order to enable the in-vitro inductive link characterization.

A

INSPECTING THE MESH OF THE SIMULATED SOFT ENCAPSULATION

In Section 5.1.3, the simulation of the coil employing a 5 μm PDMS resulted in erroneous results in the estimation of ImZ. In order to investigate this behavior, the mesh for encapsulation thicknesses of 5 μm, 15 μm and 360 μm is illustrated in Figures A.1a, A.1b and A.1c respectively. As already mentioned in Section 4.5.1, the soft encapsulation was discretized among others to an area between the coil traces (i.e. "spacing") and one that represents its thickness (i.e. "top_coat_thk").

Figure A.1 illustrates that for the spacing between the conductor traces, the aspect ratio is relatively small and more than 2 mesh cells were produced in its volume. On the contrary, it is shown that for the encapsulation thickness of 5 μm, only 2 mesh cells were produced in the "top_coat_thk" which also have a high aspect ratio. According to the HFSS manual [8] this may lead to the unexpected results, as observed in Section 5.1.3. In addition, it is shown that at higher thicknesses the aspect ratio was significantly smaller with more mesh cells. For example, when the thickness was 360 μm, the number of the mesh cells produced on the encapsulation thickness were more than 6. As a result, the meshing of the air on top of the encapsulation was also captured more accurately.

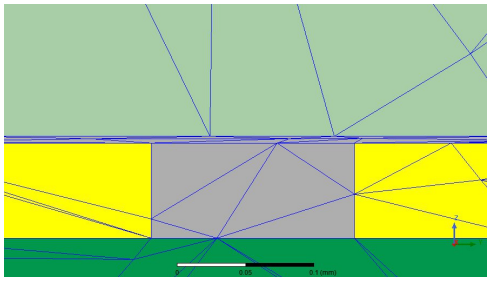

(a)

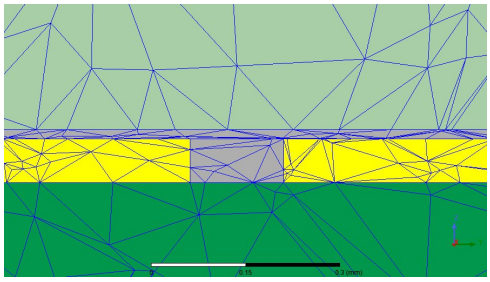

(b)

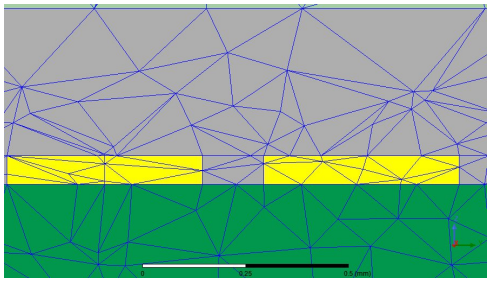

(c)

Figure A.1: Mesh size for PDMS encapsulation of a) 5 μm, b) 15 μm and c) 360 μm thick. From the top to the bottom are depicted the following: substrate in green, coil traces in yellow, encapsulation spacing and encapsulation thickness (i.e. "top_coat_thk") in gray, whereas the light green color on top of the encapsulation thickness represents the surrounding air.

B

EXPERIMENTAL MEASUREMENTS IN PBS

In the following tables and figures, the detailed results of the different case studies of Chapter 5 are presented.

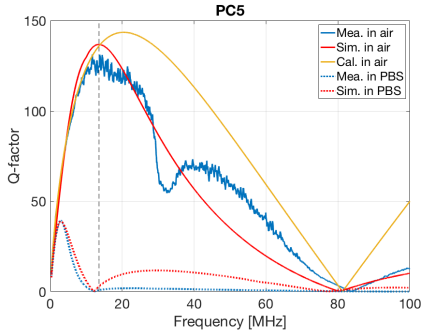

(a)

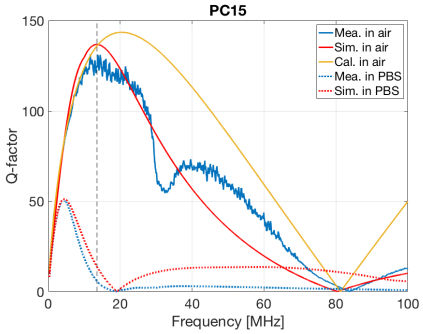

(b)

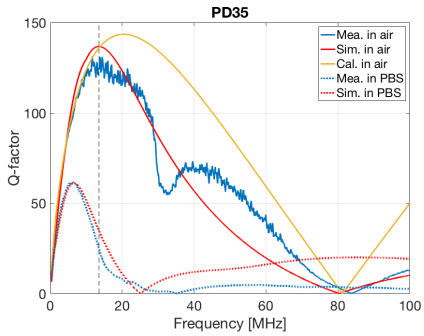

(c)

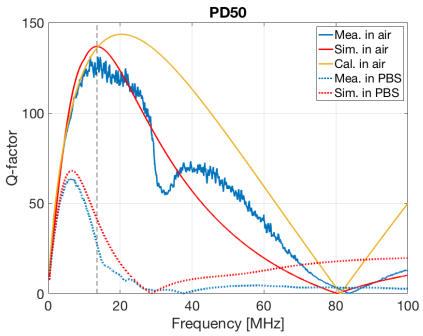

(d)

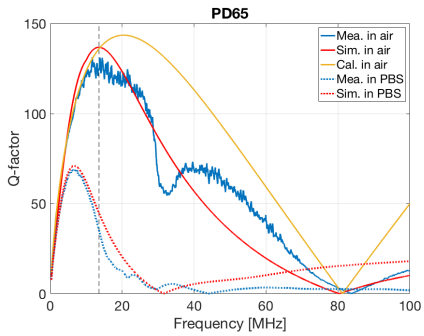

(e)

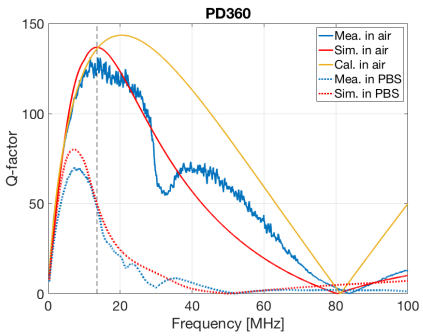

(f)

Figure B.1: Q-factors over frequency in air and PBS for the coils under test a) PC5, b) PC15, c) PD35, d) PD50, e) PD65, f) PD360.

Sample ID	**UCA**			**PC5**					**PC15**				
Environment	**Air without encapsulation**			**Air with encapsulation**			**PBS**		**Air with encapsulation**			**PBS**	
Method	Mea.	Sim.	Cal.	Mea.	Sim.	Cal.	Mea.	Sim.	Mea.	Sim.	Cal.	Mea.	Sim.
L (μm)	1.44	1.39	1.31	1.44	1.38	1.31	1.45	1.39	1.45	1.39	1.31	1.44	1.39
ReZ (Ω)	1	0.89	0.83	1.08	1.22	1.05	262	143.77	1	0.94	1.03	45.10	17.02
Rp (MΩ)	-	-	-	-	-	0.89	-	-	-	-	1.01	-	-
Rloss (kΩ)	15.68	16.79	16.35	14.23	12.37	13.04	-0.0012	-2.14	16.05	15.80	13.32	2.09	3.69
Cp (pF)	2.5	2.81	2.91	2.51	4.38	3.90	118.92	124.06	2.64	2.92	3.94	50.18	49.97
Ct2 (pf)	92.88	96.10	101.86	92.76	94.76	100.87	-	-	92.03	95.61	100.83	45.07	0.49
SRF (MHz)	83.73	80.35	81.28	83.54	64.47	70.20	12.2	12.12	81.18	78.66	69.85	18.68	19.09
Q	123.66	136.89	136.02	111.97	99.72	110.07	-0.78	-2.860	125.32	128.32	112.45	5.81	13.73
k	0.151	0.159	0.169	0.15	0.159	0.16	0.149	0.161	0.15	0.158	1.69	1.50	1.59
PTE	63.95	65.59	64.27	61.68	58.54	59.55	0	0	64.44	64.25	60.06	13.42	26.45

Table B.1: Measurement, simulation and calculation results for the ucnoated sample UCA and the Parylene-C PC5 and PC15. Note that for the sample PC5 where its SRF is lower than the operating frequency of 13.56 MHz, it behaves as a capacitor and thus its Rloss and Q-factor are negative.

Sample ID	**UCA**			**PD35**					**PD50**					**PD65**					**PD360**				
Environment	**Air without encapsulation**			**Air with encapsulation**			**PBS**		**Air with encapsulation**			**PBS**		**Air with encapsulation**			**PBS**		**Air with encapsulation**			**PBS**	
Method	Mea.	Sim.	Cal.	Mea.	Sim.	Cal.	Mea.	Sim.	Mea.	Sim.	Cal.	Mea.	Sim.	Mea.	Sim.	Cal.	Mea.	Sim.	Mea.	Sim.	Cal.	Mea.	Sim.
L (μm)	1.44	1.39	1.31	1.44	1.39	1.31	1.45	1.36	1.46	1.399	1.31	1.45	1.37	1.46	1.39	1.31	1.44	1.37	1.46	1.4	1.31	1.45	1.37
ReZ (Ω)	1	0.89	0.83	1.06	0.97	0.87	5.99	4.63	1.06	0.94	0.87	5.28	3.59	1.03	0.95	0.87	3.90	3.16	1.02	0.90	0.87	2.81	2.52
Rp (MΩ)	-	-	-	-	-	1.25	-	-	-	-	1.49	-	-	-	-	1.61	-	-	-	-	5.13	-	-
Rloss (kΩ)	15.68	16.79	16.35	16.04	15.49	15.71	4.09	5.93	15.57	15.98	15.74	4.35	6.38	16.02	15.69	15.75	5.16	6.62	16.28	16.70	15.86	6.60	6.54
Cp (pF)	2.5	2.81	2.91	2.99	3.25	3.92	14.05	29.56	3.09	3.14	3.98	12.38	22.36	3.24	3.15	4.01	8.95	18.52	3.65	3.24	4.58	6.38	7.37
Ct2 (pf)	92.88	96.10	101.86	91.67	95.23	100.86	80.60	71.48	91.08	95.34	100.79	82.34	78.17	91.05	95.62	100.74	86.34	81.84	90.52	95.01	100.20	88.22	92.75
SRF (MHz)	83.73	80.35	81.28	76.07	74.56	70.07	35.19	25.07	74.76	75.87	69.52	37.50	28.75	73.08	75.94	69.25	44.2	31.56	68.84	74.60	64.85	52.2	49.99
Q	123.66	136.89	136.02	118.23	125.31	133.02	25.14	34.76	120.15	129.39	133.20	27.68	41.11	123.54	127.36	133.26	35.37	44.76	124.86	134.70	133.39	47.45	49.88
k	0.151	0.159	0.169	0.15	0.158	0.169	1.499	0.163	0.149	0.158	0.169	0.150	1.62	0.149	0.159	0.169	1.509	1.61	0.149	0.158	0.169	1.49	1.61
PTE	63.95	65.59	64.27	63.20	63.79	63.98	29.14	39.26	63.70	64.50	64.03	30.77	41.24	64.34	64.08	64.04	35.25	42.24	64.70	65.47	64.19	41.75	41.93

Table B.2: Measurement, simulation and calculation results for the ucnoated sample UCA and the PDMS PD35, PD50, PD65 and PD360.

REFERENCES

[1] Kush Agarwal, Rangarajan Jegadeesan, Yong-Xin Guo, and Nitish V Thakor. Wireless power transfer strategies for implantable bioelectronics. *IEEE Reviews in Biomedical Engineering*, 10:136–161, 2017.

[2] Johnson I Agbinya. *Wireless power transfer*, volume 45, pages 523–526. River Publishers, 2015.

[3] M Ahmadian, BW Flynn, AF Murray, and DRS Cumming. Miniature transmitter for implantable micro systems. In *Engineering in Medicine and Biology Society, 2003. Proceedings of the 25th Annual International Conference of the IEEE*, volume 4, pages 3028–3031. IEEE, 2003.

[4] Dukju Ahn and Maysam Ghovanloo. Optimal design of wireless power transmission links for millimeter-sized biomedical implants. *IEEE Trans. Biomed. Circuits and Systems*, 10(1):125–137, 2016.

[5] Firas Akasheh, Todd Myers, John D Fraser, Susmita Bose, and Amit Bandyopadhyay. Development of piezoelectric micromachined ultrasonic transducers. *Sensors and Actuators A: Physical*, 111(2-3):275–287, 2004.

[6] Sina Akhbari, Firas Sammoura, Chen Yang, Amir Heidari, David Horsley, and Liwei Lin. Self-curved diaphragms by stress engineering for highly responsive pmut. In *2015 28th IEEE International Conference on Micro Electro Mechanical Systems (MEMS)*, pages 837–840. IEEE, 2015.

[7] James M Anderson, Analiz Rodriguez, and David T Chang. Foreign body reaction to biomaterials. In *Seminars in immunology*, volume 20, pages 86–100. Elsevier, 2008.

[8] L Ansoft. An introduction to hfss fundamental principles, concepts, and use. *Ansoft, Pittsburgh*, page 88, 2009.

[9] Oscar Aquilina. A brief history of cardiac pacing. *Images in paediatric cardiology*, 8(2):17, 2006.

[10] Amin Arbabian, Ting Chia Chang, Max L Wang, Jayant Charthad, Spyridon Baltsavias, Mojtaba Fallahpour, and Marcus J Weber. Sound technologies, sound bodies: Medical implants with ultrasonic links. *IEEE Microwave Magazine*, 17(12): 39–54, 2016.

[11] Robin Augustine. *Electromagnetic modelling of human tissues and its application on the interaction between antenna and human body in the BAN context*. PhD thesis, Paris Est, 2009.

[12] Umar Azad and Yuanxun Ethan Wang. Impact of receiver coil misalignment on near-field communication system performance. In *Proceedings of the 2012 IEEE International Symposium on Antennas and Propagation*, pages 1–2. IEEE, 2012.

[13] Peng Bai, Guang Zhu, Zong-Hong Lin, Qingshen Jing, Jun Chen, Gong Zhang, Jusheng Ma, and Zhong Lin Wang. Integrated multilayered triboelectric nanogenerator for harvesting biomechanical energy from human motions. *ACS nano*, 7(4): 3713–3719, 2013.

[14] Michael W Baker and Rahul Sarpeshkar. Feedback analysis and design of rf power links for low-power bionic systems. *IEEE Transactions on Biomedical Circuits and Systems*, 1(1):28–38, 2007.

[15] Surajit Das Barman, Ahmed Wasif Reza, Narendra Kumar, Md Ershadul Karim, and Abu Bakar Munir. Wireless powering by magnetic resonant coupling: Recent trends in wireless power transfer system and its applications. *Renewable and Sustainable Energy Reviews*, 51:1525–1552, 2015.

[16] JS Binette, M Garon, P Savard, MD McKee, and MD Buschmann. Tetrapolar measurement of electrical conductivity and thickness of articular cartilage. *Journal of biomechanical engineering*, 126(4):475–484, 2004.

[17] Karen Birmingham, Viviana Gradinaru, Polina Anikeeva, Warren M Grill, Victor Pikov, Bryan McLaughlin, Pankaj Pasricha, Douglas Weber, Kip Ludwig, and Kristoffer Famm. Bioelectronic medicines: a research roadmap. *Nature Reviews Drug Discovery*, 13(6):399, 2014.

[18] Kara Bocan and Ervin Sejdić. Adaptive transcutaneous power transfer to implantable devices: A state of the art review. *Sensors*, 16(3):393, 2016.

[19] B Bonaz, V Sinniger, D Hoffmann, D Clarencon, N Mathieu, C Dantzer, L Vercueil, C Picq, C Trocmé, P Faure, et al. Chronic vagus nerve stimulation in crohn's disease: a 6-month follow-up pilot study. *Neurogastroenterology & Motility*, 28(6): 948–953, 2016.

[20] Graham Brodie, Mohan V Jacob, and Peter Farrell. *Microwave and Radio-Frequency Technologies in Agriculture: an introduction for agriculturalists and engineers*, pages 55–57. Walter de Gruyter GmbH & Co KG, 2016.

[21] Chintan Buch, P Markondeya Raj, Billyde Brown, Himani Sharma, Teng Sun, Kyoung-Sik Moon, Klaus-Jürgen Wolter, Rao Tummala, Tadashi Takahashi, Keiji Takemura, et al. Ultra-thin wireless power module with integration of wireless inductive link and supercapacitors. In *2016 IEEE 66th Electronic Components and Technology Conference (ECTC)*, pages 2364–2371. IEEE, 2016.

[22] Walter Guyton Cady. Piezoelectricity: an introduction to the theory and applications of electromechanical phenomena in crystals. 1946.

[23] Marco Carminati, MD Vahey, Angelo Rottigni, Giorgio Ferrari, J Voldman, Marco Sampietro, et al. Enhancement of a labelfree dielectrophoretic cell sorter with an integrated impedance detection system. In *XIV International Conference on Miniaturized Systems for Chemistry and Life Sciences*, 2010.

[24] Michael Catrysse, Bart Hermans, and Robert Puers. An inductive power system with integrated bi-directional data-transmission. *Sensors and Actuators A: Physical*, 115(2-3):221–229, 2004.

[25] Marin Cernea, Ecaterina Andronescu, Roxana Radu, Fabio Fochi, and Carmen Galassi. Sol–gel synthesis and characterization of batio3-doped (bi0. 5na0. 5) tio3 piezoelectric ceramics. *Journal of Alloys and Compounds*, 490(1-2):690–694, 2010.

[26] Ting Chia Chang, Marcus J Weber, Max L Wang, Jayant Charthad, Butrus Pierre T Khuri-Yakub, and Amin Arbabian. Design of tunable ultrasonic receivers for efficient powering of implantable medical devices with reconfigurable power loads. *IEEE transactions on ultrasonics, ferroelectrics, and frequency control*, 63(10):1554–1562, 2016.

[27] Ting Chia Chang, Marcus J Weber, Jayant Charthad, Spyridon Baltsavias, and Amin Arbabian. End-to-end design of efficient ultrasonic power links for scaling towards submillimeter implantable receivers. *IEEE transactions on biomedical circuits and systems*, 12(5):1100–1111, 2018.

[28] Woo-Jin Chang, Demir Akin, Miroslav Sedlak, Michael R Ladisch, and Rashid Bashir. Poly (dimethylsiloxane)(pdms) and silicon hybrid biochip for bacterial culture. *Biomedical Microdevices*, 5(4):281–290, 2003.

[29] Jayant Charthad, Marcus J Weber, Ting Chia Chang, and Amin Arbabian. A mm-sized implantable medical device (imd) with ultrasonic power transfer and a hybrid bi-directional data link. *IEEE Journal of solid-state circuits*, 50(8):1741–1753, 2015.

[30] Jayant Charthad, Nemat Dolatsha, Angad Rekhi, and Amin Arbabian. System-level analysis of far-field radio frequency power delivery for mm-sized sensor nodes. *IEEE Transactions on Circuits and Systems I: Regular Papers*, 63(2):300–311, 2016.

[31] Yuhua Cheng, Gaofeng Wang, and Maysam Ghovanloo. Analytical modeling and optimization of small solenoid coils for millimeter-sized biomedical implants. *IEEE Transactions on Microwave Theory and Techniques*, 65(3):1024–1035, 2017.

[32] David B Christensen and Shad Roundy. Ultrasonically powered piezoelectric generators for bio-implantable sensors: Plate versus diaphragm. *Journal of Intelligent Material Systems and Structures*, 27(8):1092–1105, 2016.

[33] Douglas A Christensen. *Ultrasonic bioinstrumentation*. wiley New York, 1988.

[34] George VB Cochran, MW Johnson, MP Kadaba, F Vosburgh, MW Ferguson-Pell, and VR Palmeiri. Piezoelectric internal fixation devices: A new approach to electrical augmentation of osteogenesis. *Journal of orthopaedic research*, 3(4):508–513, 1985.

[35] Victoria Cotero, Ying Fan, Tea Tsaava, Adam M Kressel, Ileana Hancu, Paul Fitzgerald, Kirk Wallace, Sireesha Kaanumalle, John Graf, Wayne Rigby, et al. Noninvasive

sub-organ ultrasound stimulation for targeted neuromodulation. *Nature communications*, 10(1):952, 2019.

[36] JP Critchley, GJ Knight, and Walter William Wright. *Heat-resistant polymers: technologically useful materials*. Springer Science & Business Media, 2013.

[37] Brian Curran, Ivan Ndip, Jorg Bauer, Stephan Guttowski, Klaus Dieter Lang, and Herbert Reichl. The impact of moisture absorption on the electrical characteristics of organic dielectric materials. In *2011 12th Intl. Conf. on Thermal, Mechanical & Multi-Physics Simulation and Experiments in Microelectronics and Microsystems*, pages 1–5. IEEE, 2011.

[38] Brian Curran, Ivan Ndip, Ege Engin, Jorg Bauer, Harald Pötter, Klaus-Dieter Lang, and Herbert Reichl. A modeling approach for predicting the effects of dielectric moisture absorption on the electrical performance of passive structures. *Journal of Microelectronics and Electronic Packaging*, 11(3):115–121, 2014.

[39] Lyndon Da Cruz, Brian F Coley, Jessy Dorn, Francesco Merlini, Eugene Filley, Punita Christopher, Fred K Chen, Varalakshmi Wuyyuru, Jose Sahel, Paulo Stanga, et al. The argus ii epiretinal prosthesis system allows letter and word reading and long-term function in patients with profound vision loss. *British Journal of Ophthalmology*, 97(5):632–636, 2013.

[40] Canan Dagdeviren, Byung Duk Yang, Yewang Su, Phat L Tran, Pauline Joe, Eric Anderson, Jing Xia, Vijay Doraiswamy, Behrooz Dehdashti, Xue Feng, et al. Conformal piezoelectric energy harvesting and storage from motions of the heart, lung, and diaphragm. *Proceedings of the National Academy of Sciences*, 111(5):1927–1932, 2014.

[41] Carmelo De Maria, Licia Di Pietro, Andrés Díaz Lantada, June Madete, Philippa Ngaju Makobore, Mannan Mridha, Alice Ravizza, Janno Torop, and Arti Ahluwalia. Safe innovation: On medical device legislation in europe and africa. *Health Policy and Technology*, 7(2):156–165, 2018.

[42] Alexey Denisov and Eric Yeatman. Ultrasonic vs. inductive power delivery for miniature biomedical implants. In *Body Sensor Networks (BSN), 2010 International Conference on*, pages 84–89. IEEE, 2010.

[43] Charles S Desilets, John D Fraser, and Gordon S Kino. The design of efficient broad-band piezoelectric transducers. *IEEE Transactions on sonics and ultrasonics*, 25(3):115–125, 1978.

[44] Peter Dirksen. Pre-collapsed cmut with mechanical collapse retention, January 12 2012. US Patent App. 13/203,751.

[45] N de N Donaldson and TA Perkins. Analysis of resonant coupled coils in the design of radio frequency transcutaneous links. *Medical and Biological Engineering and computing*, 21(5):612–627, 1983.

[46] Zhu Duan, Yong-Xin Guo, and Dim-Lee Kwong. Rectangular coils optimization for wireless power transmission. *Radio Science*, 47(03):1–10, 2012.

[47] Herbert B Dwight. Skin effect in tubular and flat conductors. *Transactions of the American Institute of Electrical Engineers*, 37(2):1379–1403, 1918.

[48] TA Emadi, G Thomas, S Pistorius, and DA Buchanan. Capacitive micromachined ultrasonic transducer array with pencil beam shape and wide range beam steering. *Procedia Engineering*, 47:542–545, 2012.

[49] Elpida Episkopou, Stergios Papantonis, William J Otter, and Stepan Lucyszyn. Defining material parameters in commercial em solvers for arbitrary metal-based thz structures. *IEEE Transactions on terahertz science and Technology*, 2(5):513–524, 2012.

[50] SN Etkind, AE Bone, B Gomes, N Lovell, CJ Evans, IJ Higginson, and FEM Murtagh. How many people will need palliative care in 2040? past trends, future projections and implications for services. *BMC medicine*, 15(1):102, 2017.

[51] Erez Falkenstein, Michael Roberg, and Zoya Popovic. Low-power wireless power delivery. *IEEE Transactions on microwave theory and techniques*, 60(7):2277–2286, 2012.

[52] Feng-Ru Fan, Zhong-Qun Tian, and Zhong Lin Wang. Flexible triboelectric generator. *Nano energy*, 1(2):328–334, 2012.

[53] Michael Faraday. The bakerian lecture: Experimental researches in electricity. second series. *Philosophical Transactions of the Royal Society of London*, 122:163–194, 1832.

[54] Gordana Klaric Felic, David Ng, and E Skafidas. Investigation of frequency-dependent effects in inductive coils for implantable electronics. *IEEE Transactions on Magnetics*, 49(4):1353–1360, 2013.

[55] Rodolfo Castanho Fernandes and Azauri Albano de Oliveira. Iterative design method of weakly coupled magnetic elements for inductive power transfer. In *2013 Brazilian Power Electronics Conference*, pages 1088–1094. IEEE, 2013.

[56] Rosaria Ferrigno, Abraham D Stroock, Thomas D Clark, Michael Mayer, and George M Whitesides. Membraneless vanadium redox fuel cell using laminar flow. *Journal of the American Chemical Society*, 124(44):12930–12931, 2002.

[57] Kyriaki Fotopoulou and Brian W Flynn. Wireless power transfer in loosely coupled links: Coil misalignment model. *IEEE Transactions on Magnetics*, 47(2):416–430, 2011.

[58] Camelia Gabriel. Dielectric properties of biological materials. In *Bioengineering and Biophysical Aspects of Electromagnetic Fields*, pages 86–135. CRC press, 2006.

[59] Sami Gabriel, RW Lau, and Camelia Gabriel. The dielectric properties of biological tissues: Ii. measurements in the frequency range 10 hz to 20 ghz. *Physics in medicine & biology*, 41(11):2251, 1996.

[60] JC Maxwell Garnett. Xii. colours in metal glasses and in metallic films. *Philosophical Transactions of the Royal Society of London. Series A, Containing Papers of a Mathematical or Physical Character*, 203(359-371):385–420, 1904.

[61] Jaime Garnica, Raul A Chinga, and Jenshan Lin. Wireless power transmission: From far field to near field. *Proceedings of the IEEE*, 101(6):1321–1331, 2013.

[62] S Gevorgian, H Berg, H Jacobsson, and T Lewin. Application notes-basic parameters of coplanar-strip waveguides on multilayer dielectric/semiconductor substrates, part 1: high permittivity superstrates. *IEEE microwave magazine*, 4(2): 60–70, 2003.

[63] Spartak S Gevorgian. Basic characteristics of two layered substrate coplanar waveguides. *Electronics Letters*, 30(15):1236–1237, 1994.

[64] Giovanni Ghione and Michele Goano. Revisiting the partial-capacitance approach to the analysis of coplanar transmission lines on multilayered substrates. *IEEE Transactions on microwave theory and techniques*, 51(9):2007–2014, 2003.

[65] M Giacomelli Penon, SJ Picken, Michael Wübbenhorst, G De Vos, and J Van Turnhout. Dielectric water sorption analysis. *Review of scientific instruments*, 77(11): 115107, 2006.

[66] Vasiliki Giagka and Wouter A Serdijn. Realizing flexible bioelectronic medicines for accessing the peripheral nerves–technology considerations. *Bioelectronic Medicine*, 4(1):8, 2018.

[67] J-C Ginefri, A Rubin, M Tatoulian, M Woytasik, F Boumezbeur, B Djemaï, M Poirier-Quinot, F Lethimonnier, L Darrasse, and E Dufour-Gergam. Implanted, inductively-coupled, radiofrequency coils fabricated on flexible polymeric material: Application to in vivo rat brain mri at 7 t. *Journal of Magnetic Resonance*, 224: 61–70, 2012.

[68] JP Goedbloed. Conformal mapping methods in two-dimensional magnetohydrodynamics. *Computer Physics Communications*, 24(3-4):311–321, 1981.

[69] William F Gorham. A new, general synthetic method for the preparation of linear poly-p-xylylenes. *Journal of Polymer Science Part A-1: Polymer Chemistry*, 4(12): 3027–3039, 1966.

[70] Mahammad A Hannan, Saad Mutashar, Salina A Samad, and Aini Hussain. Energy harvesting for the implantable biomedical devices: issues and challenges. *Biomedical engineering online*, 13(1):79, 2014.

[71] Reid R Harrison. Designing efficient inductive power links for implantable devices. In *Circuits and Systems, 2007. ISCAS 2007. IEEE International Symposium on*, pages 2080–2083. IEEE, 2007.

[72] Christina Hassler, Tim Boretius, and Thomas Stieglitz. Polymers for neural implants. *Journal of Polymer Science Part B: Polymer Physics*, 49(1):18–33, 2011.

[73] David Hayward, Elisabeth Hollins, Peter Johncock, Iain McEwan, Richard A Pethrick, and Elisabeth A Pollock. The cure and diffusion of water in halogen containing epoxy/amine thermosets. *Polymer*, 38(5):1151–1168, 1997.

[74] William J Heetderks. Rf powering of millimeter-and submillimeter-sized neural prosthetic implants. *IEEE Transactions on Biomedical Engineering*, 35(5):323–327, 1988.

[75] ROBERT G HILL. Biomedical polymers. In *Biomaterials, Artificial Organs and Tissue Engineering*, pages 97–106. Elsevier, 2005.

[76] Scott Hinaga, Marina Koledintseva, P Anmula, and J Drewniak. Effect of conductor surface roughness upon measured loss and extracted values of pcb laminate material dissipation factor. In *Proc. Techn. Conf. IPC Expo/APEX 2009*, pages S20–2, 2009.

[77] Takuichi Hirano, Jiro Hirokawa, and Makoto Ando. Influence of the sma connector and its modeling on electromagnetic simulation. *Microwave and Optical Technology Letters*, 57(9):2168–2171, 2015.

[78] John S Ho, Alexander J Yeh, Evgenios Neofytou, Sanghoek Kim, Yuji Tanabe, Bhagat Patlolla, Ramin E Beygui, and Ada SY Poon. Wireless power transfer to deep-tissue microimplants. *Proceedings of the National Academy of Sciences*, 111(22):7974–7979, 2014.

[79] Ingeborg Hochmair, Peter Nopp, Claude Jolly, Marcus Schmidt, Hansjörg Schößer, Carolyn Garnham, and Ilona Anderson. Med-el cochlear implants: state of the art and a glimpse into the future. *Trends in amplification*, 10(4):201–219, 2006.

[80] Johannes Hoffmann, Christian Hafner, Patrick Leidenberger, Jan Hesselbarth, and Sven Burger. Comparison of electromagnetic field solvers for the 3d analysis of plasmonic nanoantennas. In *Modeling Aspects in Optical Metrology II*, volume 7390, page 73900J. International Society for Optics and Photonics, 2009.

[81] R Holland. Representation of dielectric, elastic, and piezoelectric losses by complex coefficients. *IEEE transactions on Sonics and Ultrasonics*, 14(1):18–20, 1967.

[82] Ahmed Ibrahim and Mehdi Kiani. A figure-of-merit for design and optimization of inductive power transmission links for millimeter-sized biomedical implants. *IEEE transactions on biomedical circuits and systems*, 10(6):1100–1111, 2016.

[83] Agilent Technologies Inc. Impedance measurement handbook. July 2006.

[84] Ashraf B Islam, Syed K Islam, and Fahmida S Tulip. Design and optimization of printed circuit board inductors for wireless power transfer system. 2013.

[85] H Jaffe and DA Berlincourt. Piezoelectric transducer materials. *Proceedings of the IEEE*, 53(10):1372–1386, 1965.

[86] Mohammad-Ali Jazayeri, Martin P Emert, JoAnn Bartos, Ted Tabbert, Dhanunjaya R Lakkireddy, and Mohammad-Reza Jazayeri. Subcutaneous implantable cardioverter-defibrillator placement in a patient with a preexisting transvenous implantable cardioverter-defibrillator. *HeartRhythm case reports*, 3(6):306–310, 2017.

[87] Rangarajan Jegadeesan and Yong-Xin Guo. Topology selection and efficiency improvement of inductive power links. *IEEE Transactions on Antennas and Propagation*, 60(10):4846–4854, 2012.

[88] Rangarajan Jegadeesan, Kush Agarwal, Yong-Xin Guo, Shih-Cheng Yen, and Nitish V Thakor. Wireless power delivery to flexible subcutaneous implants using capacitive coupling. *IEEE Transactions on Microwave Theory and Techniques*, 65 (1):280–292, 2017.

[89] Jørgen Arendt Jensen. Field: A program for simulating ultrasound systems. In *10TH NORDICBALTIC CONFERENCE ON BIOMEDICAL IMAGING, VOL. 4, SUPPLEMENT 1, PART 1: 351–353*. Citeseer, 1996.

[90] Guangqiang Jiang and David D Zhou. Technology advances and challenges in hermetic packaging for implantable medical devices. In *Implantable Neural Prostheses 2*, pages 27–61. Springer, 2009.

[91] Uei-Ming Jow and Maysam Ghovanloo. Design and optimization of printed spiral coils for efficient transcutaneous inductive power transmission. *IEEE Transactions on biomedical circuits and systems*, 1(3):193–202, 2007.

[92] Uei-Ming Jow and Maysam Ghovanloo. Modeling and optimization of printed spiral coils in air and muscle tissue environments. In *Engineering in Medicine and Biology Society, 2009. EMBC 2009. Annual International Conference of the IEEE*, pages 6387–6390. IEEE, 2009.

[93] HC Karner and A Schutz. The dielectric properties of fibre reinforced epoxies under the influence of humidity. In *Properties and Applications of Dielectric Materials, 1994., Proceedings of the 4th International Conference on*, volume 1, pages 344–347. IEEE, 1994.

[94] S Kerzenmacher, J Ducrée, R Zengerle, and F Von Stetten. Energy harvesting by implantable abiotically catalyzed glucose fuel cells. *Journal of Power Sources*, 182 (1):1–17, 2008.

[95] Adam Khalifa, Yasha Karimi, Milutin Stanaćević, and Ralph Etienne-Cummings. Novel integration and packaging concepts of highly miniaturized inductively powered neural implants. In *Engineering in Medicine and Biology Society (EMBC), 2017 39th Annual International Conference of the IEEE*, pages 234–237. IEEE, 2017.

[96] Alireza Khaligh, Peng Zeng, and Cong Zheng. Kinetic energy harvesting using piezoelectric and electromagnetic technologies—state of the art. *IEEE Transactions on Industrial Electronics*, 57(3):850–860, 2010.

[97] Sadeque Reza Khan and GoangSeog Choi. Analysis and optimization of four-coil planar magnetically coupled printed spiral resonators. *Sensors*, 16(8):1219, 2016.

[98] Butrus T Khuri-Yakub and Ömer Oralkan. Capacitive micromachined ultrasonic transducers for medical imaging and therapy. *Journal of micromechanics and microengineering*, 21(5):054004, 2011.

[99] Mehdi Kiani and Maysam Ghovanloo. An rfid-based closed-loop wireless power transmission system for biomedical applications. *IEEE Transactions on Circuits and Systems II: Express Briefs*, 57(4):260–264, 2010.

[100] Sanghoek Kim, John S Ho, Lisa Y Chen, and Ada SY Poon. Wireless power transfer to a cardiac implant. *Applied Physics Letters*, 101(7):073701, 2012.

[101] Sohee Kim, Reid R Harrison, and Florian Solzbacher. Influence of system integration and packaging on its inductive power link for an integrated wireless neural interface. *IEEE Transactions on Biomedical Engineering*, 56(12):2927–2936, 2009.

[102] Gordon S Kino. *Acoustic waves: devices, imaging, and analog signal processingPrentice-Hall Signal Processing Series*. Englewood Cliffs, Prentice-Hall, 1987.

[103] Asimina Kiourti and Konstantina S Nikita. Miniature scalp-implantable antennas for telemetry in the mics and ism bands: design, safety considerations and link budget analysis. *IEEE Transactions on Antennas and Propagation*, 60(8):3568–3575, 2012.

[104] MCAM Koolen, JAM Geelen, and MPJG Versleijen. An improved de-embedding technique for on-wafer high-frequency characterization. In *Proceedings of the 1991 Bipolar Circuits and Technology Meeting*, pages 188–191. IEEE, 1991.

[105] George Kossoff. The effects of backing and matching on the performance of piezoelectric ceramic transducers. *IEEE Transactions on sonics and ultrasonics*, 13(1): 20–30, 1966.

[106] Y Kozlovsky. Vibration of plates in contact with viscous fluid: Extension of lamb's model. *Journal of Sound and Vibration*, 326(1-2):332–339, 2009.

[107] Richard Krimholtz, David A Leedom, and George L Matthaei. New equivalent circuits for elementary piezoelectric transducers. *Electronics Letters*, 6(13):398–399, 1970.

[108] Rajaram Krishnan. *AC electrokinetic separation and detection of nanoparticles and DNA nanoparticulates under high conductance conditions*. PhD thesis, UC San Diego, 2010.

[109] William B Kuhn and Noureddin M Ibrahim. Analysis of current crowding effects in multiturn spiral inductors. *IEEE Transactions on Microwave Theory and Techniques*, 49(1):31–38, 2001.

[110] Andre Kurs, Aristeidis Karalis, Robert Moffatt, John D Joannopoulos, Peter Fisher, and Marin Soljačić. Wireless power transfer via strongly coupled magnetic resonances. *science*, 317(5834):83–86, 2007.

[111] Horace Lamb. On the vibrations of an elastic plate in contact with water. *Proc. R. Soc. Lond. A*, 98(690):205–216, 1920.

[112] Sanghoon Lee, Wendy Yen Xian Peh, Jiahui Wang, Fengyuan Yang, John S Ho, Nitish V Thakor, Shih-Cheng Yen, and Chengkuo Lee. Toward bioelectronic medicine—neuromodulation of small peripheral nerves using flexible neural clip. *Advanced Science*, 4(11):1700149, 2017.

[113] Thomas H Lee. The design of cmos radio-frequency integrated circuits. *Communications Engineer*, 2(4):47–47, 2004.

[114] Bert Lenaerts and Robert Puers. *Omnidirectional inductive powering for biomedical implants*, pages 197–198. Springer, 2009.

[115] Chang Liu. Recent developments in polymer mems. *Advanced Materials*, 19(22): 3783–3790, 2007.

[116] Changrong Liu, Yong-Xin Guo, Hucheng Sun, and Shaoqiu Xiao. Design and safety considerations of an implantable rectenna for far-field wireless power transfer. *IEEE Transactions on antennas and Propagation*, 62(11):5798–5806, 2014.

[117] Xun Liu, WM Ng, CK Lee, and SY Hui. Optimal operation of contactless transformers with resonance in secondary circuits. In *Applied Power Electronics Conference and Exposition, 2008. APEC 2008. Twenty-Third Annual IEEE*, pages 645–650. IEEE, 2008.

[118] H Looyenga. Dielectric constants of heterogeneous mixtures. *Physica*, 31(3):401–406, 1965.

[119] Xin Lu, Gu Xu, Peter G Hofstra, and Robert C Bajcar. Moisture–absorption, dielectric relaxation, and thermal conductivity studies of polymer composites. *Journal of Polymer Science Part B: Polymer Physics*, 36(13):2259–2265, 1998.

[120] Yan Lu and Wing-Hung Ki. A 13.56 mhz cmos active rectifier with switched-offset and compensated biasing for biomedical wireless power transfer systems. *IEEE transactions on biomedical circuits and systems*, 8(3):334–344, 2013.

[121] William H Maisel, Michael O Sweeney, William G Stevenson, Kristin E Ellison, and Laurence M Epstein. Recalls and safety alerts involving pacemakers and implantable cardioverter-defibrillator generators. *Jama*, 286(7):793–799, 2001.

[122] JM Manley and HE Rowe. Some general properties of nonlinear elements-part i. general energy relations. *Proceedings of the IRE*, 44(7):904–913, 1956.

[123] HFSS Manual. Electromagnetics suite version 15.0. 0, 2014.

[124] Warren P Mason. Electromechanical transducers and wave filters. 1948.

[125] Alex V Mezheritsky. Efficiency of excitation of piezoceramic transducers at antiresonance frequency. *IEEE transactions on ultrasonics, ferroelectrics, and frequency control*, 49(4):484–494, 2002.

[126] Aaron D Mickle, Sang Min Won, Kyung Nim Noh, Jangyeol Yoon, Kathleen W Meacham, Yeguang Xue, Lisa A McIlvried, Bryan A Copits, Vijay K Samineni, Kaitlyn E Crawford, et al. A wireless closed-loop system for optogenetic peripheral neuromodulation. *Nature*, 565(7739):361, 2019.

[127] Mohamad Harris Misran, Abdul Rahim, Sharul Kamal, Akaa Agbaeze Eteng, and Guy AE Vandenbosch. Assessment of kapton-based flexible antenna for near field wireless energy transfer. *Applied Computational Electromagnetics Society Journal*, 32(1), 2017.

[128] Sunderarajan S Mohan, Maria del Mar Hershenson, Stephen P Boyd, and Thomas H Lee. Simple accurate expressions for planar spiral inductances. *IEEE Journal of solid-state circuits*, 34(10):1419–1424, 1999.

[129] Jorge Mario Herrera Morales. *Evaluating biocompatible barrier films as encapsulants of medical micro devices*. PhD thesis, Université Grenoble Alpes, 2015.

[130] Steven A Morris and Chriswell G Hutchens. Implementation of mason's model on circuit analysis programs. *IEEE transactions on ultrasonics, ferroelectrics, and frequency control*, 33(3):295–298, 1986.

[131] Saad Mutashar, Mahammad A Hannan, Salina A Samad, and Aini Hussain. Analysis and optimization of spiral circular inductive coupling link for bio-implanted applications on air and within human tissue. *Sensors*, 14(7):11522–11541, 2014.

[132] Xavier Navarro, Thilo B Krueger, Natalia Lago, Silvestro Micera, Thomas Stieglitz, and Paolo Dario. A critical review of interfaces with the peripheral nervous system for the control of neuroprostheses and hybrid bionic systems. *Journal of the Peripheral Nervous System*, 10(3):229–258, 2005.

[133] CR Neagu, HV Jansen, A Smith, JGE Gardeniers, and MC Elwenspoek. Characterization of a planar microcoil for implantable microsystems. *Sensors and Actuators A: Physical*, 62(1-3):599–611, 1997.

[134] Robert E Newnham, LJ Bowen, KA Klicker, and LE Cross. Composite piezoelectric transducers. *Materials & Design*, 2(2):93–106, 1980.

[135] M Olfatnia, Z Shen, JM Miao, LS Ong, T Xu, and M Ebrahimi. Medium damping influences on the resonant frequency and quality factor of piezoelectric circular microdiaphragm sensors. *Journal of micromechanics and microengineering*, 21 (4):045002, 2011.

[136] Jacopo Olivo, Sandro Carrara, and Giovanni De Micheli. Modeling of printed spiral inductors for remote powering of implantable biosensors. In *2011 5th International Symposium on Medical Information and Communication Technology*, pages 29–32. IEEE, 2011.

[137] Sophocles J Orfanidis. Electromagnetic waves and antennas. 2002.

[138] Shaul Ozeri and Doron Shmilovitz. Ultrasonic transcutaneous energy transfer for powering implanted devices. *Ultrasonics*, 50(6):556–566, 2010.

[139] Donatella Paolino, Piyush Sinha, Massimo Fresta, and Mauro Ferrari. Drug delivery systems. *Encyclopedia of medical devices and instrumentation*, 2006.

[140] Jongmin Park, Youndo Tak, Yoongoo Kim, Youngwook Kim, and Sangwook Nam. Investigation of adaptive matching methods for near-field wireless power transfer. *IEEE Transactions on Antennas and Propagation*, 59(5):1769–1773, 2011.

[141] M Giacomelli Penon, SJ Picken, M Wubbenhorst, G De Vos, and J van Tumhout. Dielectric water sorption analysis. *Review of Scientific Instruments*, 77(11):115107, 2006.

[142] Ronald Pethig. Dielectric and electrical properties of biological materials. *Journal of Bioelectricity*, 4(2):vii–ix, 1985.

[143] Ewald Pettenpaul, Hartmut Kapusta, Andreas Weisgerber, Heinrich Mampe, Jürgen Luginsland, and Ingo Wolff. Cad models of lumped elements on gaas up to 18 ghz. *IEEE Transactions on Microwave Theory and Techniques*, 36(2):294–304, 1988.

[144] AB Pippard. Experimental analysis of the electronic structure of metals. *Reports on Progress in Physics*, 23(1):176, 1960.

[145] polymerdatabase.com. Cucco: The coupled coil configurator. URL https://polymerdatabase.com/polymers/Polydimethylsiloxane.html.

[146] Charles A Popeney and Kenneth M Aló. Peripheral neurostimulation for the treatment of chronic, disabling transformed migraine. *Headache: The Journal of Head and Face Pain*, 43(4):369–375, 2003.

[147] Zoya Popovic and Branko Popovic. *Introductory electromagnetics*, pages 383–388. Prentice˜ Hall, 2000.

[148] Suryanarayana AN Prasad, Quentin Gallas, Stephen B Horowitz, Brian D Homeijer, Bhavani V Sankar, Louis N Cattafesta, and Mark Sheplak. Analytical electroacoustic model of a piezoelectric composite circular plate. *AIAA journal*, 44(10): 2311–2318, 2006.

[149] Yiheng Qin, Matiar MR Howlader, M Jamal Deen, Yaser M Haddara, and P Ravi Selvaganapathy. Polymer integration for packaging of implantable sensors. *Sensors and Actuators B: Chemical*, 202:758–778, 2014.

[150] Yogesh K Ramadass and Anantha P Chandrakasan. A battery-less thermoelectric energy harvesting interface circuit with 35 mv startup voltage. *IEEE Journal of Solid-State Circuits*, 46(1):333–341, 2011.

[151] A Ramos, E Riera, JL San Emeterio, and PT Sanz. Modelling of multilayer piezoelectric transducers for echographic applications equivalent circuits. *Mundo Electronico*, 187, 1988.

[152] Anil Kumar RamRakhyani, Shahriar Mirabbasi, and Mu Chiao. Design and optimization of resonance-based efficient wireless power delivery systems for biomedical implants. *IEEE Transactions on Biomedical Circuits and Systems*, 5(1): 48–63, 2011.

[153] James C Rautio and Veysel Demir. Microstrip conductor loss models for electromagnetic analysis. *IEEE transactions on microwave theory and techniques*, 51(3): 915–921, 2003.

[154] M Redwood. Transient performance of a piezoelectric transducer. *The journal of the acoustical society of America*, 33(4):527–536, 1961.

[155] DG Rickerby. Societal and policy aspects of the introduction of nanotechnology in healthcare. *International journal of healthcare technology and management*, 7(6): 463–473, 2006.

[156] DA Robinson and SP Friedman. Effect of particle size distribution on the effective dielectric permittivity of saturated granular media. *Water Resources Research*, 37 (1):33–40, 2001.

[157] Joana F Sacramento, Daniel J Chew, Bernardete F Melo, Matteo Donegá, Wesley Dopson, Maria P Guarino, Alison Robinson, Jesus Prieto-Lloret, Sonal Patel, Bradley J Holinski, et al. Bioelectronic modulation of carotid sinus nerve activity in the rat: a potential therapeutic approach for type 2 diabetes. *Diabetologia*, 61 (3):700–710, 2018.

[158] Alanson P Sample, David T Meyer, and Joshua R Smith. Analysis, experimental results, and range adaptation of magnetically coupled resonators for wireless power transfer. *IEEE Transactions on industrial electronics*, 58(2):544–554, 2011.

[159] Edward Sazonov and Michael R Neuman. *Wearable Sensors: Fundamentals, implementation and applications*. Elsevier, 2014.

[160] William G Scanlon, B Burns, and Noel E Evans. Radiowave propagation from a tissue-implanted source at 418 mhz and 916.5 mhz. *IEEE Transactions on Biomedical Engineering*, 47(4):527–534, 2000.

[161] Kee Scholten and Ellis Meng. Materials for microfabricated implantable devices: a review. *Lab on a Chip*, 15(22):4256–4272, 2015.

[162] Schormans. Cucco: The coupled coil configurator. URL https://github.com/schormans/CuCCo.

[163] Matthew Schormans, Virgilio Valente, and Andreas Demosthenous. Practical inductive link design for biomedical wireless power transfer: A tutorial. *IEEE transactions on biomedical circuits and systems*, (99), 2018.

[164] Dongjin Seo, Jose M Carmena, Jan M Rabaey, Elad Alon, and Michel M Maharbiz. Neural dust: An ultrasonic, low power solution for chronic brain-machine interfaces. *arXiv preprint arXiv:1307.2196*, 2013.

[165] Dongjin Seo, Jose M Carmena, Jan M Rabaey, Michel M Maharbiz, and Elad Alon. Model validation of untethered, ultrasonic neural dust motes for cortical recording. *Journal of neuroscience methods*, 244:114–122, 2015.

[166] John S Seybold. *Introduction to RF propagation*, page 22. John Wiley & Sons, 2005.

[167] Shima Shahab, Sihong Zhao, and Alper Erturk. Soft and hard piezoelectric ceramics and single crystals for random vibration energy harvesting. *Energy Technology*, 6(5):935–942, 2018.

[168] Stewart Sherrit and Binu K Mukherjee. Characterization of piezoelectric materials for transducers. *arXiv preprint arXiv:0711.2657*, 2007.

[169] Stewart Sherrit, Sean P Leary, Benjamin P Dolgin, and Yoseph Bar-Cohen. Comparison of the mason and klm equivalent circuits for piezoelectric resonators in the thickness mode. In *Ultrasonics Symposium, 1999. Proceedings. 1999 IEEE*, volume 2, pages 921–926. IEEE, 1999.

[170] Po-Jen Shih and Wen-Pin Shih. Design, fabrication, and application of bioimplantable acoustic power transmission. *Journal of Microelectromechanical Systems*, 19(3):494–502, 2010.

[171] Nosherwan Shoaib. *Vector Network Analyzer (VNA) Measurements and Uncertainty Assessment*, page 5. Springer, 2017.

[172] Ping Si, Aiguo Patrick Hu, David Budgett, Simon Malpas, Joseph Yang, and Jinfeng Gao. Stabilizing the operating frequency of a resonant converter for wireless power transfer to implantable biomedical sensors. In *Proc. 1st Int. Conf. Sensing Technology*, pages 477–482, 2005.

[173] Erhaer K Sittig. Effects of bonding and electrode layers on the transmission parameters of piezoelectric transducers used in ultrasonic digital delay lines. *IEEE Transactions on Sonics and Ultrasonics*, 16(1):2–9, 1969.

[174] Amir M Sodagar and Parviz Amiri. Capacitive coupling for power and data telemetry to implantable biomedical microsystems. In *Neural Engineering, 2009. NER'09. 4th International IEEE/EMBS Conference on*, pages 411–414. IEEE, 2009.

[175] Ferroelectrics Standards Committee of the IEEE Ultrasonics and Frequency Control Society. Ieee standard on piezoelectricity, 1987.

[176] Thomas Stieglitz. Manufacturing, assembling and packaging of miniaturized neural implants. *Microsystem technologies*, 16(5):723–734, 2010.

[177] John William Strutt and Baron Rayleigh. *The theory of sound*. Dover, 1945.

[178] Changyi Su, Haixin Ke, and Todd Hubing. Overview of electromagnetic modeling software. In *Proc. of the 25th International Review of Progress in Applied Computational Electromagnetics*, pages 736–741, 2009.

[179] Charles R Sullivan and Richard Y Zhang. Simplified design method for litz wire. In *2014 IEEE Applied Power Electronics Conference and Exposition-APEC 2014*, pages 2667–2674. IEEE, 2014.

[180] Shin-nosuke Suzuki, Shunsuke Kimura, Tamotsu Katane, Hideo Saotome, Osami Saito, and Kazuhito Kobayashi. Power and interactive information transmission to implanted medical device using ultrasonic. *Japanese journal of applied physics*, 41(5S):3600, 2002.

[181] Keysight Technologies. Impedance measurement handbook, 2016. URL https://literature.cdn.keysight.com/litweb/pdf/5950-3000.pdf.

[182] N Tesla. The transmission of electric energy without wires (the thirteenth anniversary number of the electrical world and engineer). 1904.

[183] Kenji Uchino, Yuan Zhuang, and SEYIT O URAL. Loss determination methodology for a piezoelectric ceramic: new phenomenological theory and experimental proposals. *Journal of Advanced Dielectrics*, 1(01):17–31, 2011.

[184] NM Van Hemel and EE Van der Wall. 8 october 1958, d day for the implantable pacemaker. 2008.

[185] Santhosh D Vishwakarma, AK Pandey, JM Parpia, and R Pratap. Contribution of acoustic losses in the quality factor of a micromechanical resonator. *arXiv preprint arXiv:1204.4701*, 2012.

[186] Bhadri Visweswaran, Prashant Mandlik, Siddharth Harikrishna Mohan, Jeff A Silvernail, Ruiqing Ma, James C Sturm, and Sigurd Wagner. Diffusion of water into permeation barrier layers. *Journal of Vacuum Science & Technology A: Vacuum, Surfaces, and Films*, 33(3):031513, 2015.

[187] Antonio Arnau Vives. *Piezoelectric transducers and applications*. Springer Science & Business Media, 2008.

[188] Ruchi Warty, Mohammad-Reza Tofighi, Usmah Kawoos, and Arye Rosen. Characterization of implantable antennas for intracranial pressure monitoring: Reflection by and transmission through a scalp phantom. *IEEE Transactions on Microwave Theory and Techniques*, 56(10):2366–2376, 2008.

[189] Ju Hyung We, Sun Jin Kim, and Byung Jin Cho. Hybrid composite of screen-printed inorganic thermoelectric film and organic conducting polymer for flexible thermoelectric power generator. *Energy*, 73:506–512, 2014.

[190] Thomas Weiland, Martin Timm, and Irina Munteanu. A practical guide to 3-d simulation. *IEEE Microwave Magazine*, 9(6):62–75, 2008.

[191] Harold A Wheeler. Simple inductance formulas for radio coils. *Proceedings of the Institute of Radio Engineers*, 16(10):1398–1400, 1928.

[192] Long Wu and Yeong-Chin Chen. Pspice approach for designing the ultrasonic piezoelectric transducer for medical diagnostic applications. *Sensors and Actuators A: Physical*, 75(2):186–198, 1999.

[193] Kuek Chee Yaw. Measurement of dielectric material properties: Application note. *Rhode and Shawrtz Technical Publication*, 2012.

[194] Chu-Sun Yen, Zvonko Fazarinc, and Richard L Wheeler. Time-domain skin-effect model for transient analysis of lossy transmission lines. *Proceedings of the IEEE*, 70(7):750–757, 1982.

[195] Meysam Zargham and P Glenn Gulak. Maximum achievable efficiency in near-field coupled power-transfer systems. *IEEE Transactions on Biomedical Circuits and Systems*, 6(3):228–245, 2012.

[196] David L Zealear, Kurt C Garren, Ricardo J Rodriguez, Julio H Reyes, Shan Huang, Mehmet R Dokmeci, and Khalil Najafi. The biocompatibility, integrity, and positional stability of an injectable microstimulator for reanimation of the paralyzed larynx. *IEEE transactions on biomedical engineering*, 48(8):890–897, 2001.

[197] Yangkun Zhang, Tien-Fu Lu, and Yuxin Peng. Three-port equivalent circuit of multi-layer piezoelectric stack. *Sensors and Actuators A: Physical*, 236:92–97, 2015.

[198] Clemens M Zierhofer and Erwin S Hochmair. High-efficiency coupling-insensitive transcutaneous power and data transmission via an inductive link. *IEEE Transactions on biomedical engineering*, 37(7):716–722, 1990.

[199] Zimmerman. Global bio-electronic market size, status and forecast 2018-2025. URL https://www.radiantinsights.com/research/global-bio-electronic-market-size-status-and-forecast-2018-2025.

[200] Diana M Zuckerman, Paul Brown, and Steven E Nissen. Medical device recalls and the fda approval process. *Archives of internal medicine*, 171(11):1006–1011, 2011.